NTNU

Norwegian University of
Science and Technology

Exploring V_2C MXene as a New Cathode Material for Rechargeable Magnesium Batteries

Frode Håskjold Fagerli

Nanotechnology
Submission date: July 2018
Supervisor: Fride Vullum, IMA
Co-supervisor: Henning Kaland, IMA

Norwegian University of Science and Technology
Department of Materials Science and Engineering

Preface

This thesis has been completed in partial fulfillment of the requirements for the degree of Master of Science in Nanotechnology at NTNU. It has been a project under the Department for Materials Science and Engineering, during the spring semester of 2018. The project has been strongly connected to that of PhD candidate and co-supervisor Henning Kaland, and some of the experimental work has therefore been performed in collaboration with him.

First of all, I would like to thank my supervisor Fride Vullum-Bruer, for her guidance and general support throughout the project. I would also like to express my sincere gratitude to Henning Kaland, who has been a great mentor and discussion partner during this period. He is explicitly thanked for his assistance in all of the etching processes, for allowing me to use some of his mixed electrolytes and cycling results, as well as for the introduction to many of the experimental techniques used as a part of this project. Moreover, I would like to thank Torild Krogstad for her patience and assistance during most of the etching processes, and Yingda Yu for his help with the SEM and EDX instruments. Lastly, I would like to thank the participants of the regular battery and ceramic group meetings, for their comments and thoughts to my presentations.

On a personal level, I would like to thank my friends and collegues at NTNU, who has made this journey worthwhile. A special thanks is also devoted to Isa-Lill Wangbergtrø and my family, who has been especially supportive in the final stages of this writing period.

Frode Håskjold Fagerli

Trondheim, 12.07.2018

Abstract

Rechargeable magnesium batteries (RMBs) is a promising technology to compete with state-of-the art lithium-ion batteries, due to the possible improvements in safety, abundance of materials and energy density. However, one major problem with RMBs is the lack of suitable cathode materials that can host Mg-ions without trapping them. A new two-dimensional material, known as MXenes, has received increasing interest as a potential electrode material, due to its inherent high electrical conductivity and ion intercalation capabilities. In this work, one of these MXenes, namely V_2C, has been synthesized and electrochemically characterized in order to evaluate it as a potential cathode material for RMBs.

First, the V_2AlC MAX phase was synthesized by sintering a powder mixture of elemental V, Al, C, before the Al layer of the MAX phase was selectively etched out using a concentrated HF solution, to give multilayered V_2C MXene. Some of the multilayered V_2C was also treated with a tetrabutylammonium hydroxide (TBAOH) solution and delaminated. The structure, morphology and elemental content of the synthesized materials were characterized by X-ray spectroscopy (XRD), scanning electron microscopy (SEM) and energy dispersive X-ray spectroscopy (EDX). All of the active materials were then used to form cathodes, by drop casting a slurry containing the active material onto carbon paper, which later were assembled into coin cells and tested by electrochemical cycling.

The most critical aspects for obtaining phase pure V_2C MXene with high yield, a suitable particle size distribution and morphology was found to be strongly dependent on the synthesis procedure of the V_2AlC MAX phase, as well as the subsequent etching time and HF concentration. Using an electrolyte consisting of 0.4 M all phenyl complex solved in tetrahydrofuran (APC:THF), the different active materials showed limited cathode capacities (<4 mAh/g), indicating no significant Mg-ion intercalation into the V_2C structure. The TBAOH treatment and delamination of V_2C resulted in an increase of interlayer distance by 2.2 Å and reduced particle sizes, respectively, but was not found to considerably improve the cycling performance. However, with the inclusion of 0.4 M LiCl into the electrolyte (APC/LiCl:THF), the obtained capacity increased significantly (70 mAh/g after 50 cycles), demonstrating the intercalation of less charge dense Li-ions. The limited capacity obtained with the V_2C MXene was attributed to high Mg-ion migration barriers, and future efforts should be directed toward lowering of these barriers, while keeping the operating potential as high as possible. With optimized termination groups, interlayer distances and morphology of the V_2C particles, together with an improved electrolyte, V_2C could still be a promising cathode material, enabling energy dense RMBs and hybrid Mg-Li batteries.

Sammendrag

Oppladbare magnesiumbatterier (OMBer) er en lovende utfordrer for den ledende litium-ionbatteri-teknologien, på grunn av dets forbedringspotensial innenfor sikkerhet, pris og energitetthet. En utfordring med OMBer er imidlertid mangelen på egnede katodematerialer som kan holde Mg-ioner uten å fange dem. Et nytt todimensjonalt materiale, kjent som MXener, har fått økende interesse som et potensielt elektrodemateriale, grunnet høy elektrisk ledningsevne og muligheter for ioneinterkalasjon. I dette arbeidet har en av disse MXenene, nemlig V_2C, blitt syntetisert og elektrokjemisk karakterisert for å evaluere den som et potensielt katodemateriale for OMBer.

Først ble V_2AlC MAX-fasen syntetisert ved sintring av en pulverblanding av de tre elementene V, Al, C før Al-laget i MAX-fasen ble selektivt etset ut ved bruk av en konsentrert HF-løsning, for å danne flerlags V_2C MXene. Noe av det etsede materialet ble deretter behandlet med en tetrabutylammoniumhydroksid (TBAOH) løsning og delaminert. Strukturen, morfologien og elementinnholdet til de syntetiserte materialene ble karakterisert vha. røntgenspektroskopi (XRD), sveipe-elektronmikroskopi (SEM) og energidispersiv røntgenspektroskopi (EDX). Alle de aktive materialene ble deretter brukt til å danne katoder ved å dryppe dråper av en blanding som inneholdt det aktive materiale på karbonpapir, og som senere ble satt sammen til knappecellebatterier og testet ved elektrokjemisk sykling.

De mest kritiske aspektene for å oppnå faserent V_2C MXene med høyt utbytte, en passende partikkelstørrelsesfordeling og morfologi, viste seg å være sterkt avhengig av syntese-prosedyren til V_2AlC MAX-fasen, i tillegg til den benyttede etsetiden og HF-konsentrasjonen. Ved bruk av en elektrolytt bestående av 0.4 M all-fenylkompleks løst i tetrahydrofuran (APC:THF) viste de ulike aktive materialene begrenset katodekapasitet (< 4 mAh/g), noe som tyder på ubetydelig Mg-ioneinterkalering inn i V_2C-strukturen. TBAOH-behandlingen av V_2C førte til en økning av mellomlagsavstanden med 2.2 Å, og delamineringen resulterte i en tydelig redusering av partikkelstørrelsene, men ingen av disse behandlingene endte opp med å forbedre syklingsytelsen betraktelig. Derimot, med tilsats av 0.4 M LiCl i elektrolytten (APC/LiCl:THF) økte den oppnådde kapasiteten betydelig (70 mAh/g etter 50 sykluser), noe som demonstrerte interkalering av mindre ladningstette Li-ioner. Den begrensede kapasiteten som ble oppnådd med V_2C MXene, ble tilskrevet høye migreringsbarrierer for Mg-ionene, og fremtidig innsats bør derfor rettes mot å senke disse barrierene, samtidig som en høy spenning bør opprettholdes. Med optimaliserte termineringsgrupper, mellomlagsavstander og morfologi av V_2C-partiklene, kan V_2C fortsatt vise seg å være et lovende katodemateriale som muliggjør energitette OMBer og Mg-Li hybridbatterier.

Contents

Chapter 1

Introduction

Rechargeable batteries have become an important part of today's society, be it in portable electronic devices, power-tools, off-grid electrical applications, electric vehicles (EVs) or energy storage devices. They also represent one of the most feasible ways of stabilizing the energy output from fluctuating energy sources, and will therefore play a significant role in the transition from fossil energy (oil, coal, gas) towards renewable energy sources (wind, solar, etc.). Hence, rechargeable batteries may help to mitigate climate change, which is one of the most prominent global challenges today [1].

The first example of a practical rechargeable battery was the lead-acid battery, invented by Gaston Planté in the year of 1859 [2]. Due to its low cost and high power density, lead-acid batteries still holds most of the market share for rechargeable batteries [3, 4], mainly used for automotive starters. However, because of its limited energy density and relatively poor cyclability [5], it is left unsuitable for new energy demanding applications, such as electric vehicles and grid energy storage [6, 7]. Meanwhile, new technologies have arisen, and today the dominant rechargeable battery technologies comprise of nickel-cadmium (NiCd), nickel-metal hydride (NiMH) and lithium-ion batteries (LiB), in addition to the lead-acid batteries. Due to their unmatchable combination of high energy density and high power density, LiBs have become the technology of choice, especially for the booming market of EVs [8]. LiBs therefore represent the fastest growing rechargeable battery technology, and is expected to continue its growth and in some years be dominant in the battery market [3, 9].

Nevertheless, there are some important challenges with LiBs that may hinder its rapid expansion. Firstly, with the use of flammable electrolytes at high operating voltages, together with the possibility of dendrite formation [10], several cases of LiB fires have been reported [11],

which has resulted in a ban of LiBs in flight luggage [12]. As these flames also have been found to produce toxic fluoride gas emissions [13], serious questions regarding the safety of LiBs have arisen [14]. In addition, due to the limited abundance of raw materials, together with the difficulty of recycling, it is unsure whether this technology can respond to the strongly increasing demand for rechargeable batteries [15]. I.e. the global electric vehicle sales have escalated from less than 10 000 in 2010 to 774 000 in 2016, surpassing 2 million cumulative sales [16], representing a drastic increase in the utilization of rechargeable batteries. This again opens up for the rise of different battery technologies based on more abundant and less expensive materials, and possibly safer technologies, such as sodium-, magnesium- and aluminum batteries.

Some of the most promising alternative battery technologies are based on multivalent ions such as Ca^{2+}, Mg^{2+} and Al^{3+}, due to the fact that they can transport more charge per ion and thus increase the capacity of the batteries [17]. Rechargeable magnesium batteries (RMBs) have been one of the most prominent contenders to LiB, partly due to the possibility of using Mg anodes without dendrite formation upon charging [18]. The use of a metal anode opens up for a 6 fold increase in the capacity compared to the graphite anodes used in todays commercial LiB. Considering that magnesium is one of the most abundant metals in the earth's crust, RMB would avoid the problem with scarcity, and at the same time open up for less expensive batteries. Additionally, due to the lack of dendrite formation, RMBs also represent a safer alternative than LiBs. With the first practical RMB being demonstrated by D. Aurbach et al. in the year of 2000 [19], this also represents a relatively young battery technology, with a lot of research possibilities. However, since then, only minor improvements in energy density has been accomplished, which has been attributed to the great challenge of finding suitable electrolytes to the Mg metal anode and cathode materials that can host the divalent Mg-ions.

An interesting candidate to be used as RMB cathodes is the new group of two-dimensional materials, known as MXenes, which was first discovered in 2011 [20]. MXenes are formed by the selective etching of the "A"-layer from its layered MAX phase precursor, where the "M" material describes a transition metal (i.e. Ti, Cr, V), "A" is a group 13 or 14 element (i.e. Al, Si) and "X" represents either C or N. Due to the large amount of MAX phase precursors, a similar large range of MXenes have been synthesized, offering possibilities to fine tune material properties. As they have demonstrated to be electrically conductive [21], abundant [22], hydrophilic and stable as nearly atomically thin sheets [23], application possibilities have not been hard to find. Gas- and biosensing [24, 25], gas separation [26], water purification [27], supercapacitors [28], catalyst for water splitting [29, 30, 31] are only some of them, and due to their ion intercalating properties, they have also drawn significant interest towards

energy storage applications [32, 33].

In this work, the relatively unexplored V_2C MXene has been investigated as a cathode material for RMB. As it previously has been shown to host Li-ions [34, 35], Na-ions [36] and even trivalent Al-ions [37], it also opens up for the possibility of hosting Mg-ions. With one of the highest theoretically calculated cathode capacities of all known MXenes [38, 32], it is a promising material for RMB cathodes.

Aim of this work

The overall goal of this project was to explore the possibility of using the V_2C MXene as a new intercalating cathode material for rechargeable magnesium batteries. In order to make this possible, the first subgoal of the project was to successfully synthesize V_2C. Since the MXene materials have not been previously synthesized at the department, extra effort has been designated to the development of a successful synthesis route, in order to obtain V_2C of sufficient phase purity and yield.

After successful synthesis of V_2C, the second subgoal was to assemble coin cell batteries with V_2C as the cathode material, followed by electrochemical characterization, in order to determine its capacity and operating voltage.

As the initial results indicated limited capacity, efforts were directed to exploring different methods to enable substantial magnesium intercalation, in order to evaluate V_2C's applicability as cathode material in rechargeable magnesium batteries.

Chapter 2

Theory

2.1 Introduction to batteries

2.1.1 Working principle

A battery is defined as: "a container consisting of one or more electrochemical cells, in which chemical energy is converted into electricity and used as a source of power" [39]. One such cell, known as a galvanic cell, is shown in Figure 2.1 and consists of two electrodes that are physically separated by an ion conducting electrolyte, while at the same time being connected through an external electrical circuit. During discharge of the cell, electrochemical reactions take place on both of these electrodes, where the one termed as the anode is being oxidized (loses electrons), while the other is termed as the cathode and is reduced (receives electrons). The combined reduction and oxidation reactions are abbreviated "redox" reactions, and due to a difference in the electrochemical potential of these reactions, an electric potential difference between the electrodes arises. During discharge of the cell, this electric potential difference causes electrons to flow from the anode to the cathode, and with an electrically insulating electrolyte, the flow of electrons are forced through the external circuit, where it can do work[40].

In order to have continuous redox reactions, the current flow needs to be accompanied by a flow of ions in the electrolyte. This ionic current between the electrodes retains the potential difference between the electrodes until one of the electrodes is unable to be reduced/oxidized any further. When this happens, the current flow stops, and the cell is unable to continue

doing work.

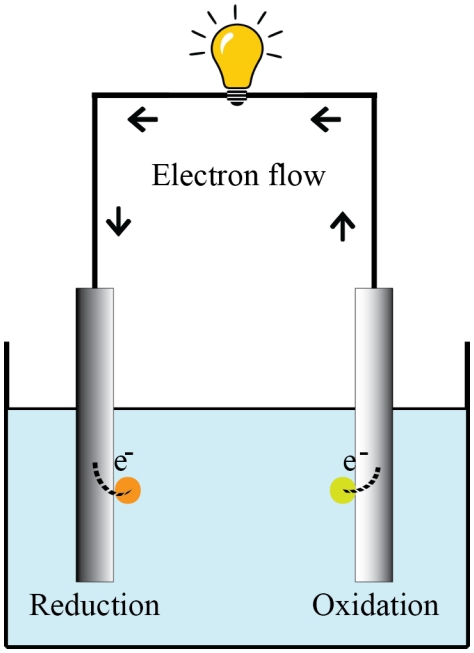

Figure 2.1: Illustration of a simplified galvanic cell, showing the separated reduction and oxidation reactions taking place on the two electrodes during discharge, resulting in a current of electrons through the external circuit.

The two groups of electrochemical cells that can form batteries are divided into primary and secondary cells. A primary cell is a basic galvanic cell, where the electrochemical reactions taking place during discharge form non-reversible products and thereby cause the cell to be non-rechargeable. A secondary cell is also a galvanic cell, but unlike primary cells the electrochemical reactions are fully reversible. By applying a current in the opposite direction to the discharge current, the cell may therefore be charged to its initial state, enabling many cycles of discharge and charge per cell. Unless other specified, only secondary batteries will be addressed in this thesis, and the terms "battery" and "cell" may therefore be used as a simplified way of describing a secondary battery/cell.

In order to increase the energy density of batteries, the volume is usually minimized, which also results in a reduction of the distance between the two electrodes. In order to prevent physical contact between the electrodes and thus short circuiting the battery, a porous membrane is utilized to create a physical barrier. Such a membrane is usually denoted as a "separator", and comprise of several materials with varying application areas. Wettability for different types of electrolytes, pore size, stability etc. are all parameters that must be optimized for each application [41].

Another component that may be needed in a battery cell is a current collector, which has the basic property of transferring electrons between the electrode and the electric circuit. If the electrode material is unable to form free standing films, the current collector may work as a substrate onto where the material can be deposited. In addition, if the electrode material is not electrically conductive, the current collector helps to reduce the electrons travel distance within a high resistance material. Different metal foils are common current collectors due to their high conductivity, combined with their suitable reduction potentials [42].

When combined to form a battery cell, all of these different components need to be compatible with each other, in order for a battery cell to function properly. A mismatch between two or more components is enough to prevent the flow of electrons and/or ions and thus stop the whole cell from working. For example, if the electrolyte does not wet the separator, the ions will not be able to flow between the electrodes, and the redox reactions will eventually stop. Furthermore, all the components need to be both chemically and electrochemically compatible, in order to avoid unwanted side reactions. This illustrates some of the complexity of battery science, as changing one component might have an effect on all the other battery constituents. On the other hand, it also opens up for a lot of possibilities, as there are endless combinations of possible battery compositions.

2.1.2 Battery performance parameters

There are several important battery performance parameters, and which one is most critical, depends on the specific application. Commercial batteries come in different shapes and sizes, ranging from single coin cells to batteries the size of a football field [43]. The latter, however, consists of a great amount of smaller battery cells stacked together, and in theory there is practically no limitations to the amount of cells that can be stacked together, except for material abundance and space to store it. Increasing the number of cells in a battery, increases the energy it can store. However, increasing the cell stacking also increases the volume and weight of the total battery, which will make the batteries inapplicable for certain applications. This illustrates the importance of good figures of merit that are universal to all battery technologies, which will be explained in this section.

Generally, there are several factors that are important for the commercializability of a rechargeable battery. The most critical parameters are summarized below:

- Specific power output & input
- Cycle lifetime
- Shelf life
- Volumetric energy density
- Gravimetric energy density
- Safety
- Efficiency
- Low cost
- Environmentally friendliness

where specific power output & input represents the power (mW/g) at which the battery can be (dis)charged [40]. Cycle lifetime is used to describe the amount of cycles that a battery can perform before the capacity is reduced to a certain percentage of its initial value (usually set to 80% for electric vehicles). Shelf life describes how long a battery can be stored without degradation.

Which of the parameters that are most important varies with the battery application. For applications such as electric vehicles, portable electronic devices etc., volumetric and gravimetric energy density is of utmost importance, as the batteries are to be transferred with the device, and therefore should be as small and light weight as possible. Moreover, safety is a serious concern, considering that the devices usually are utilized by humans. On the contrary, for energy storage for the electric grid, weight, volume and safety of the batteries are not equally important, as they may be stored stationary. Instead, lifetime and efficiency of the batteries become more important, as the batteries would be needed to store energy over thousands of cycles with limited losses. Common for all applications is the desire to have low cost batteries made by environmentally friendly materials and processes.

The total energy that can be delivered by a cell is a product of the total amount of charge it can provide and the voltage by which these charges can be delivered. During discharge of a battery, there is a time dependent electric current, $I(t)$, transporting electrons (negative charge) from the anode to the cathode. The energy, E, can then be found from [44]

$$E(I) = \int_0^{\Delta t} IV dt, \tag{2.1}$$

where Δt represents the time needed to completely discharge the battery, and V represents the operating voltage of the battery. This voltage is a combination of the open-circuit voltage between the two electrodes without any external load, together with an overpotential which will be described below. The open-circuit voltage, V_{OC}, comes from the difference in electrochemical potential between the electrodes, given by [40]

$$V_{\mathrm{OC}} = \frac{\mu_{\mathrm{A}} - \mu_{\mathrm{C}}}{e} \tag{2.2}$$

where e is the elementary charge, while μ_{C} and μ_{A} represent the electrochemical potential of the cathode and anode, respectively. However, during (dis)charge of the cell, the actual operating voltage at which the redox reactions take place, usually differs from the theoretically calculated value, where the difference comes from the cell's overpotential [45]. During discharge, the operating voltage is reduced, and when the cell is being charged the operating voltage is increased, which leads to an excess amount of energy that is lost in the cycling process.

In general, the overpotential is caused by the system being under non-ideal conditions (away from thermodynamic equilibrium). It can be explained through the polarization effect during cycling, which depends on both the current density and the internal battery resistance. For example, if a high current density is utilized during discharge, an excess amount of electrons reach the cathode before enough ions are able to migrate through the electrolyte and accompany them. This local charge difference creates a polarization within the cell and thus reduces the operating voltage of the battery as compared to the open-circuit voltage. The opposite voltage shift occurs during charge of the battery, where the polarization increases the necessary voltage to charge the battery. As the internal resistance varies with the state of (dis)charge, $0 < q < 100\%$, the operating voltage during (dis)charge is given by [40]

$$V_{\mathrm{dis}} = V_{\mathrm{OC}} - \eta(q, I_{\mathrm{dis}}), \tag{2.3}$$

$$V_{\mathrm{ch}} = V_{\mathrm{OC}} + \eta(q, I_{\mathrm{ch}}), \tag{2.4}$$

where η is the overpotential, with $\frac{\partial \eta}{\partial I} > 0$, while I_{ch} and I_{dis} are the currents during charge and discharge, respectively. Noteworthy, the internal battery resistance, and thus also the overpotential of the cell, greatly depends on the electrode materials. This is generally related to their varying catalytic ability [46] and the different electrode/electrolyte interfaces that occur [47].

The total charge that can be stored and delivered is usually termed the battery's capacity (expressed in mAh), Q, and is given by

$$Q(I) = \int_0^{\Delta t} I dt, \tag{2.5}$$

where I and Δt now represent the (dis)charge current and -time. The relation between the variables in equation (2.5) is generally not linear, where use of higher currents usually leads to a reduced battery capacity. This arises from the diffusion limitation of ion conductivities at higher currents [45], which results in a difference in the electric and ionic currents and therefore polarization effects within the cell. As stated in Equations (2.3) and (2.4), higher currents results in more polarization, which reduces (discharge) or increases (charge) the operating voltage. This further results in a shortened (dis)charge time, as the cut-off voltages are reached earlier than what would be the case for lower currents. However, by again using a lower current, the apparent capacity loss will be recovered [48].

An aspect that is not included in Equation (2.5), is the fact that the total battery capacity is dependent on both electrodes in the system, and limited by the electrode with the lowest capacity. With an imbalance between the electrode capacities, the excess capacity of one electrode will remain unused, which results in an excess amount of material in the battery. Balancing the electrode capacities is therefore critical upon optimizing the specific capacity (expressed as mAh/g) of the battery, which is one of the most important parameters when comparing battery performance. This theoretical specific capacity of a balanced battery is given by

$$\text{Battery specific capacity (mAh/g)} = \frac{C_{\text{A}} C_{\text{C}}}{C_{\text{A}} + C_{\text{C}}}, \tag{2.6}$$

where C_A and C_C represent the specific capacities of the anode and cathode, respectively. Using Faraday's law of electrolysis, which states the proportionality between charge and mass in electrochemical reactions, the theoretical specific capacities of each of the electrodes can

be calculated [44]. Rewritten from [49], this value is given by

$$\text{Electrode specific capacity (mAh/g)} = \frac{nF}{M_w}, \tag{2.7}$$

where n is the number of electrons taking part in the electrochemical reaction, M_w is the atomic or molecular mass ($\mathrm{g\,mol^{-1}}$) of the reacting compound and F is the Faraday constant, which describes the magnitude of electric charge per mole of electrons. Converting to more useful units, this constant equals to an equivalent of 26801.5 mAh $\mathrm{mol^{-1}}$. An expression for the volumetric capacity (expressed as $\mathrm{mAh/cm^3}$) is obtained by multiplying Equation (2.7) with the density, ρ ($\mathrm{g/cm^3}$), of the reacting compound:

$$\text{Electrode volumetric capacity (mAh/cm}^3) = \frac{nF}{M_w} \times \rho \tag{2.8}$$

The term used to describe the efficiency of the charge transfer in a system fascilitating electrochemical reactions is usually the Coulombic efficiency. With Q_{dis} and Q_{ch} being the battery capacities during discharge and charge, respectively, the Coulombic efficiency, CE, is defined as

$$\mathrm{CE} = 100 \times \frac{Q_{\mathrm{dis}}}{Q_{\mathrm{ch}}}. \tag{2.9}$$

An efficiency lower than 100% indicates that some unwanted side reactions are taking place, accounting for some of the charged capacity. These irreversible capacity losses , ICL, then describes the amount of capacity that is lost in a cycle and is given by

$$\mathrm{ICL} = Q_{\mathrm{ch}} - Q_{\mathrm{dis}}. \tag{2.10}$$

After multiple cycles, the amount of irreversibly lost capacity increases. The cumulative irreversible capacity losses, CICL, after n cycles, is then given by

$$\mathrm{CICL} = \sum_n (Q_{\mathrm{ch},n} - Q_{\mathrm{dis},n}). \tag{2.11}$$

The energy efficiency also gives information about energy losses during cycling, including the effect of overpotentials, and can be explicitly defined using Equations (2.1), (2.3) and (2.4):

$$\text{Energy efficiency} = 100 \times \frac{\int_0^{\Delta t} IV_{\text{dis}} dt}{\int_0^{\Delta t} IV_{\text{ch}} dt}. \tag{2.12}$$

2.1.3 Terminology

To ease the readability of this thesis, important terms that have not yet been described will now be presented.

First of all, the definitions of anode and cathode will be clarified. In secondary batteries both electrodes will experience reduction and oxidation, depending on whether the battery is being charged or discharged. To prevent any misunderstandings, the convention for galvanic cells will be used - the anode and cathode are the electrodes at which oxidation and reduction takes place during discharge of the battery, respectively.

Galvanostatic cycling is one the key characterization techniques of a battery. It involves the measurement of voltage over time using a constant current, where the (dis)charge rates is given in terms of "C-rates". This is a measure of the rate at which a battery is (dis)charged relative to its maximum capacity. A C-rate of N, where N is a positive real number, thus represents the current that will (dis)charge the battery in $\frac{1}{N}$ hours. For a battery with a specific capacity of 200 mAh/g, a 0.5 C-rate would therefore represent a current of 100 mA/g.

When comparing the capacities of different electrode materials, usually the specific capacity (expressed in mAh/g) and volumetric capacity (expressed in mAh/cm^3) are utilized. They usually represent the total capacity per mass/volume of the active electrode material, and represents a way of comparing electrode materials independent on the electrode size/weight. However, as usually only the mass/volume of the active material is included in the obtained capacity, loading (mg/cm^2), porosity etc. need to be considered in order to predict the specific or volumetric capacity that can be expected for a complete and practical battery system.

2.2 Rechargeable magnesium batteries

2.2.1 Overview

Rechargeable magnesium batteries (RMB) consist of the same general components as most of the other battery technologies, where the fundamental difference is the ions that are used for the charge transfer, namely magnesium ions. The main motivation for RMB technology is as follows:

1. Multivalent cations (Mg^{2+})
2. Possible to use Mg metal anode
3. The abundance of Mg

The multivalency of the Mg-ions leads to that each ion transports twice the charge as compared to Li^+ ions. Since they are of similar size, the theoretical volumetric capacity is doubled for RMBs. However, as the Mg-ions are almost four times heavier, the specific capacity would appear to be limited to half of what is theoretically achievable for Li-ions.

In comparison to lithium metal, magnesium metal show less dendrite formations upon cycling, which allows for the use of a metal anode in RMBs [50]. Dendrites are tree like formations of i.e. Li metal that can grow from the anode, and with prolonged cycling, could puncture the separator and reach the cathode. This would lead to short circuiting of the battery, and possibly cause thermal runaway. Mg metal on the other hand, deposits homogeneously during charge [17]. With a specific and volumetric capacity of around 2046 mAh/g and 3833 mAh/cm^3, Mg metal anodes have the highest theoretical specific capacity of all RMB anode materials [51]. Additionally, using a Mg metal anode might eliminate the need of the typical copper current collector, cutting cost and dead weight even further. In comparison, the commercially used graphite anode for Li-ion batteries has a specific capacity of only 350 mAh/g [52]. Furthermore, Mg metal has a relatively low electrode potential of $-2.37\,V$ [53], which together with the high theoretical capacity, enables the possibility for energy dense batteries. Figure 2.2 illustrates a general RMB with a Mg metal anode, a separator, an electrolyte and an intercalation-based cathode material.

As mentioned in Chapter 1, there are concerns related to the abundance of some of the raw materials used for LiBs. Mg on the other hand, is the eight most abundant metal in

the earths crust and around 10 000 times more abundant than Li [54]. In a long term perspective, RMB technology may therefore represent a promising alternative to LiBs, as the demand for batteries is prospected to escalate [8]. The high abundance of Mg may also enable for the production of low cost batteries, which is an important reason for the interest in RMB technology.

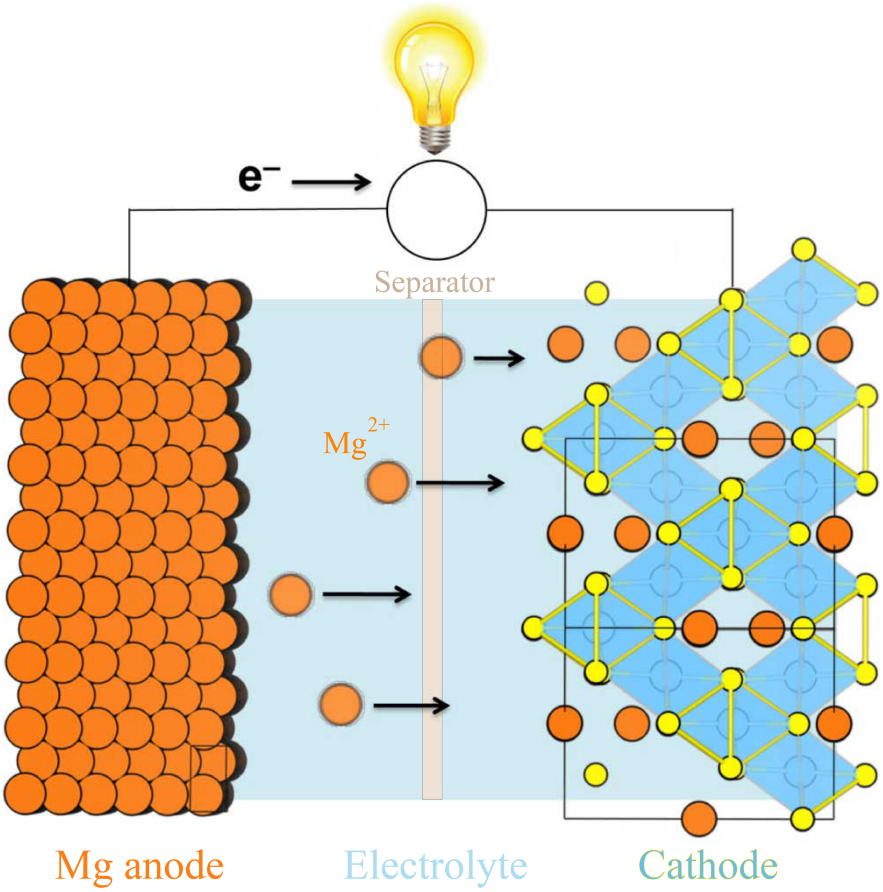

Figure 2.2: Schematic of a typical rechargeable magnesium battery with a Mg anode, an electrolyte transporting the Mg-ions, a separator and an intercalation-based cathode material that can host Mg-ions. Adapted from [17].

2.2.2 Technology status

The first practical RMB was created in 2000, when D. Aurbach et al. utilized the Mo_6S_8 Chevrel phase as cathode material and an electrolyte based on organohaloaluminate salts, in order to obtain a capacity of around 100 mAh/g for more than 2000 cycles [19]. However, with the main focus being directed towards improvements of LiBs, only minor improvements in RMB technology have been achieved since then, still leaving RMB a relatively new and

unexplored technology. As a result of the possibility of improved energy density and reduced costs compared to LiBs, several of the leading car companies have committed their research into RMB technology [55, 56]. This has also lead to a significant increase in the number of publications on RMBs the last 8 years (Figure A.10).

The main challenges with RMB technology are to find suitable electrolytes that easily solve and transport Mg-ions, and cathode materials that allow for Mg-intercalation [57]. The divalent nature and small size of the Mg-ions causes a high charge density, which makes the ions easily attract and interact with oppositely charged molecules and repel those of similar charge. This leads to a slow ion migration in both the electrolyte and cathode materials, in addition to extremely sluggish reaction kinetics [58, 59].

2.2.3 Anode

Even though Mg metal may seem like the clear choice for anode material, there are still some challenges associated to its use. These challenges are mainly related to the low electrode potential, and therefore the high activity of the Mg metal. Finding electrolytes that allows for Mg deposition and dissolution while being stable with the metal anode has therefore turned out to be a bottleneck for the development of RMB technology [17]. Aqueous electrolytes would result in the metal surface to oxidize, and thereby form an impermeable oxide layer on its surface. As most non-aqueous electrolytes have been found to form impermeable solid electrolyte interface (SEI) layers as well, the number of suitable electrolytes has reduced drastically, and will be discussed in the upcoming section. In comparison, the SEI layers that are formed in LiBs allow for Li permeation, and are vital to prevent continuous electrolyte degradation [40].

To get around this problem, different approaches have been attempted. Some have reported the use of intercalation anodes, such as spinel $Li_4Ti_5O_{12}$ and Li_3VO_4, achieving discharge capacities of around 175 mAh/g and 318 mAh/g, respectively [60, 61]. However, the insertion anodes already reported tend to suffer from low coulombic efficiencies and low capacities at higher discharge rates, which has been explained by the slow kinetics of the Mg-ions [57]. Furthermore, in order for RMBs to be viable products compared to the other battery technologies, utilization of the advantages that Mg metal anodes offer might be a necessity. Therefore, most of the RMB related research focuses on finding electrolytes that are compatible with the metal anode.

One recent report also claims to have formed an artificial interface on the Mg anode surface which allows for reversible cycling of a Mg/V_2O_5 full cell in a water-containing, carbonate-based electrolyte [62]. This might open up a new world of possible electrolyte compositions for RMBs, concluding the applicability of the metal anode. However, more research needs to be completed to verify the performance of these artificial interfaces.

Noteworthy, due to the high specific/volumetric capacity of Mg metal anodes, RMBs are generally cathode limited. Far less anode material than cathode material is needed in order to balance the electrodes, and thereby achieve the highest possible full cell specific capacity, calculated by Equation (2.6). For comparison, when balancing the Mg metal anode (2046 mAh/g) with the chevrel phase cathode mentioned earlier (100 mAh/g), the chevrel phase cathode would require more than 20 times the mass of the Mg metal anode.

2.2.4 Electrolyte

There are several requirements that need to be met for an electrolyte to be applicable for RMBs, where the most prominent ones are listed below:

1. Solve Mg-ion salts or complexes containing Mg-ions
2. Suitable interaction energies between Mg-ion and surrounding complexes
3. High Mg-ion conductivity
4. Electrically insulating
5. High electrochemical stability
6. High chemical stability
7. Non-corrosive
8. Non-toxic and -flammable
9. Low cost

Probably the most important requirement for the electrolyte is related to whether or not it actually can encompass Mg-ions. In order to allow Mg dissolution and deposition on the metal anode, and intercalation of Mg-ions in the cathode, solvation of the Mg-ions is

necessary. However, the interaction energy between the Mg-ions and the solvent complexes has to be balanced. If it is too weak, the solvent may not be able to dissolve the Mg-salt, and if it is too strong, the intercalation of Mg-ions into the cathode will be difficult [63]. Too strong bonds might result in an overpotential for the desolvation of Mg-ions, reducing the energy efficiency of the battery.

If the electrolyte is able to both hold, transfer and deposit the Mg-ions, the next concern relates to whether the electrolyte remains stable during cycling. The electrochemical potential window of an electrolyte represents the potential gap between where the electrolyte is oxidized and reduced, and thus represents the potential window where the electrolyte is thermodynamically stable. These oxidation and reduction limits are determined by the highest occupied molecular orbit (HOMO) and the lowest unoccupied molecular orbit (LUMO) of the electrolyte. Figure 2.3 illustrates the relevant electrochemical potentials of a full cell. For an electrolyte to be thermodynamically stable upon cycling, the HOMO level needs to be below the oxidation potential of the cathode in order to prevent oxidation of the electrolyte, while the LUMO level needs to be higher than the reduction potential of the anode in order to prevent electrolyte reduction. If μ_{A} is above the electrolyte LUMO, the electrolyte will be reduced, unless the anode-electrolyte reaction becomes blocked by the formation of a passivating SEI layer [40].

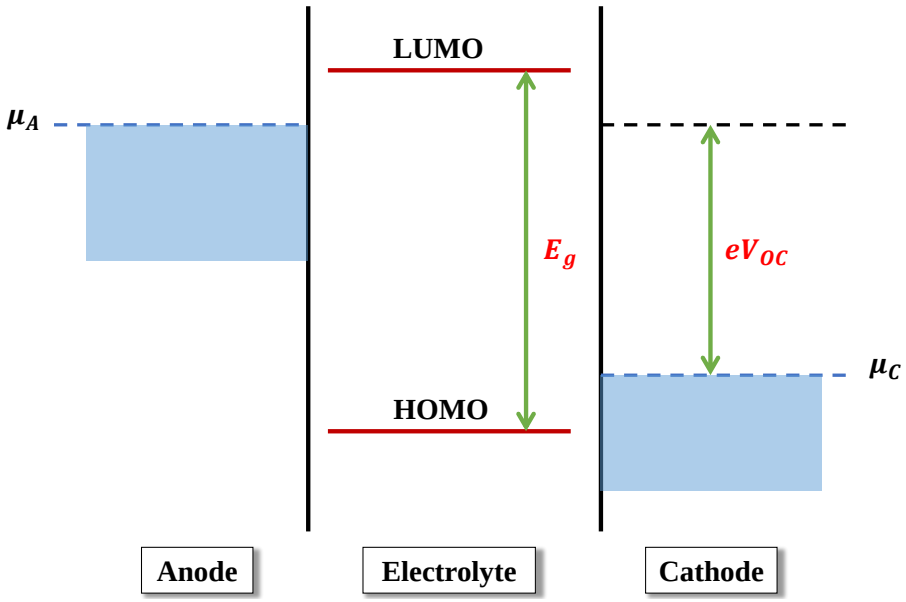

Figure 2.3: The electrochemical stability window (E_g) of the electrolyte shown by the difference between the HOMO and LUMO electron states. The open-circuit voltage (V_{OC}) is presented as the difference between the electrochemical potential of the anode (μ_{A}) and the cathode (μ_{C}). Inspired by [40].

The chemical stability of an electrolyte is also an important factor, preventing the general degradation of either the electrolyte or any of the other cell components. The electrolyte should ideally be able to maintain its properties (ion conductivity, electrochemical window, Mg solubility, etc.) within a range of temperatures, and should also be able to last for prolonged cycling without degradation. Corrosion of metal components of the cell should therefore be prevented.

While the previously mentioned requirements describes what is needed for a RMB to function, the remaining requirements generally relates to the commercializability of RMB technology. In order to have a viably battery technology, the safety of the battery, and thus also of the electrolyte, needs to be addressed. Non-toxic, -flammable and low cost electrolytes are therefore not essential for a RMB, but instead important factors that need to be addressed regarding the development of the technology.

Efforts so far

The first electrolytes that was found to allow for Mg dissolution and deposition were solutions of organomagnesium compounds (known as Grignard reagents) in ethereal solvents, found by Gregory et al. in 1990 [64]. They also found ethereal solvents to be the only solvents that did not form impermeable layers on Mg metal anodes. From then, it took 10 years before Aurbach et al. managed to increase the anodic stability of the Grignard reagents by combining them with aluminum-based Lewis acids solved in tetrahydrofuran (THF) or polyethers of the glyme family [19]. The continued work on Grignard electrolytes then lead to the use of organomagnesium chloride complexes, such as the "all phenyl complex" (APC) [65, 66], the "magnesium aluminum chloride complex" (MACC) [67], and the "dichloro complex" (DCC) [68]. All of these electrolytes have shown a high degree of reversible Mg plating and stripping, with anodic stabilities of around 3.1 V [69]. However, even though all of these complexes may be utilized for state-of-the-art RMBs, there are some drawbacks related to their content. Due to the presence of chloride, these electrolytes have been found to cause severe corrosion of noble metals at potentials exceeding 2 V vs Mg [51, 70]. Additionally, the solvents used for these electrolytes are often volatile, where the most commonly used solvent is the THF (boiling temperature of 66 °C [71]), which results in limited safety improvements as compared to LiBs.

Another limiting factor with these Grignard electrolytes is their incompatibility with high voltage cathode materials [51, 72]. In order to develop electrolyte solutions with higher anodic stabilities, inspiration was taken from the world of LiBs to use non-organometallic compounds. However, most of them struggle with very low solubility in ethereal solvents, except for magnesium bis trifluoromethanesulfonyl imide ($Mg(TFSI)_2$), which has demonstrated good properties when dissolved in different glymes and therefore gotten a lot of interest [73, 74, 75].

In the search for optimized electrolytes, numerous electrolytes have been tested and contribute to some of the challenges. At Toyota R&D, they discovered a group of promising halogen-free electrolytes [76, 77, 78], such as Mg carboranes and boron-clusters, showing less corrosion than the above-mentioned electrolytes with some of the highest reported anodic stability windows (3.8-4.0 V) to date [79]. Additionally, Canepa et al. have managed to demonstrate good ionic conductivity (0.01-0.1 mS/cm^2) for Mg-ions in a magnesium scandium selenide spinel solid state electrolyte at room temperature [80], and thereby opening up for a new range of possible non-flammable electrolytes.

To sum up, several electrolytes have been shown to successfully dissolute and deposit Mg-ions, where most of them utilize ethereal solvents, due to their inertness towards Mg metal. The Mg-salts vary substantially, but some of the most commonly used are APC and MACC, and for high voltage cathodes $Mg(TFSI)_2$. Even though these electrolytes show high degree of reversibility, a lot of research is needed in order to improve the performance of RMB electrolytes.

2.2.5 Cathode

The main performance criteria for a viable RMB cathode material are listed as follows:

1. High reversible specific and volumetric capacities
2. High operating potential vs. the anode
3. Fast Mg-ion diffusion
4. High electrical conductivity
5. Chemical stability
6. Long cycle life and shelf life
7. Non-toxic
8. Abundant materials
9. Low cost
10. Environmental friendly fabrication process

Most importantly, a RMB cathode material needs to be able to host Mg-ions. The incorporation of Mg-ions can follow the typical intercalation-type redox reactions, conversion reactions or alloying reactions. The number of Mg host sites that the cathode material contains determines its capacity, and is one of two factors that influence the energy density, as discussed in Section 2.1.2. For the operating potential to be high, the oxidation potential of the cathode should be as low as possible. The power density of the cathode is given by the electrical conductivity and Mg-ion diffusion of the cathode.

As mentioned, the fundamental challenge with RMB cathodes comes from the high charge density of the Mg-ions, which due to their attraction to the host material and strong repulsion between themselves results in a slow ion migration [57]. For this reason, it has been difficult to find materials that both allow for high voltage operation, and show a significant amount of retained capacity [17].

Efforts so far

The first published study of Mg-ion intercalation materials was reported in 1989, when Gregory et al. studied a variety of transition metal sulfides, borides and oxides [64]. They discovered a set of materials including ZrS_2, Mn_2O_3, RuO_2 and Co_3O_4, that displayed reasonable combination of potential vs. Mg and capacity. Since then, several intercalation-based host materials consisting of different oxides and sulfides were identified [81, 17], but no real breakthrough came before Aurbach et al. demonstrated the successful use of a Chevrel Mo_6S_8 structure [19]. The Chevrel structure demonstrated less than 15% capacity fade over 2000 cycles with a capacity of around 70 mAh/g. Since its first use in 2000, Mo_6S_8 has remained as one of the leading materials for RMB cathodes. Still, there has been no commercial applications, due to its low operating voltage vs. Mg (1.1 V) and thereby limited energy density.

In general, the different groups of functioning cathode materials can be separated into chalcogenides and oxides [17]. The leading materials for each of the categories, together with their limitations, will be presented here.

The chalcogenide cathode materials usually consist of transition metals with S or Se anions, such as the already mentioned Chevrel phase. These materials have demonstrated some of the best Mg-ion mobilities of all cathode materials, which partly has been described by their more polarizable anion networks as compared to oxides [82, 80, 51]. TiS_2 is the material that has demonstrated the highest stable capacity of these materials at 115 mAh/g [83, 84]. However, similar to most of the materials within this group, it has an operating voltage that is too low (<1 V) to be a competitive cathode material. The chevrel phases also suffer from Mg-ion trapping over time [85, 86].

In order to increase the operating voltage of the cell, attempts have been made to utilize transition metal oxides. Several structures have been tested, such as different polymorphs of MnO_2 [87, 88] and different forms of V_2O_5 [89, 90], where all of them show increased operating voltages (> 1.5 V), as well as high capacities on the initial cycles (>150 mAh/g). However, general for most of them is a drastic capacity fade for the continued cycles. Interestingly, it has been found that the capacities of these materials strongly depend on the water content in the electrolyte, showing a significant increase compared to the water-free electrolytes [91, 87]. On the other hand, this limits the compatibility with Mg metal anodes, as it is found to be unstable with water concentrations exceeding 0.1% in non-aqueous electrolytes [92]. Another challenge with these cathode materials is the limited electrolyte compatibility with high voltage cathodes, as already mentioned in Section 2.2.4.

Finding suitable cathode materials to host Mg-ions has become one of the main challenges related to RMB technology. It appears that having large capacities and high voltages, may come on the cost of low cycle life. In recent years, a new group of materials known as MXenes have emerged and provided possible candidates for RMB intercalation cathode materials. These materials will be discussed further in the upcoming section.

2.3 MXenes

2.3.1 Background

MXenes are a new type of two-dimensional material that is usually synthesized through selective etching of what is known as "MAX phases". These MAX phases have their name from their general chemical formula; $M_{n+1}AX_n$, where $n = 1$, 2 or 3, the "M"-atom represents a transition metal (i.e. Ti, Zr, V,Nb), the "A"-atom represents a group 13 or 14 element (usually Al or Si), and the "X"-atom represents carbon and/or nitrogen[93]. These atoms are arranged in layered hexagonal crystal structures where $M_{n+1}X_n$ layers are interlayered by pure A layers, as illustrated in Figure 2.4 [94].

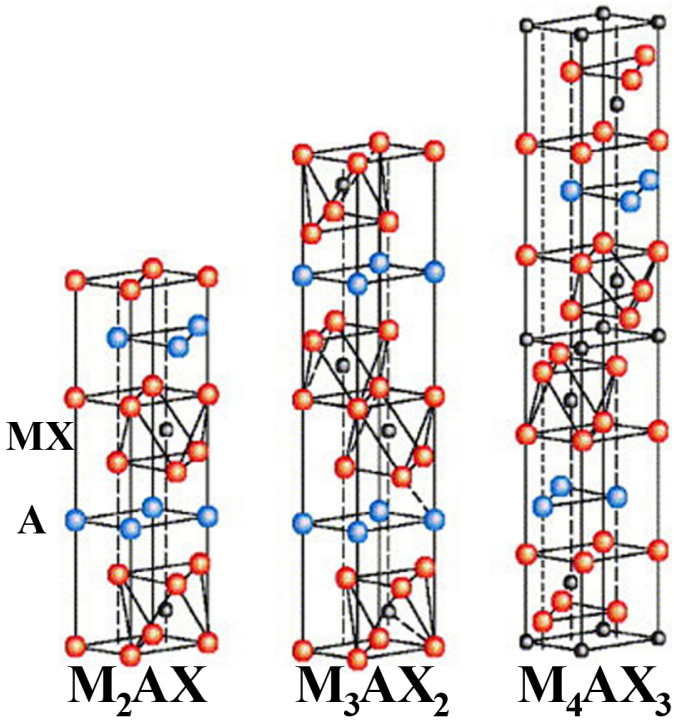

Figure 2.4: MAX phase structure. Reused from [95]

The discovery of MXenes was as a result of a project between Y. Gogotsi and M. W. Barsoum at Drexel University, who tried to apply MAX phases as anode material for Li-ion batteries. However, it appeared that the bonds between the MAX phae atoms were too strong to let the Li-ions intercalate between them, and they realized they needed to somehow open up the structure in order to allow the ions to pass through [96]. In 2011, M. Naguib etched the Ti_3AlC_2 MAX phase using an aqueous HF-solution, which resulted in the selective etching of Al-atoms from the structure, leaving only two-dimensional sheets of Ti_3C_2 left. As the A atom had been removed from the MAX phase (giving "MX"), and with two-dimensional morphology reminiscent of graphene, they called the new group of materials "MXenes" (pronounced "maxenes"). Figure 2.5 schematically illustrates the process of etching MAX phases, and the resulting MXenes.

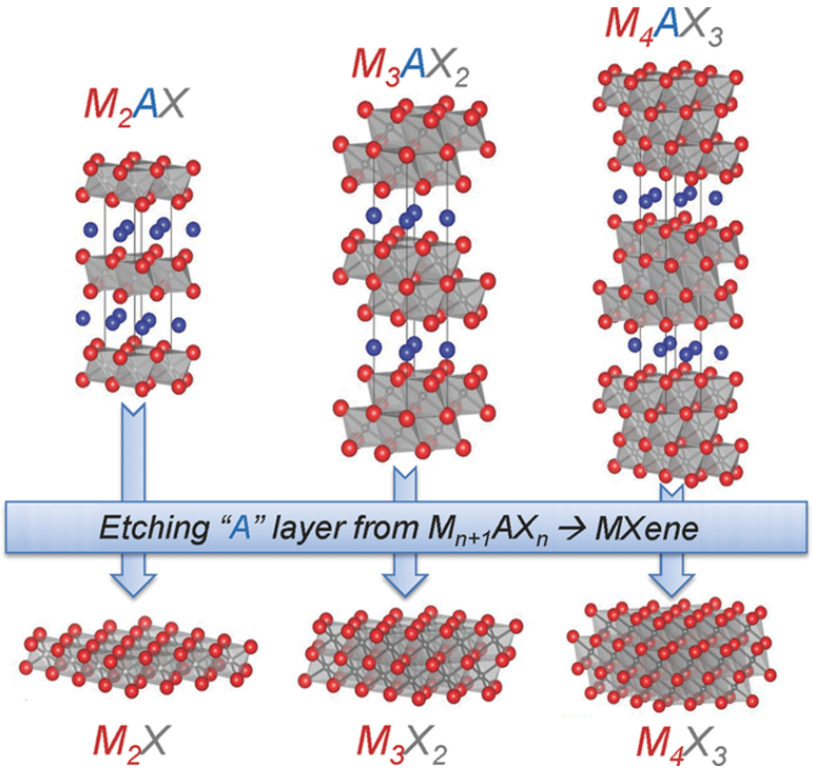

Figure 2.5: Illustration of the structural change upon etching from MAX phase to MXene. Adapted from [97].

To date, more than 70 different MAX phases and more than 20 different MXenes have been successfully synthesized, and the number is rapidly increasing [98, 33]. Until recently, the selective etching of MAX phases has been limited to Al as the A atom, which has been explained by Al having the lowest reduction potential of all the A elements [99]. However, in February 2018 A. Mohamed et al. managed to selectively etch Si from Ti_3SiC_2, opening up for new and possibly cheaper synthesis routes of MXene materials [100].

2.3.2 MXene synthesis

As mentioned, MXenes have so far been synthesized by wet-etching of a MAX phase powder in hydrofluoric acid (HF) or HF-forming etchants [98, 21, 101]. This chemical etching process results in functionalized surfaces with -O, -F or -OH termination groups bound to the M element, which are generally denoted as T_x in the formula for MXenes ($M_{n+1}X_nT_x$). However, for the sake of simplicity the $M_{n+1}X_n$ notation is used to described the MXenes in this report. When not mentioned specifically, the presence of the termination groups on the MXene surfaces is implied.

The general chemical reactions during etching of the MAX phase have been proposed to be:

$$M_{n+1}AlX_n + 3HF \rightarrow M_{n+1}X_n + AlF_3 + 1.5H_2, \tag{2.13}$$

$$M_{n+1}X_n + 2H_2O \rightarrow M_{n+1}X_n(OH)_2 + H_2, \tag{2.14}$$

$$M_{n+1}X_n + H_2O \rightarrow M_{n+1}X_nO + H_2. \tag{2.15}$$

$$M_{n+1}X_n + 2HF \rightarrow M_{n+1}X_nF_2 + H_2, \tag{2.16}$$

where Equation (2.13) shows the removal of the A atom, while Equations (2.14), (2.15) and (2.16) describe the formation of the termination groups on the MXene surfaces [20]. Controlling the termination groups of the MXene material is of great importance for most applications, as they have been modelled and experimentally verified to strongly influence the properties of the MXenes [102, 103, 104, 105].

Critical etching parameters for MXene synthesis are the HF concentration, the temperature and the duration of the etching. Despite the structural similarities between the different types of MAX phases, the optimal etching conditions vary strongly[98]. One of the reasons for this is the different bond energies between the transition metal and the Al. For example, it has been found that Nb_2AlC requires longer etching times than Ti_2AlC [34, 106], where the Nb-Al and Ti-Al bond energies in Nb_2AlC and Ti_2AlC have been estimated to be 1.21 eV and 0.98 eV, respectively [107].

Increasing the HF concentration usually reduces the etching time needed, but may not be ideal for all MAX phases. This is because of the difference in stability for the different MXenes, where the value of n for a given $M_{n+1}AX_n$ phase plays an important role. For example, while the Ti_3AlC_2 MAX phase may well be etched using a 50% solution of HF, the

same concentration results in the complete dissolution of Ti_2AlC [106]. Generally, the higher the n, the more stable the MXene.

Another parameter that influences the required etching conditions for complete exfoliation of the Al layer is the particle size of the immersed powder [34]. The particle size and morphology determines the distance that the HF molecules need to diffuse in order to reach the innermost Al atoms, and therefore also the diffusion time that is needed. As the HF molecules diffuse in between the MXene layers, it is the lateral particle sizes that determines the diffusion path. Considering that the particle sizes may vary significantly, it is difficult to achieve equal etching of all particles. Having a narrow particle size distribution is therefore of great importance when trying to prevent some of the particles to be overetched, while at the same time ensure the complete removal of Al atoms from the bigger particles. In order to compare the etching parameters, average values or mesh values for the particle sizes are usually applied. Unfortunately, no general relation between etching time and particle sizes exists, as of today.

After the etching of the MAX phase, the particle sizes usually remain similar. Even though the Al atoms are etched out, the Van der Waals forces between the two-dimensional flakes are still strong enough to hold the two-dimensional flakes together. In order to separate these flakes, and obtain delaminated MXene flakes (denoted d-$M_{n+1}X_n$) one would first need to preintercalate the structure with cations[108], or some organic molecules such as TBAOH [109]. These molecules help to swell the MXene structure, which reduces the attractive van der Waals forces between the flakes. If the attractive forces are weakened enough, then sonication or even hand shaking has been shown to delaminate multilayered ($ml-$) MXenes into single- (sl-) and few layered (fl-) MXenes [23]. The process is schematically illustrated in Figure 2.6. Here again, the conditions that are needed for successful delamination of MXenes vary substantially for different MXenes.

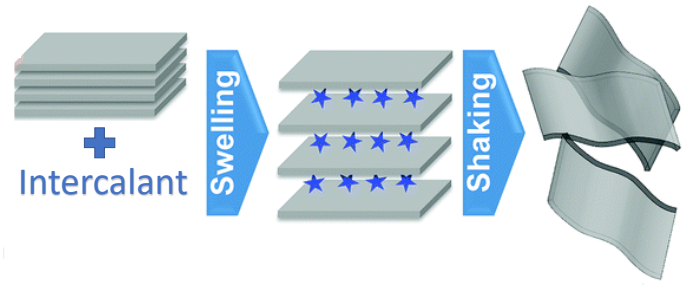

Figure 2.6: The process of MXene delamination, illustrating how the insertion of an intercalant helps to swell the structure, which allows for the separation of single layered MXene. Adapted from [23].

2.3.3 MXene intercalation properties

Owing to their outstanding properties, including high melting point, excellent oxidation resistance, hardness, compositional variability, hydrophilic nature, high electrical and thermal conductivity, high surface area, and ability to host a broad range of intercalants, MXene materials have been developed as promising electrode materials [110]. By controlling the interlayer distance between the MXene layers, together with the termination groups, the ion hosting capabilities of the MXene material can be finely modified [111, 102, 98]. As already mentioned, the interlayer distance can be adjusted by the preintercalation of various molecules. Additionally, due to the hydrophilic nature of MXenes, water molecules have also been found to easily intercalate into the structure, being one of the main sources for variations in interlayer distances [34, 112]. The formation of termination groups is generally related to the etching conditions utilized, where a higher HF concentration usually results in more F- and OH-terminations being formed [102]. To change the termination groups, annealing [113], suspension into alkaline solutions (KOH) [114, 102], and delamination [23], have all shown to reduce the amount of F-terminations, in favour of OH- and O-terminations.

To the author's knowledge, there has been no experimental investigations on the intercalation sites of Mg-ions into any MXene structures, although theoretical predictions have been reported [32]. Figure 2.7 shows the predicted sites from density functional theory (DFT) calculations, indicating an addition of 2 Mg-ions per unit of V_2C. Calculations on the preferred intercalation pathways of Li-ions have also been completed [115], showing that the different termination groups greatly affect the kinetics of the cation diffusion into the host structure. Termination groups have also been calculated to have a great impact on the theoretical capacity of V_2C, where O-terminated surfaces is expected to result in the highest specific capacity, of all termination groups mentioned here [32].

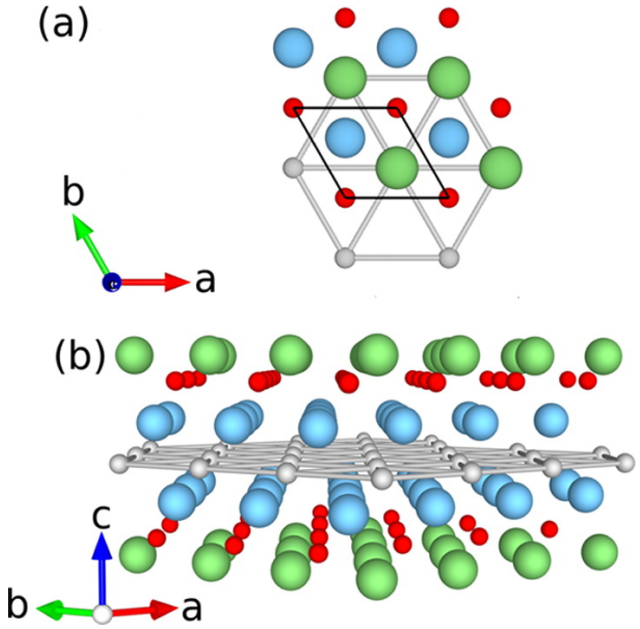

Figure 2.7: Illustration of the theoretically predicted cation intercalation sites on the V_2C structure: (a) view down the c-axis and (b) side view. Spheres represent: intercalant (green), functional group (red), vanadium (blue) and carbon (grey). In the top view, the 1x1 unit cell is outlined in black. Reused from [32].

2.3.4 V_2C MXene

V_2C belongs to the thinnest group of MXenes, consisting of only two layers of transition metal atoms per MXene flake. In order to understand the structure of the V_2C MXene, it is important to recognize the structure of its MAX phase precursor. V_2AlC is a layered hexagonal 211-phase (referring to the stoichiometry of V:Al:C), belonging to the space group $P6_3/mmc$, with lattice parameters of a = 2.9107 Å, and c = 13.101 Å [116]. The unit cell of the structure is presented in Figure 2.8, and consists of the vanadium atoms in a hexagonal closest packing arrangement with interstitial carbon atoms in the octahedral sites between the vanadium layers.

After exfoliation of the aluminum layer, the two-dimensional V_2C retain the layered structure of V_2AlC. The main difference is the expansion of the c-lattice vector, which comes from an increase in the interlayer distance. Due to the ordered structure of the MXene material, XRD measurements are one of the most important characterization techniques used to verify the V_2C formation. This can generally be observed by a downward shift of the peaks related to planes in the c-axis (usually the (002)-peak), which comes from the increased spacing between the V_2C-flakes.

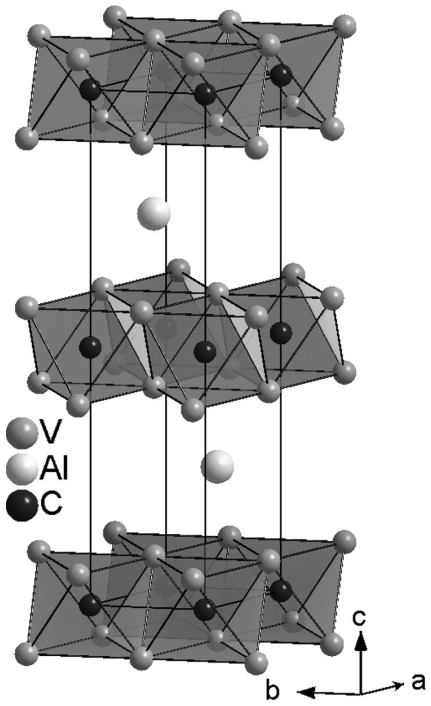

Figure 2.8: Unit cell of the V_2AlC structure. Reused with permission from [116].

The properties of V_2C MXene are generally affected by the same parameters as other MXenes, with the change of interlayer distances and termination groups. Additionally, as the bond energy between V-Al in V_2AlC is higher (1.09 eV) than that between Ti-Al in Ti_2AlC (0.98) [107], this MAX phase generally requires higher concentrations of HF in order to successfully exfoliate the Al-layer. Most reports to date have utilized HF concentrations as high as 50%, and etching times of up to 96 h [37, 34, 36, 23].

Chapter 3

Experimental

3.1 Overview

The experimental work of this project has consisted of V_2C MXene synthesis from in-house synthesized V_2AlC MAX phase, which in turn has been used to create coin cell cathodes for rechargeable magnesium batteries. The MXene and MAX phase synthesis processes are heavily based on previously reported methods [37, 34, 36, 23]. However, in order to obtain phase purity, some important information was lacking. Therefore, the procedure itself had to be fine tuned and the missing parameters had to be optimized.

During this period, a total of 5 batches of V_2AlC have been synthesized, 4 different HF etching processes have been completed, 1 attempt of preintercalating TBAOH followed by 2 attempts of delaminating V_2C has been done, 4 different V_2C-containing slurries have been prepared, and in total 32 coin cell batteries have been assembled, using 3 different electrolytes. Figure 3.1 illustrates the overview over which processes that are connected, where the numbering of the batches and the etching processes is done chronologically. These numbers will be used to address the different processes throughout this chapter.

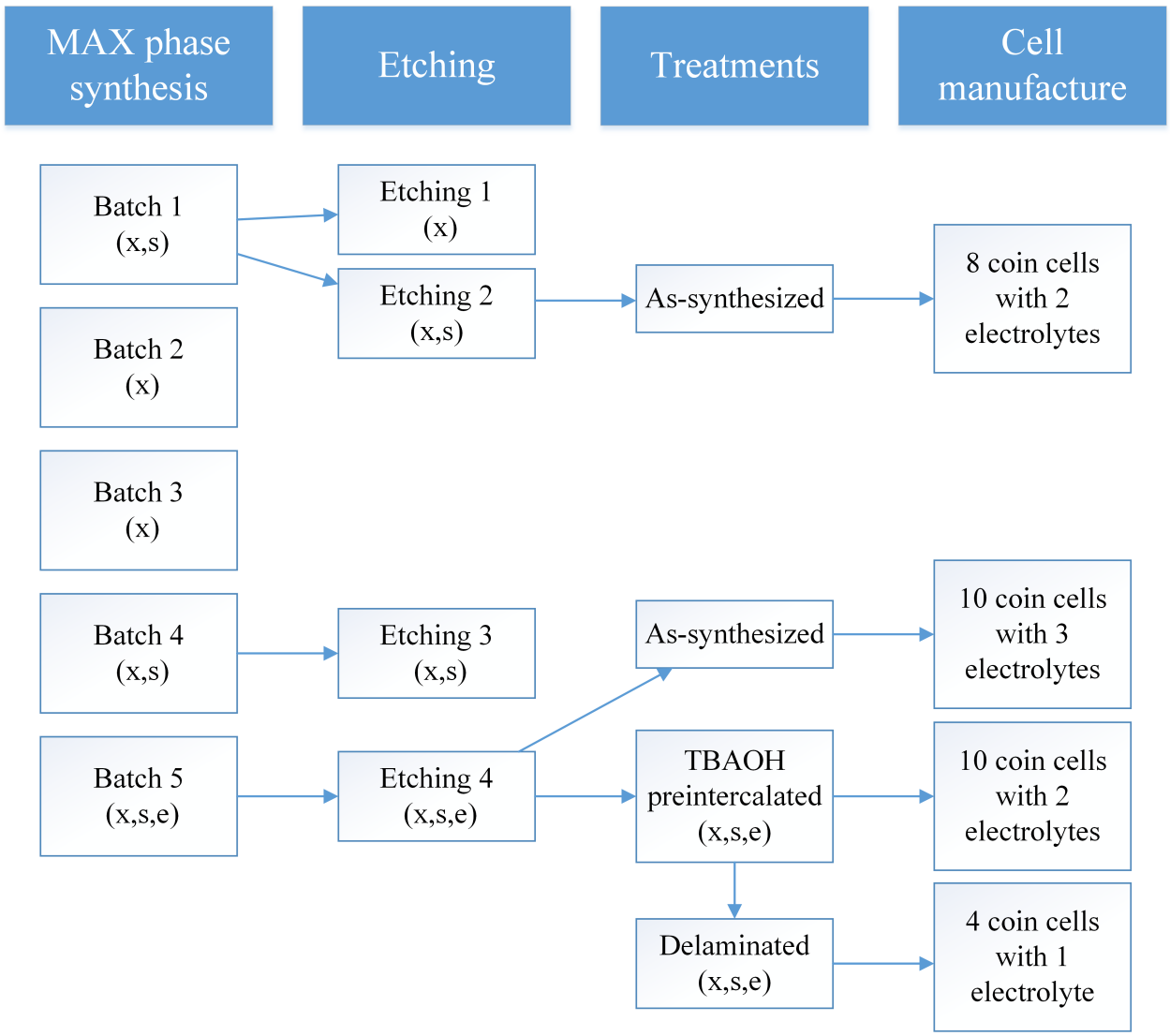

Figure 3.1: A structural overview of the experimental work that has been completed. The letters x, s and e represent the characterization methods that have been utilized on the products of the given step, where x, s and e represent XRD, SEM and EDX measurements, respectively.

3.2 MXene synthesis

3.2.1 MAX phase synthesis

The MAX phase synthesis process consists mainly of five steps. These steps are shown in Figure 3.2, where the order of the different steps is illustrated.

Figure 3.2: Schematic of the processes that are a part of the MAX phase synthesis.

In order to synthesize the desired V_2AlC MAX phase, vanadium powder (99.5%, 325 mesh, Sigma-Aldrich®), aluminum powder (99.5%, 325 mesh, Alfa Aesar) and graphite powder (99.5%, 400 mesh, TIMCAL TIMREX) were mixed in a 125 ml milling bottle with the molar ratio of 2:1.3:1. To prevent oxidation of the aluminum and vanadium powders, they were stored and weighed inside an argon filled glovebox (MBraun, $O_2 < 0.1$ ppm, $H_2O < 0.1$ ppm). After adding the metal powders into the milling bottle, the bottle was taken out of the glovebox, before a sufficient amount of yttria stabilized zirconia milling balls to fill 2/3 of the bottle was added (∼300 g). Immediately afterwards, isopropanol was added (just enough to cover the milling balls) in order to minimize air exposure. Then, the graphite powder was weighed and added to the mixture, before the bottle was placed on a roll mill (U.S. Stoneware Long Roll Jar Mill) and milled at 205 rpm for approximately 18 hours. This step was done to increase the homogeneity of the powder mixture.

After the wet milling process, the isopropanol was evaporated by different approaches. General for all procedures was that the mixture was poured into a beaker, filtering out the milling balls using a 4 mm pore sized plastic sieve. To increase the yield, the balls and the plastic bottle were washed with more isopropanol. Then, the isopropanol was evaporated, leaving a dry mixture of the different powders. For the first batch, this was done by leaving the beaker on a hot plate (40 °C) for 3-4 h, before the dry powder mixture was scooped over to an alumina crucible. For the second batch, it was done by removing most of the supernatant using a plastic pipette, before the remaining mixture was dried directly in the crucible at room temperature. The remaining three batches utilized a rotavapor (Büchi® R 210) for the evaporation, where the beaker was rotated at 50 °C under a pressure of 137 mbar.

Before sintering of the powder mixtures, the last three batches were pressed into cylindrical 1 g pellets with a diameter of 10 mm. This was done by initially applying a pressure of 25 MPa for 10 s, before releasing the pressure for another 10 s. This was done to let some of the air out before further pressing. Thereafter, the final pressure of 50 MPa was held for 20 s in order to form around 6 mm tall pellets that were put into the crucible. The uniaxial pressing of the pellets was done manually using a toggle press (Mäder VK 2500-40). To test the difference between sintering of powders and pellets, batch three was divided into two parts, where only one of them was pressed into pellets. Table 3.1 shows a summary of how the different batches were prepared for sintering, and the images in Figure 3.3 illustrates how the different mixtures were sintered.

To form the V_2AlC MAX phase, the dried powder was then sintered. The alumina crucible, containing the powder mixture, was inserted into a sealed tube furnace (Entech ETF 17) before supplying a continuous flow of argon gas through the sample chamber. To prevent the presence of oxygen at higher temperatures, the sintering program was started with a 4 h dwelling step at room temperature for the argon to flush out the air inside the tube. The argon flow was determined by the number of bubbles per second in a borosilicate glass bubble counter (DURAN®), and was adjusted to be around 2-3 bubbles per second. After the dwelling step, a heating rate of $5\,^{\circ}\mathrm{C\,min^{-1}}$ was used until the target temperature of 1500 °C was reached. This temperature was held for 4 h, before the furnace was cooled to room temperature using a cooling rate of $5\,^{\circ}\mathrm{C\,min^{-1}}$.

After sintering, the sintered powder/pellets were downsized using a steel mortar, prior to XRD measurements. A steel mortar was used to prevent damaging of agate, due to the hardness of the V_2AlC particles. After XRD verification, the V_2AlC-containing samples were further downsized down either by dry planetary ball milling at 600 rpm (Retsch PM 100), or by simply continued grinding with the metal mortar. To ensure a certain particle size distribution prior to the etching, the powders were sieved through a 325 mesh sieve, in order to acquire particle sizes smaller than 44 µm. Table 3.3 lists which downsizing method was used for the different powders. Until the continued synthesis of V_2C, the powders were stored in sample bottles under ambient conditions. EDX measurements were done to characterize the elemental contents of the powders, and SEM was used to investigate the general morphology of the powders, as well as to give an approximate particle size distribution.

Table 3.1: A summary of the different evaporation methods utilized for the different MAX phase batches, as well as which of the powder mixtures that were pressed into pellets. In addition, it also lists how the powders were downsized prior to the following etching step. 'RT' and 'PM' are here used as abbreviations for room temperature and planetary milling, respectively.

Batch nr.	Drying procedure	Form	Downsized
1	In beaker at 40 °C	Powder	3 × 3 h PM
2	In crucible at RT	Powder	-
3	Rotavapor	Powder + Pellet	-
4	Rotavapor	Pellet	3 × 3 h PM
5	Rotavapor	Pellet	Mortared ∼ 30 m

(a)

(b)

(c)

Figure 3.3: Pictures of the alumina crucibles before the first three batches were sintered, illustrating the different ways that the powder was prepared for sintering. Image (a) shows the scooped powder of batch 1 after being air dried in a beaker, (b) presents how the remaining isopropanol of batch 2 was evaporated directly in the crucible (at the beginning of the evaporation), and (c) represents the rotavapored powder mixture of batch 3 as both powder and pellets. The remaining two batches were sintered like the pellets in image (c).

3.2.2 Etching of MAX phase

In order to selectively etch out the aluminum atoms from the synthesized V_2AlC MAX phase, concentrated hydrofluoric acid (HF) was used. It was done by measuring a desired amount of HF solution with a specific concentration before pouring it into a plastic beaker containing a teflon coated magnet. A certain amount of V_2AlC powder was then immersed into the solution over a 30 min period, in order to limit the concentration of the formed hydrogen gas and to prevent excess heating of the mixture, which might lead to oxidation of V_2C. Thereafter, the beaker was covered with parafilm, to prevent spilling and/or evaporation of HF during the etching period. To prevent a high concentration of hydrogen gas being trapped, a small opening in the parafilm was made. The dispersion was then left stirring for a given amount of time. Table 3.2 lists the different parameters that were used for the different etching processes.

Table 3.2: Etching parameters for the four different etching processes of the synthesized MAX phases, where all of them were completed at room temperature.

Etching nr.	1	2	3	4
Etched MAX phase batch	1	1	4	5
Amount of etched powder	0.5 g	0.5 g	4 g	3.5 g
HF concentration (wt. %)	10	48	48	48
Amount of HF solution	15 ml	10 ml	30 ml	30 ml
Etching time	48 h	96 h	96 h	96 h

After the etching process was ended, the powder was washed with deionized water to remove the HF. This was done by carefully pouring the dispersion into a 125 ml plastic centrifuge bottle, and using deionized water to get all of the powder out of the beaker. Then, the centrifuge bottle was almost completely filled with water, before the dispersion was centrifuged (VWR Mega Star 600) at 4350 rpm (corresponding to a relative centrifugal force (RCF) of $\sim$1800 $\times$ g) for 7 min. To prevent unnecessary shaking of the mixture, a soft acceleration and deceleration program was used additionally to the 7 min centrifugation time. The acceleration time was around 30 s, and the deceleration time was around 190 s. Thereafter, the supernatant was decanted and discarded before the remaining powder mixture was diluted with water and centrifuged again. This washing process, consisting of the centrifugation, the decantation and the dilution of the mixture, was repeated until he pH was measured to be above 5. Normally, around 5 centrifugations were needed to achieve this pH.

The dispersion containing the washed V_2C powder was vacuum filtered using either a 0.22 µm or 0.45 µm pore sized filter (GVWP09050 Durapore® Membrane Filters) to remove most of

the water. The filter paper, with the adsorbed V_2C powder, was then dried under vacuum in a vacuum oven (Binder VD 23) at 120 °C for 24 h, in order to remove all of the water from the powder. Following this, the remaining powder was scraped off the filter paper and stored in a sample bottle. To prevent unwanted oxidation, the powder was stored under vacuum in a desiccator (Scienceware® Lab Companion™). The as-synthesized V_2C was characterized using XRD, EDX and SEM, before being used to fabricate cathodes for coin cell batteries. Additionally, some of the V_2C was treated with tetrabutylammonium bromide hydroxide (TBAOH) and delaminated, as described in the next sections.

3.2.3 Preintercalation of tetrabutylammonium bromide hydroxide

With the goal of increasing the interlayer distance and alter the termination groups of the exfoliated V_2C, the organic base TBAOH was preintercalated through a simple wet mixing approach. This was done by dividing 1.4 g of the V_2C powder into two separate glass beakers, each containing 20 ml of a 20 wt.% aqueous TBAOH solution. This solution had been prepared by diluting 20 ml of a 40 wt.% TBAOH solution (Sigma-Aldrich®) with 20 ml of deionized water. The dispersions were then carefully stirred at 100 rpm overnight (∼14 h) at room temperature, in order to prevent unintended delamination of the multilayered ($ml-$) V_2C.

To remove residual TBAOH, the two mixtures were centrifuged in 50 ml centrifuge tubes (VWR) for 10 min with a speed of 5500 rpm (RCF: 3855 × g). In order to prevent unwanted shaking of the containers, an additional 2 min long acceleration time and 3 min long deceleration time were used. After the centrifugation, the supernatant was decanted and discarded. Then, the sedimented powder was washed by several iterations of diluting the dispersions, centrifuging them and discarding the decanted supernatants. Deionized water was used to dilute the dispersions the first two times, before absolute ethanol (VWR) was used for the last two times.

After washing the TBAOH-treated powder, the sedimented powder was vacuum filtered before drying under vacuum at 120 °C for 24 h. Here, a 0.22 µm pore sized filter was utilized. Then, the powder was scraped off the filter paper and stored in a vacuum desiccator until further use.

As the TBAOH-treated V_2C showed significant peaks of potassium in the EDX spectra, the TBAOH solution was inspected by EDX as well. This was done by drying one drop of the TBAOH solution directly on copper tape on the SEM sample holder. The dried particles

were inspected by EDX, to look for potassium.

3.2.4 Delamination of MXene

To delaminate single- and few-layered flakes from the *ml*-V_2C particles, approximately 0.7 g of the TBAOH-treated V_2C was added to a glass beaker containing 100 ml of deionized water. The dispersion was then sonicated in an ice-cooled ultrasonic bath (Branson B1510MTH) for 1 h. To prevent oxidation of the flakes, nitrogen gas was bubbled through the dispersion during the sonication, with a flow rate of 0.2 (controlled with a Swagelok flow rate measurement tool).

After sonication, the dispersion was divided into two 50 ml centrifuge tubes using a plastic pipette. Thereafter, the dispersions were centrifuged for 30 min at a speed of 3500 rpm (RCF: 1561 × g) in a centrifuge (Eppendorf 5810 R). The black supernatant was then decanted, vacuum filtered and dried under vacuum at 120 °C for 24 h. The remaining sedimented powder was diluted with deionized water once again, before being hand shaken for 5 min. Similar to the sonicated dispersion, this mixture was also centrifuged for 30 min at a speed of 3500 rpm (RCF: 1561 × g), before the decanted supernatant was vacuum filtered and dried. All powders were stored in sample bottles in a vacuum desiccator, after being inspected by powder X-ray diffraction and characterized by SEM and EDX. Figure 3.4 shows the black supernatants that were obtained after both delamination attempts.

3.3 Characterization

The different characterization techniques used on the different powders obtained from the MXene synthesis comprise XRD, SEM and EDX. Figure 3.1 shows which of the techniques that have been utilized for the characterization of the different powders.

The SEM images of the powder particles were taken with a Carl Zeiss AG - ULTRA 55 SEM, using an aperture size of 30 µm, an acceleration voltage of 10 kV, a working distance of 8 mm, and a scan time of 20.2 s per image. The SEM was equipped with an X-ray detector (XFlash® 4010), which was used for the EDX measurements. To achieve optimal signal output for these measurements, the parameters were changed to an aperture size of 120 µm, an acceleration voltage of 20 kV and a working distance of 10 mm. To further increase the signal output, a high current was also used for the EDX measurements.

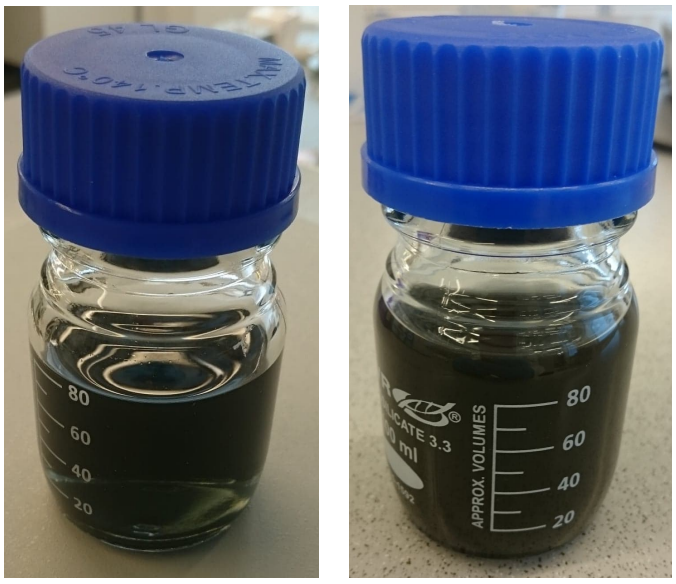

(a) (b)

Figure 3.4: Pictures of the black supernatants that were obtained after the two delamination attempts, where images (a) and (b) represent the sonicated and hand shaken dispersions, respectively.

In order to obtain representative EDX data, measurements from 5 different points, obtained from 5 different particles, were used to calculate an average elemental composition of the inspected material. The data was analyzed with the ESPRIT analysis software. The SEM image distance measurements were performed with the use of ImageJ.

The XRD measurements were performed on a Bruker D8 Focus Diffractometer using a Cu Kα radiation source, and a divergence slit size of 0.2 mm in order to reduce the background noise at lower 2Θ angles. The powder samples were prepared by filling Si cavity sample holders with a diameter of 15 mm, before gently pressing the powder with a metal spatula to obtain a flat surface. Analysis of the obtained XRD plots was performed with the DIFFRAC.EVA software from Bruker, with the PDF 2018+ database. As the V_2C MXene is a recently discovered material, it is not in the current PDF 2018+ database. The assignment of V_2C MXene peaks were done on the basis of reported XRD peaks in the literature.

When scanning the powder samples, two different XRD scan programs have been utilized. One of them was done from a 2Θ value of 5° to 75° separated into 4898 steps with a measuring time of 0.68 s per step. This was the overview scan which enabled the analysis of most of the V_2AlC- and V_2C-related peaks, as well as possible impurities. The second scan measured only lower 2Θ-values, focusing on the (0002) peaks related to V_2C and V_2AlC. This scan measured 2Θ from 3.5° to 18° in 2032 steps with a measuring time of 1 s per step.

3.4 Cell manufacture

3.4.1 Cathode preparation

In order to test the synthesized V_2C as cathode material, first a V_2C-containing slurry was prepared. The slurry consisted of 15 mg (10%) polyvinylidene fluoride (PVDF) binder (Kynar F2801), 15 mg (10%) carbon black (Imerys C-nergy super C65) and 120 mg (80%) V_2C and approximately 1 ml of 98% 1-Ethyl-2-pyrrolidone (NEP) (Sigma-Aldrich®). It was made by adding 40 droplets of NEP into a 5 ml steel shaker jar using a plastic pipette, before adding the weighed PVDF powder. The mixture was then shaken with a 7 mm steel ball in a shaker mill (Retsch MM 400) at 25 Hz for 20 min. This step was completed to ensure that the PVDF dissolved in the NEP and formed a homogeneous solution, before adding the carbon black and V_2C powders. Lastly, the mixture was shaken for another 30 min to finish the slurry preparation.

In order to test the contribution of carbon black in the cathodes, an extra slurry consisting of 90% carbon black and 10% PVDF was prepared by the co-supervisor of this thesis.

The cathodes were made by drop casting the slurry onto circular discs of carbon paper current collectors (Spectracarb 2050A-0550), where the discs had been pre-cut with a diameter of 16 mm, using an electrode cutter (Hohsen Corp.). Then the cathodes were left in a fume hood to dry for a minimum of 15 h, before they were further dried under vacuum at 120 °C for 3 h. After drying the cathodes, they were stored in an argon filled glovebox.

Due to different viscosities and a variation of drop sizes, the drop casting procedure resulted in some variations of cathode loadings. In order to know the amount of active material (V_2C) in each cathode, all cathodes were weighed both before the slurry was casted onto them and after the slurry was dried.

3.4.2 Mg-disc and separator preparation

Magnesium anode discs were prepared by using a 30 µm grain sized SiC sandpaper (Struers) to polish the oxidized surface of a magnesium metal foil (Solution Materials). Then, 12 mm diametered discs were punched out using a puncher cutter (Boehm France), before they were washed in absolute ethanol. To limit the oxidation of the surfaces, the discs were then stored in absolute ethanol before they were dried under vacuum at 50 °C for 1 h. Immediately after

being dried, the discs were introduced into an argon filled glovebox.

The separators (Whatman™GF/A glass microfiber filters) were similarly cut using a 17 mm punching tool. Prior to being introduced to the glovebox, they were also dried under vacuum at 50 °C for 1 h .

3.4.3 Electrolyte mixing

Three different electrolytes were used: 0.4M all phenyl complex solved in tetrahydrofuran (APC:THF), 0.4M LiCl solved in the APC:THF electrolyte (APC/LiCl:THF) and 0.5M magnesium bis(trifluoromethane)sulfonimide with magnesium chloride solved in 1,2-dimethoxyethane ($Mg(TFSI)_2/MgCl_2$:DME). The APC:THF and $Mg(TFSI)_2/MgCl_2$:DME electrolytes were mixed by the co-supervisor Henning Kaland, while the APC/LiCl:THF electrolyte was made by the author. All of the electrolytes were mixed in 20 ml glass bottles inside the glovebox.

The APC:THF electrolyte was prepared by adding 1.066 g of $AlCl_3$ (99.999%, Sigma-Aldrich®) to a glass bottle, before 12 ml of THF (Sigma-Aldrich®) was carefully added over the course of 20 min due to a very exothermic reaction taking place. After stirring until the $AlCl_3$ was completely dissolved, 8 ml of 2M phenylmagnesium chloride in THF (Sigma-Aldrich®) was dropwise added over a few minutes. The mixture was then stirred at 400 rpm overnight to ensure complete dissolution of the salts, and to let the electrolyte species reach equilibrium.

The APC/LiCl:THF electrolyte was prepared by weighing 50.87 mg of LiCl powder (99.7%, VWR) in a new bottle, before adding 3 ml of the APC:THF electrolyte. To completely dissolve the LiCl, the mixture was stirred at medium speed and at *ca.* 40 °C for 1 h.

Mixing of the $Mg(TFSI)_2/MgCl_2$:DME electrolyte was done similarly to the previous ones, where 0.8769 g of $Mg(TFSI)_2$ powder (Sigma-Aldrich®, [1]) and 0.1428 g of $MgCl_2$ powder (≥98%, Sigma-Aldrich®) were added to a glass bottle, before 3 ml of DME (Alfa Aesar) was added. The mixture was then stirred overnight.

The three electrolytes described above were used to assemble batteries. However, the batteries assembled with the $Mg(TFSI)_2/MgCl_2$:DME electrolyte showed abnormal cycling behavior. To verify the electrolytes itself, cyclic voltammetry (CV) was carried out to reveal reversible

[1] Upon request, a water content of 7.4% (Karl Fischer method) was supplied by the manufacturer.

Mg deposition and stripping versus the graphite paper current collector. The CV scan was done from -0.9 to 2.8 V, with a scan rate of 1 mV/s, and were performed by co-supervisor Henning Kaland.

During this project, $MgCl_2$ powder was also attempted dissolved in APC:THF in a concentration of 0.2M. However, as the powder did not dissolve, this electrolyte was not utilized in any batteries.

3.4.4 Coin cell assembly

The assembly of coin cell batteries was carried out under an inert atmosphere in a glovebox. Figure 3.5 shows a schematic of the coin cell constituents. The battery parts that have not been specifically described in the previous sections consist of coin cell bottoms and tops, 0.3 mm spacers and gaskets (Hohsen Corp.). Approximately 75 µl of electrolyte was added before and after the separator was inserted, in order to completely wet the separator.

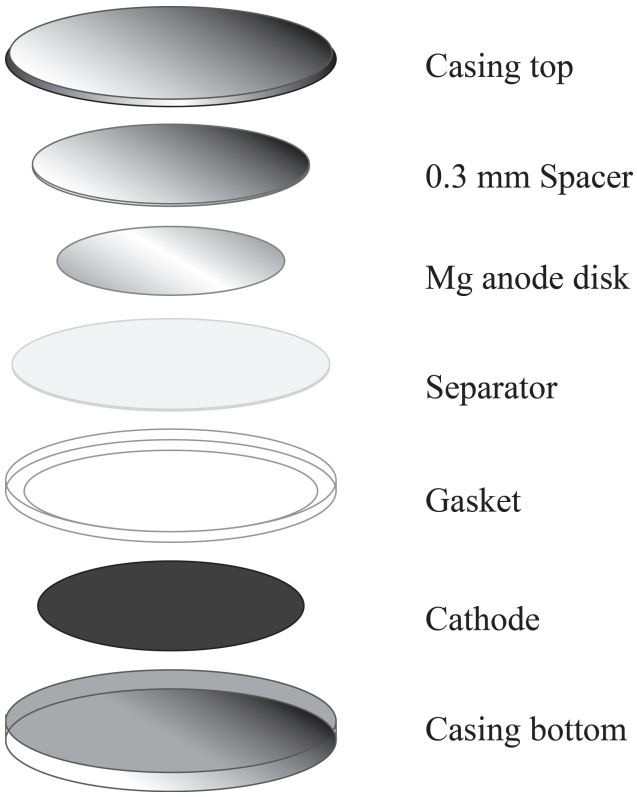

Figure 3.5: Illustration of the order of the different components of the coin cell.

After all the parts were assembled and aligned, the coin cells were crimped using an automatic crimping tool (Hohsen Corp.). Then, they were taken out and cleaned with ethanol to remove

electrolyte residues. To let the electrolytes wet and fill all the pores, no cycling program was started before a minimum of 12 h after the coin cells were assembled.

3.5 Electrochemical characterization

The galvanostatic cycling of the batteries was completed using three different cyclers (LANHE CT2001A, MACCOR 4200 and Bio-Logic BCS-805). The testing programs generally consisted of 100 cycles of discharging to 0.2 V and charging to 2.1 V. As the main goal was to look for signs of Mg-intercalation, a low C-rate of 0.02 was used. By utilizing a theoretical specific capacity of 470 $\mathrm{mA\,h\,g^{-1}}$, this C-rate represents a current of approximately 9.4 $\mathrm{mA\,g^{-1}}$.

The cycling was carried out in a temperature-controlled room set at 20 °C. Some batteries were also tested in a heated chamber at 50 °C, to see if the ion diffusion of the Mg-ions was improved. The rest were cycled in a room with a relatively stable temperature of 20 °C. Additionally, different C-rates were used on some of the batteries, in order to test their rate capabilities. These increased C-rates were 0.1 C, 0.2 C and 0.5 C.

Noteworthy, some of the batteries were unable to reach the upper cut-off voltage of 2.1 when being cycled at 50 °C. For this reason, some of the batteries have been cycled with reduced upper cut-off voltages of either 1.7 V or 1.9 V.

Chapter 4

Results

4.1 Overview

The results are divided into two main sections, being the synthesis of the active material and the electrochemical characterization of the assembled cells. The synthesis results will be presented first, and consist of XRD plots, SEM images and EDX data from the different batches that have been synthesized, together with images that illustrate notable details of the process. The second part consists of the galvanostatic cycling results from a representative selection of the batteries that have been tested.

4.2 V_2C MXene synthesis

4.2.1 V_2AlC MAX phase synthesis

Synthesis yield

Table 4.1 shows the mass changes of the five different MAX phases batches, and the resulting yield.

Table 4.1: Mass changes and yield for the five different MAX phase batches, where the end mass here represents the obtained powder after the sintering process. Noteworthy, the 2nd batch exhibited an increase of mass during the synthesis.

Batch nr.	Start mass (g)	End mass (g)	Mass change (g)	Yield (%)
1	2.00	1.46	-0.54	73
2	5.00	5.06	+0.06	101
3	3.00	2.47	-0.53	82
4	6.00	5.53	-0.47	92
5	4.50	3.97	-0.53	88

Crystallinity and phase purity

The XRD measurements of the five MAX phase batches are illustrated in Figure 4.1. It shows the $5 \leq 2\Theta \leq 75$ plots of the different batches summarized in Table 3.1, where Batch 2, 3 and 4 are represented by two different plots each. Batch 2 resulted in the formation of two separate layers after the sintering process, with a grey bottom layer and a brown layer on top, where the different layers were scanned separately. The plots from Batch 3 represent the sintered powder and pellets, respectively, and the plots for Batch 4 describes the powder before and after being planetary milled. To simplify the reading of the results, the changes between the different plots are presented by abbreviations explaining the batch number, evaporation method, whether or not the powder was pressed into pellets, and how the powder had been downsized. These abbreviations are: air dried (AIR), air dried in crucible (AIRCR), bottom layer (L1) and top layer (L2) of batch 2, dried in rotavapor (ROTA), pellet pressed (PEL), and planetary milled (MIL). The intensities are presented in logarithmic values, in order to make it easier to spot the different impurity peaks present. On the other hand, the plots have not been normalized to any of the most significant peaks, due to the fact that the orientation of the particles greatly impacts the relation between the intensities of the top peaks, and will be influenced by small differences in the sample preparation.

Table 4.2 lists the impurities found, and in which batches they have been detected. The presence of an impurity has been defined by inspection of visible signal peaks for each of the different structures. These signal peaks are found at 2Θ values of: 7.8° (V_4AlC_3), 31.8° (Al_4C_3), 40.5° (VAl_3), 37.5° (VC), 57.5° (Al_2O_3) and 23.0° (Al_4O_4C).

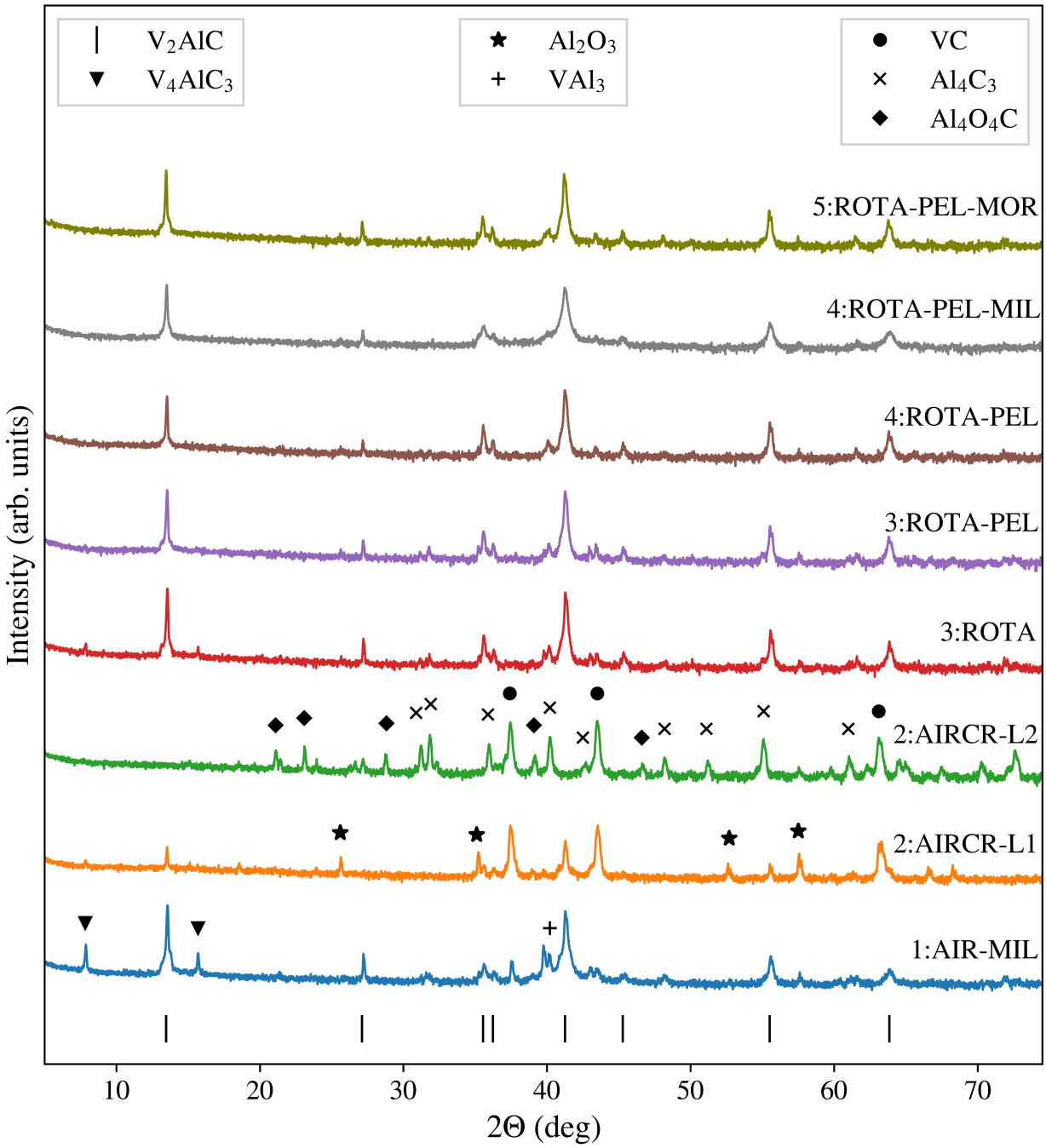

Figure 4.1: Logarithmic plots of the XRD measurements from the five different MAX phase batches that have been synthesized (summarized in Table 3.1). The batches are listed chronologically, and described by abbreviations that explain the differences in synthesis methods. Abbreviations: MAX phase batch (1-5), air dried (AIR), air dried in crucible (AIRCR), bottom (L1) and top (L2) layer of batch 2, dried in rotavapor (ROTA), pellet pressed (PEL), and planetary milled (MIL).

Table 4.2: The impurities showing significant peaks in the XRD plots of the different MAX phase batches.

Batch	Abbreviation	V_4AlC_3	Al_4C_3	VAl_3	VC	Al_2O_3	Al_4O_4C
1	1:AIR-MIL	Yes	Yes	Yes	Yes	Yes	-
2	2:AIRCR-L1	Yes	-	Yes	Yes	Yes	-
2	2:AIRCR-L2	-	Yes	Yes	Yes	-	Yes
3	3:ROTA	Yes	Yes	Yes	Yes	Yes	-
3	3:ROTA-PEL	-	Yes	Yes	Yes	Yes	-
4	4:ROTA-PEL	-	Yes	Yes	Yes	Yes	-
4	4:ROTA-PEL-MIL	-	Yes	Yes	Yes	Yes	-
5	5:ROTA-PEL-MOR	-	Yes	Yes	Yes	Yes	-

Particle size distribution and morphology

Figure 4.2 shows SEM images from the MAX phase batches (1, 4 and 5) that later were etched, after they had been downsized and sieved through a 325 mesh sieve.

Figure 4.2 presents a wide spread in particle sizes, ranging from submicron sizes to the size of the utilized sieve pores (44 µm). The submicron particles tend to agglomerate onto the larger particles, which can be seen for all powders. However, it is apparent that planetary milling (batch 1 and 4) results in more submicron particles, and a generally reduced size of the particles, as compared to the mortared powder (batch 5). Especially the 4th batch contains a lot of agglomerated particles, completely covering most of the larger ones.

The morphology of the larger particles in the different batches are generally similar. The high magnification images (Figure 4.2 b,d,f) reveal the layered structure of the particles. While some show spherical morphologies, there seems to be a tendency towards more disc-like particles, parallel to the layers.

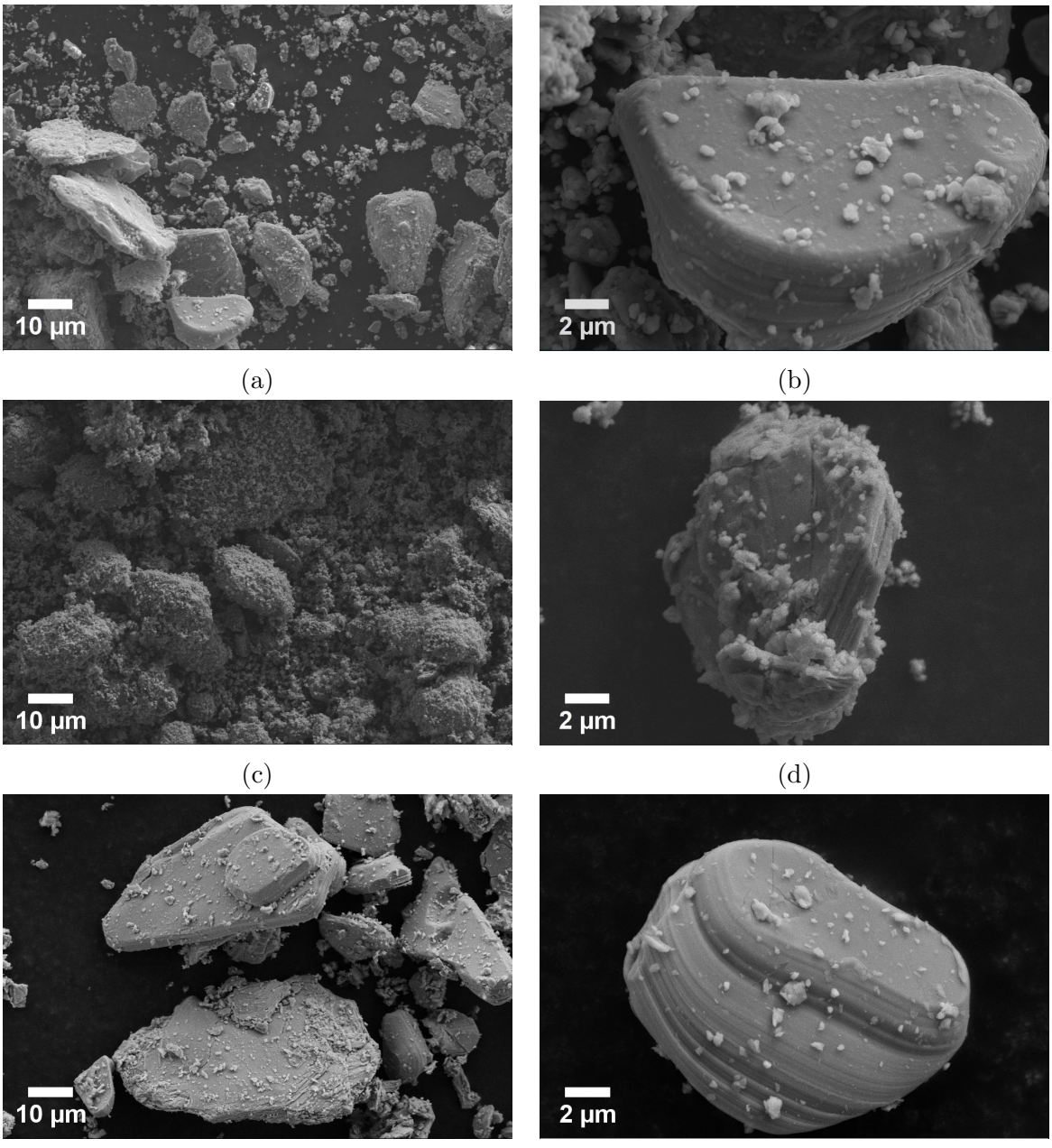

Figure 4.2: SEM images of the particles from the three MAX phase batches that later were etched, where (a-b) illustrate the 1st batch (1:AIR-MIL), (c-d) the 4th batch (4:ROTA-PEL-MIL), and (e-f) the 5th batch (5:ROTA-PEL-MOR).

4.2.2 Etching of V_2AlC MAX phase

Synthesis yield

Table 4.3 lists the mass losses of the four etching processes, together with the resulting yield. Figure A.7 (Appendix A) illustrates the amount of powder that remained on the 0.45 µm and 0.22 µm filter papers after the etched powders had been vacuum filtered, representing one source of mass loss.

Table 4.3: Mass losses during the four etching processes. The batch numbers here refers to the MAX phase batch that was etched.

Etching	Start mass (g)	End mass (g)	Mass change (g)	Yield (%)
Batch 1 - 48 h, 10% HF	0.50	0.31	-0.19	62
Batch 1 - 96 h, 40% HF	0.50	0.07	-0.43	14
Batch 4 - 96 h, 40% HF	4.00	1.77	-2.23	44
Batch 5 - 96 h, 40% HF	3.50	1.81	-1.69	52

Crystallinity and phase purity

Figures 4.3-4.6 illustrate the effects of the etching processes described in Table 3.2. Figures 4.3-4.5 focuses on structural changes and phase purity, showing the etching results of MAX phase batch 1, 4 and 5, respectively. In addition, Figure 4.6 compare the four etching results at lower angels, emphasizing the 2Θ-shift of the (002) peaks related to the formation of V_2C MXene. All of the intensities are presented in logarithmic values.

Figure 4.3 shows the influence of etching time and HF concentration on the structural change of MAX phase batch 1. It shows that 48 h of etching in a 10% HF solution resulted in the removal of the VAl_3 peak at 40.1°, and the introduction of polytetrafluoroethylene with a peak at 18°. Apart from that, no significant changes seem to have occurred. The second etching process on the other hand resulted in a significant reduction of the V_2AlC-related peaks, a complete removal of V_4AlC_3-related peaks, and the introduction of new broader peaks attributed to the formation of V_2C MXene. Some impurities, such as Al_2O_3, and VC still remains after both the processes.

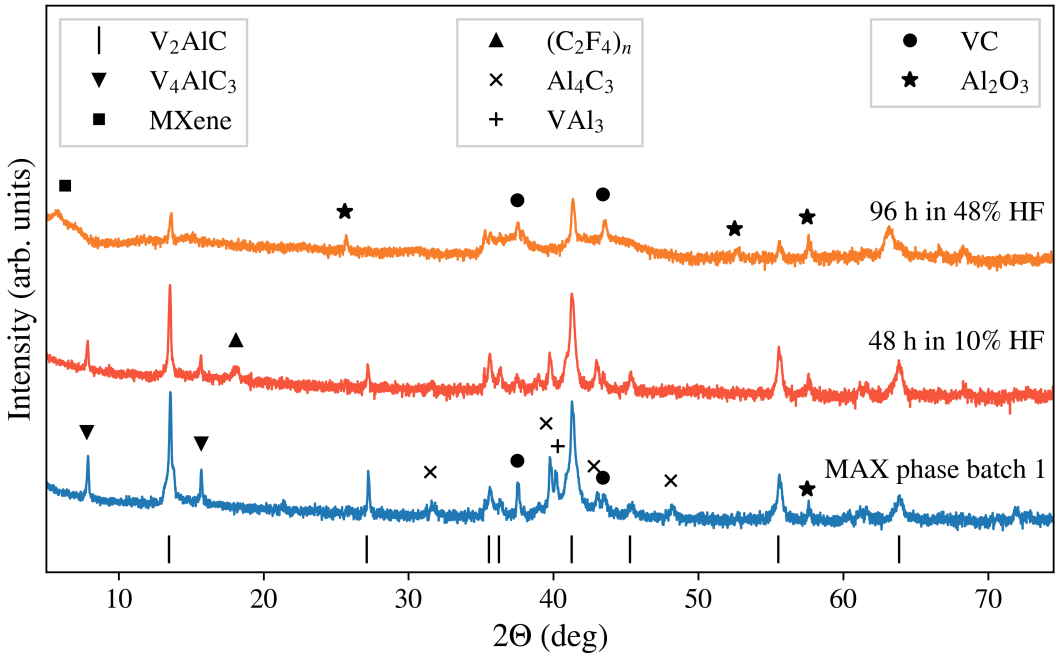

Figure 4.3: Logarithmic XRD plots of the 1st MAX phase batch, both before and after being etched with two different etching conditions (48 h in 10% HF and 96 h in 48% HF). Both processes involved the etching of 0.5 g of the initial MAX phase powder in a 15 ml (10%) and 10 ml (48%) HF solutions.

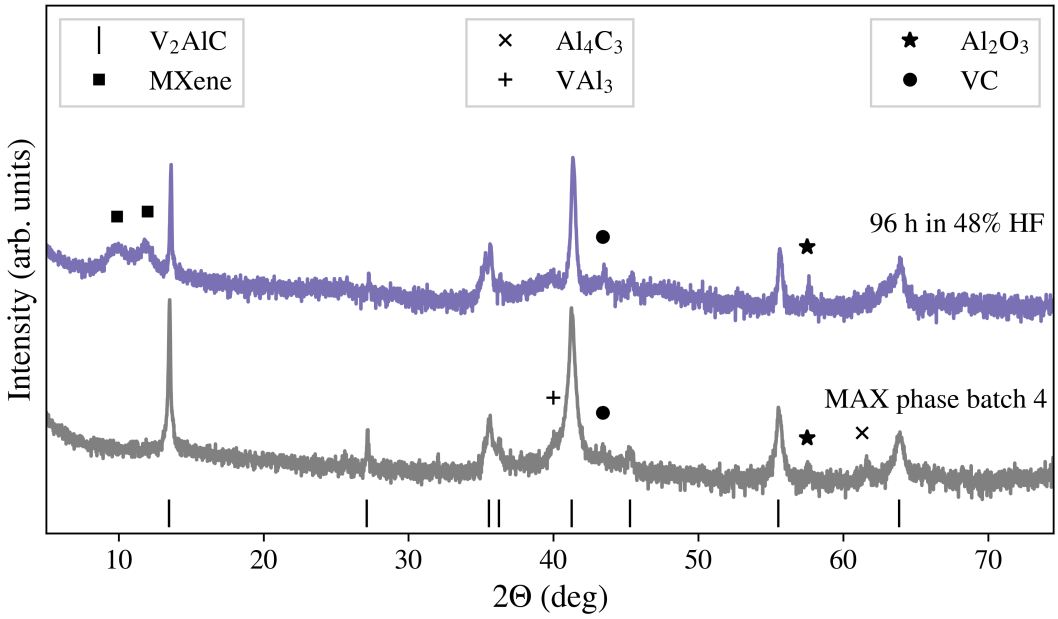

Figure 4.4: Logarithmic XRD plots of the 4th MAX phase batch, both before and after being etched (96 h in 48% HF). This process involved the etching of 4 g of the initial MAX phase powder in a 30 ml HF solution.

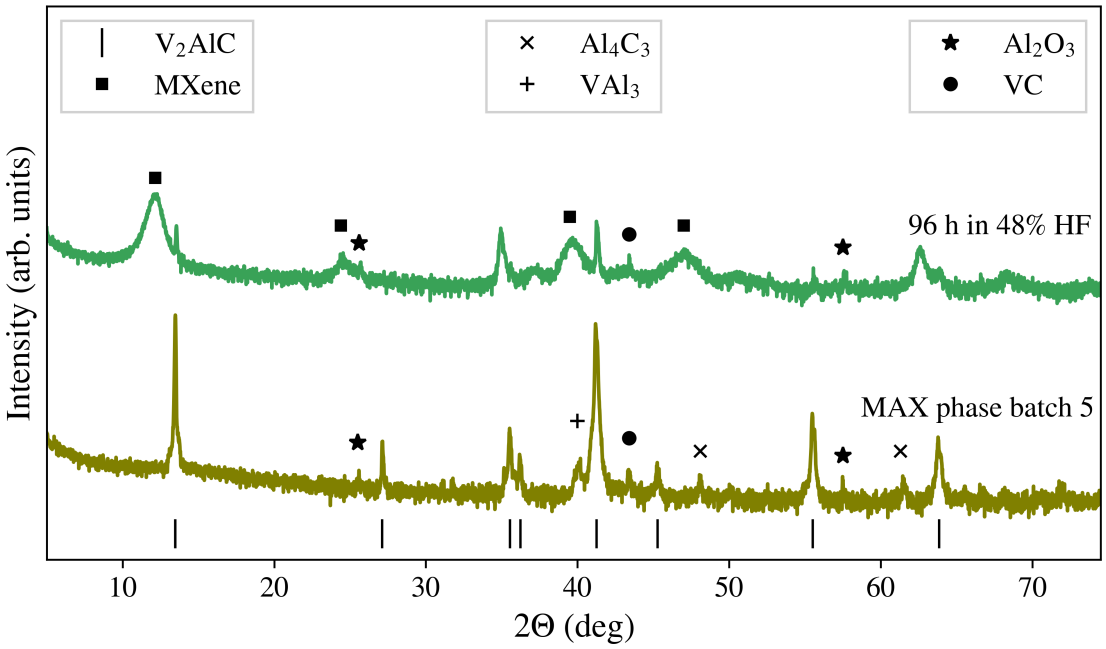

Figure 4.5: Logarithmic XRD plots of the 5th MAX phase batch, both before and after being etched (96 h in 48% HF). This process involved the etching of 3.5 g of the initial MAX phase powder in a 30 ml HF solution.

The etching of batch 4 and batch 5 (96 h, 40% HF) also showed signs of V_2C MXene being formed, as illustrated in Figures 4.4 and 4.5. The plots show an apparent reduction of the V_2AlC-related peaks after etching, and a shift of the (002) peak to lower 2Θ values related to an increased interlayer distance. Figures 4.4 and 4.5 also show the removal of VAl_3 and Al_4C_3 peaks, and the still remaining peaks related to VC and Al_2O_3.

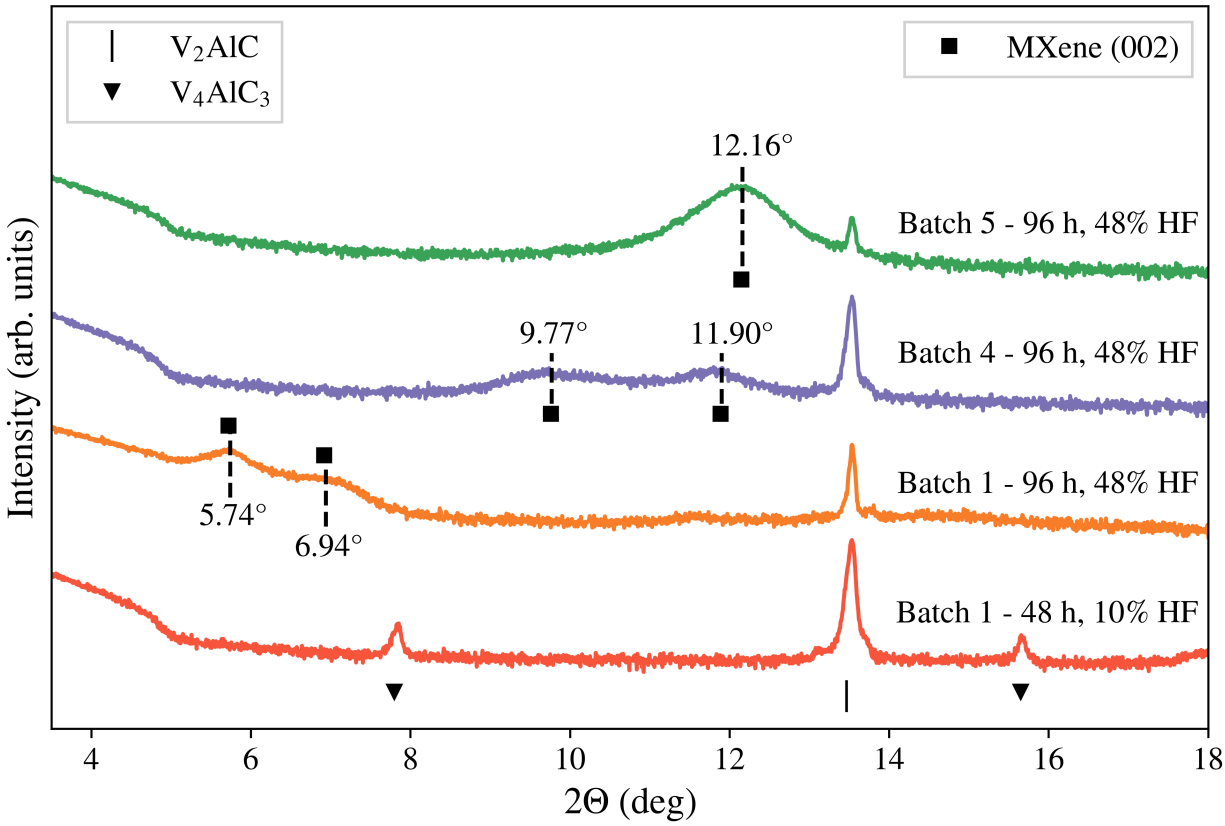

Figure 4.6: Logarithmic XRD plots of the etched MAX phase batches, marking the peak locations for the different (002) MXene peaks.

Particle size distribution and morphology

Figure 4.7 shows SEM images of the powders obtained after etching MAX phase batch 1 (4.7a-b), batch 4 (4.7c-d) and batch 5 (4.7e-f), using 48% HF for 96 h.

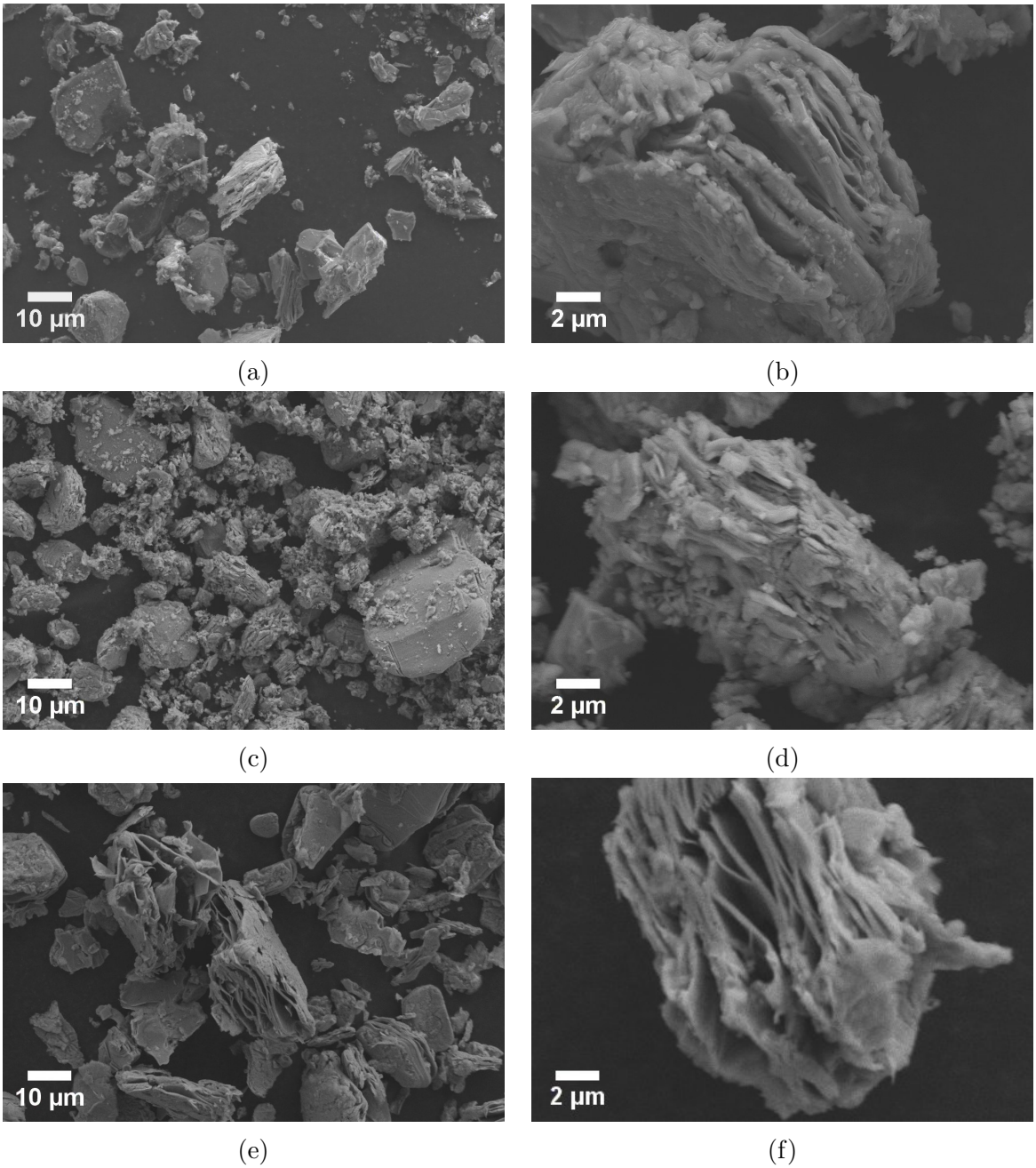

Figure 4.7: SEM images showing the obtained powders after etching MAX phase batch 1, 4 and 5, using 48% HF for 96 h. Images (a-b) represent the etching of 0.5 g of the 1st batch in a 10 ml solution, (b-c) show the result of 4 g of the 4th batch etched in a 30 ml solution, and (e-f) illustrate the particles after 3.5 g of the 5th batch was etched in a 30 ml solution.

After the etching process, all powders still showed a significant spread in particle sizes. Even though the covering layer of submicron particles was removed from the particles in MAX phase batch 4, some amount of smaller particles were still present. MAX phase batch 1 showed a similar trend, whereas the 5th batch showed small amounts of agglomerated submicron particles. In general, a flaky accordion-like appearance can be observed by several of the particles, especially those obtained from the etching of MAX phase batch 5.

4.2.3 Preintercalation and delamination of V_2C

Synthesis yield

The attempts of preintercalating the V_2C structure with TBAOH, followed by delamination to few layered V_2C, resulted in noteworthy mass changes. Table 4.4 presents the mass yield for the two treatments of the V_2C powder (Batch 5: 48% for 96 h). The 1st delamination attempt resulted in negligible amounts powder, as everything remained stuck on the filter paper after vacuum filtration (Figure A.8).

Table 4.4: The mass yield of the two MXene treatments; TBAOH preintercalation and delamination. The 1st delamination attempt refers to sonication of the TBAOH-containing solution, whereas the 2nd attempt involved handshaking of the solution. The last row represents the sedimented TBAOH-treated V_2C in the centrifugation cup after both of the delamination attempts.

Dispersion nr.	Start mass (g)	Treatment	End mass (g)	Yield (%)
1	0.5	TBAOH preintercalation	0.67	134
2	0.5	1st delamination attempt	0	0
		2nd delamination attempt	0.02	4
		Sedimented powder	0.66	132

Crystallinity, phase purity and interlayer distances

Figure 4.8 shows the XRD plots of the 5th batch of V_2AlC, both before and after etching, as well as after TBAOH treatment and the 2nd delamination attempt of the multilayered V_2C.

The TBAOH treatment resulted in a shift of the MXene peaks towards lower 2Θ-values, together with no significant change of the peaks related to other structures than MXene.

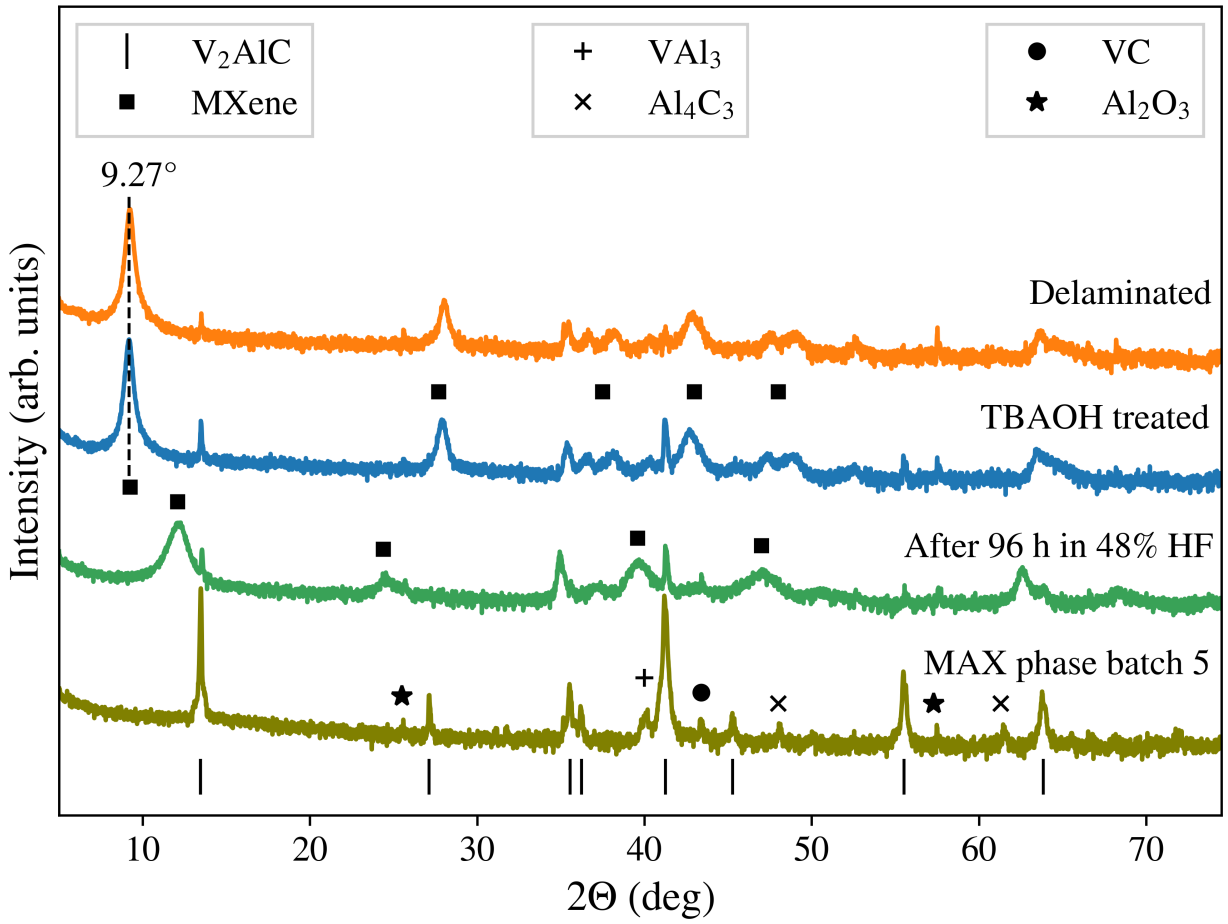

Figure 4.8: Logarithmic XRD plots from the different stages of MAX phase batch 5, going from V_2AlC to delaminated V_2C, where the middle stages consist of pristine V_2C and TBAOH-treated V_2C.

The delamination attempt caused a small reduction of the V_2AlC peaks, but apart from that, no significant changes from the only TBAOH-treated powder. Al_2O_3 remains present at all stages of the process.

The 2Θ shift of the XRD peaks related to (002) planes can be used to calculate the interlayer distance between the V_2C flakes, by utilization of Bragg's law [117]. Table 4.5 lists the interlayer distances obtained after the different etching processes and MXene treatments, together with their respective shifts from the initial V_2AlC structure.

Table 4.5: The interlayer distances obtained after the different etching processes and V_2C preparation methods, together with the shift in interlayer distance from the initial V_2AlC structure (6.6 Å). As the etching of MAX phase batch 1 and 4 with 96 h in 48% HF resulted in two peaks, they are represented by two distinct interlayer distances. Considering that MAX phase batch 1 also contain V_4AlC_3, and that etching might give rise to V_4C_3 MXene as well, the shifts relative to V_4AlC_3 (interlayer distance of 11.4 Å [116]) are included in parenthesis. TBAOH treatment and delamination was completed on the material from Batch 5 - 96 h, 48%.

Material	(002) peak angle	Interlayer distance (Å)	Shift (Å)
Batch 1 - 48 h, 10%	-	-	-
Batch 1 - 96 h, 48%	5.74° and 6.94°	15.4 and 12.7	8.8 (4.0) and 6.1 (1.3)
Batch 4 - 96 h, 48%	9.77° and 11.90°	9.1 and 7.4	2.5 and 0.8
Batch 5 - 96 h, 48%	12.16°	7.3	0.6
TBAOH treated	9.27°	9.5	2.9
Delaminated	9.27°	9.5	2.9

Particle size distribution and morphology

Figure 4.9 shows SEM images of the TBAOH-treated V_2C and the attempted delaminated V_2C, at two different magnifications (1k and 5k). Figure 4.10 shows an additional high magnification image of the TBAOH-treated V_2C, demonstrating the layered structure and accordion-like morphology of the V_2C particles.

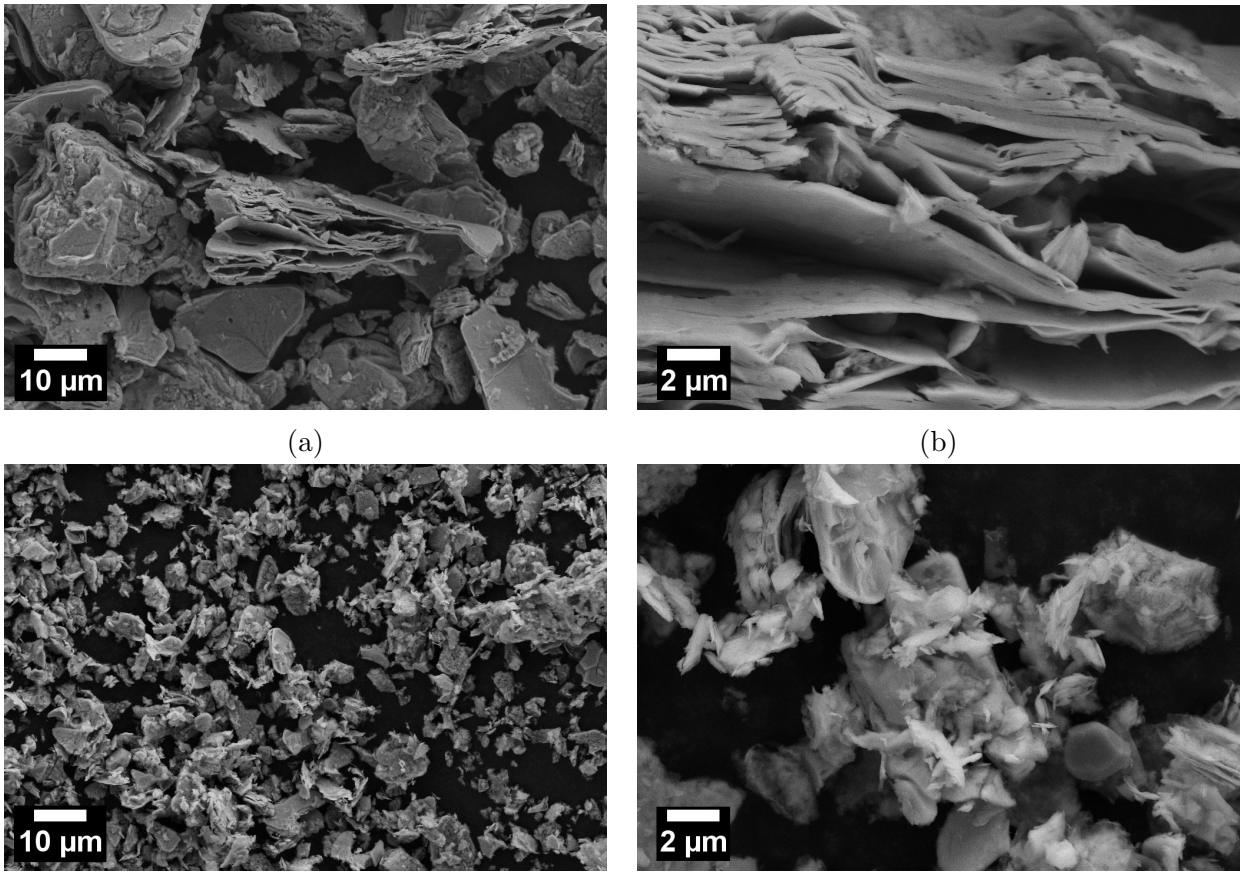

Figure 4.9: SEM images of the V_2C powder from the etching of MAX phase batch 5, where (a)-(b) represent the powder after TBAOH treatment V_2C, while (c)-(d) depicts the powder after TBAOH treatment and delamination by hand shaking.

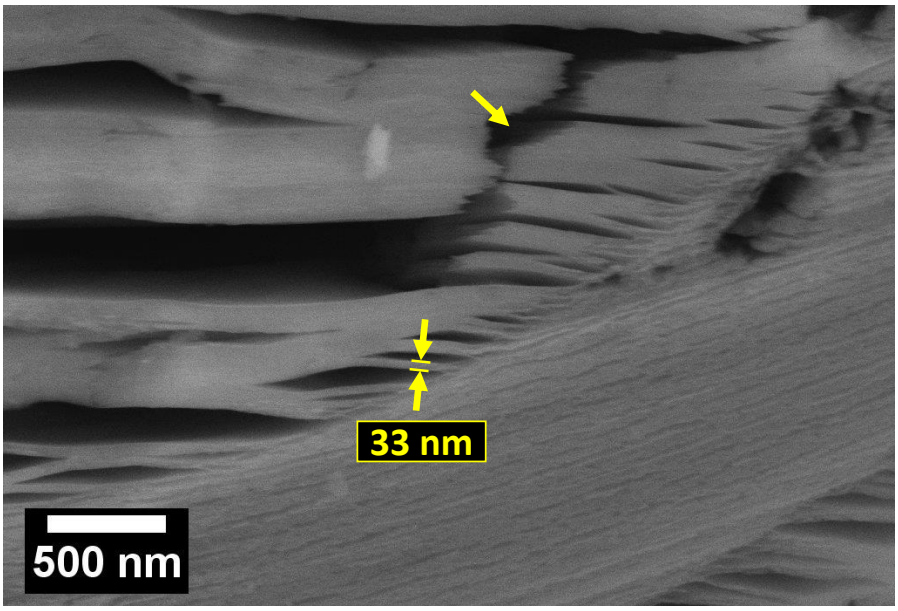

Figure 4.10: High magnification SEM image of a part of a TBAOH-treated V_2C particle, showing the layered structure of the MXene material.

The morphology of the TBAOH-treated particles are similar to the pristine particles, as seen in Figure 4.7e, with the accordion-like morphology of generally larger particles (>1 µm). From the high-magnification image (Figure 4.10) the separation of "macro-flakes" can be observed, with varying thicknesses. By utilizing the interlayer distance of this TBAOH-treated V_2C material (9.5 Å, from Table 4.5), it can be calculated that the 33 nm thick macro-flake represents approximately 35 layers of V_2C. The thickness of the macro-flakes does, together with the spacing between them, vary substantially. Figure 4.10 also shows a crack formation between some of the larger macro-flakes.

The powder obtained from the 2nd delamination attempt, as shown in Figures 4.9c and 4.9d, resulted in a substantial reduction of particle sizes. The particles are generally smaller than 10 µm, and showed a less structured accordion-like morphology, as compared to the non-delaminated particles.

Elemental analysis

Table 4.6 shows the EDX data obtained from the different stages of MAX phase batch 5, from pristine MAX phase to delaminated MXene. In order to present the data in a more useful way, the atomic ratio of the different elements are described relative to vanadium, which is represented by a value of 2. Hence, the atomic ratios describes the amount per V_2C layer.

As the powders are distributed on carbon tape, in addition to the uncertainty of EDX with light elements, the contribution of carbon has been omitted from the table. Representative plots of the EDX measurements are presented in Appendix A.

Table 4.6: EDX measurements from the different stages of MAX phase batch 5; starting with pristine V_2AlC MAX phase, after etching (V_2C), after TBAOH treatment, and after delamination of the TBAOH-treated powder. The atomic ratios are normalized to two vanadium atoms.

Material	V	Al	F	O	N	K
MAX phase batch 5	2	1.19	-	0.49	0.32	-
V_2C	2	0.10	1.12	0.45	0.43	-
TBAOH-treated V_2C	2	0.20	1.31	0.73	0.36	0.25
Delaminated V_2C	2	0.16	0.86	0.61	0.36	0.19

A SEM image of the dried TBAOH solution is shown in Figure 4.11, depicting the presence of precipitated particles on a sea of organic TBAOH molecules. These particles were found to consist of substantial amounts of potassium (Figure A.5), and therefore indicate the presence of significant potassium impurities in the TBAOH solution.

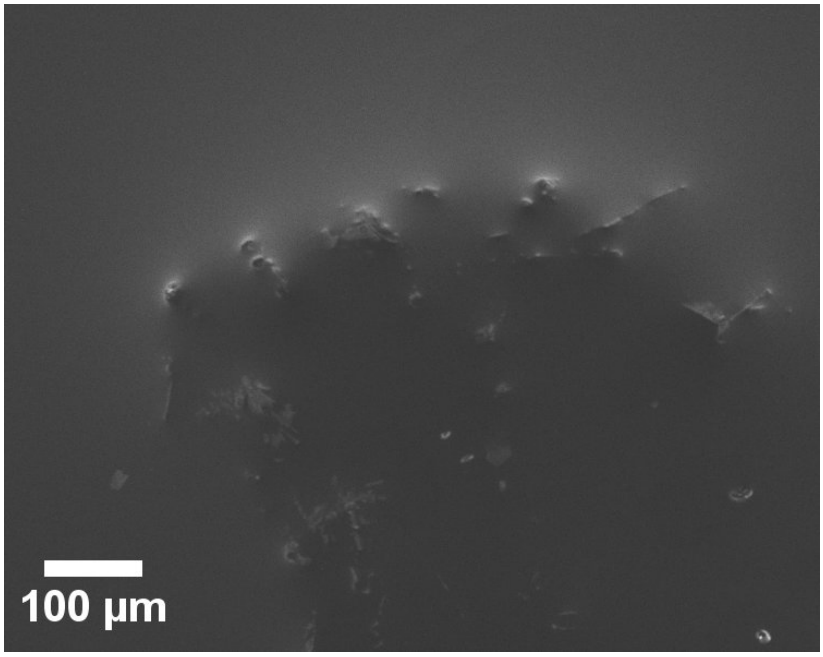

Figure 4.11: The precipitates observed on the surface of the dried TBAOH solution.

4.3 Electrochemical characterization

4.3.1 Electrolyte verification

The CV scans of the APC:THF and the $Mg(TFSI)_2/MgCl_2$:DME electrolytes are shown in Figure 4.12. The former shows close to symmetric cathodic currents from 0 to -0.9 V and anodic currents from 0 to 1 V, followed by negligible currents from 1 to ∼2.7 V. Then, a tiny anodic current tail is observed. In contrast, the $Mg(TFSI)_2/MgCl_2$:DME scan shows small and non-symmetric anodic and cathodic currents, where the anodic current starts as high as 1.5-2V.

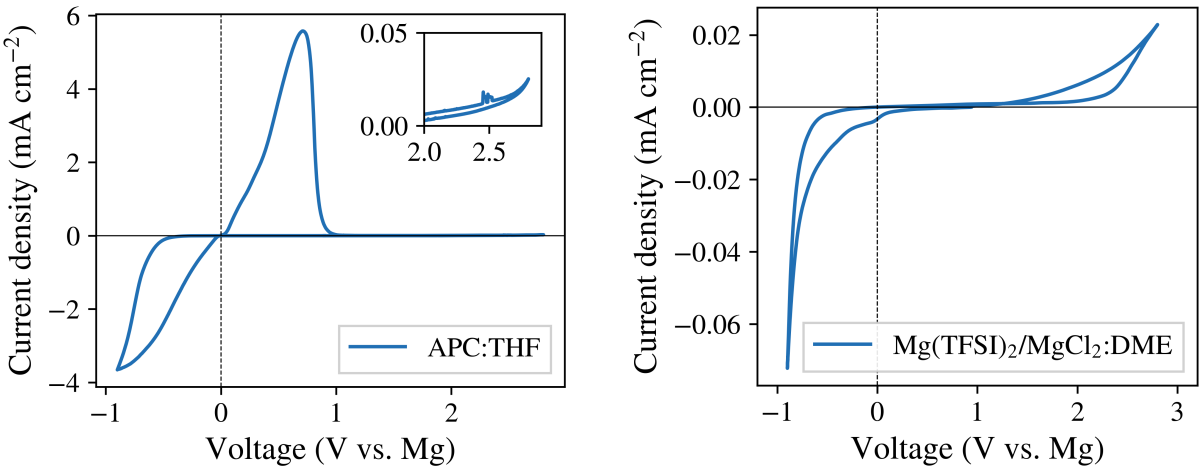

(a) (b)

Figure 4.12: Representative CV curves of Mg plating/stripping, with the use of APC:THF (a) and $Mg(TFSI)_2/MgCl_2$:DME (b) electrolytes. The experiments were carried out on graphite paper, at 1 mV s^{-1}, with Mg metal as both reference and counter electrode. The inset on Figure 4.12a shows the anodic current tail starting at around 2.7 V.

4.3.2 Overview of the cycled batteries

As described in Figure 3.1, batteries were assembled with the use of four different active materials. To simplify the difference between the cycled cells, the active materials will from now on be distinguished by the MXene material present, and the MXene treatments that have been completed. The etched powder from the 1st MAX phase batch is termed "V_2C + V_4C_3", due to the likely presence of both MXenes, whereas the etched 5th batch material is termed "V_2C". The last two active materials are termed "V_2C + TBAOH" and "$d-V_2C$", as

they have been treated with TBAOH and attempted delaminated, respectively. Due to the very limited amount of obtained $d-V_2C$, only APC:THF was tested for this active material. The rest of the active materials were cycled with both the APC:THF and the APC/LiCl:THF electrolyte.

4.3.3 All phenyl complex

Cycling at room temperature

Figures 4.13 and 4.14 present the cycling results from the four different active materials, with the use of the APC:THF electrolyte, operated at room temperature. The former figure shows the results from the V_2C + V_4C_3 active material from MAX phase batch 1, while the latter represents the active materials obtained from different treatments of MAX phase batch 5. Figure 4.15 presents the cycling results of a reference cell containing carbon black as the active material. This cell was assembled and cycled by the co-supervisor of this thesis.

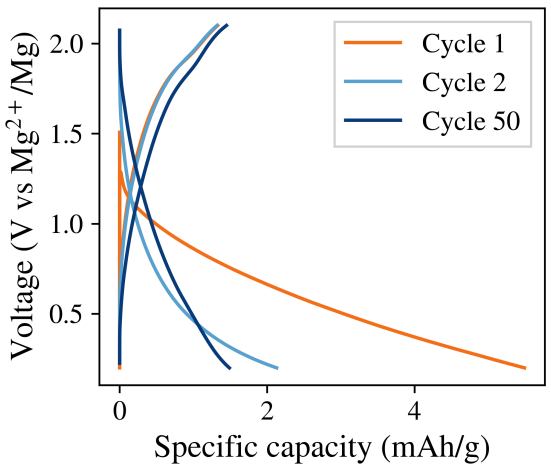

(a) V_2C + V_4C_3

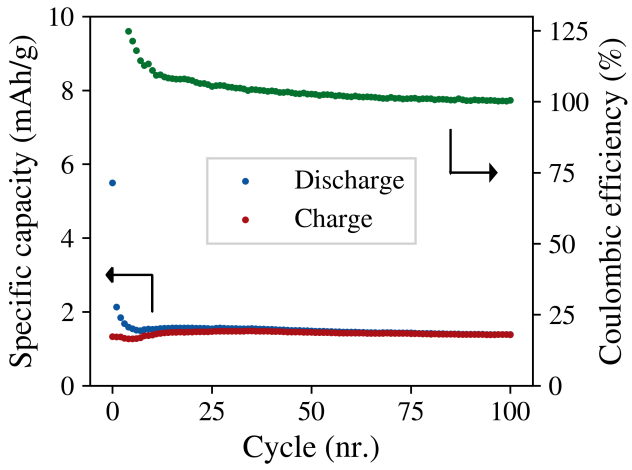

(b) V_2C + V_4C_3

Figure 4.13: Voltage profiles (a) and capacity (mAh/g active material) per cycle (b) of a cell utilizing the the APC:THF electrolyte and the V_2C + V_4C_3 active material, operated with a C-rate of 0.02 C (9.4 mA/g) at room temperature.

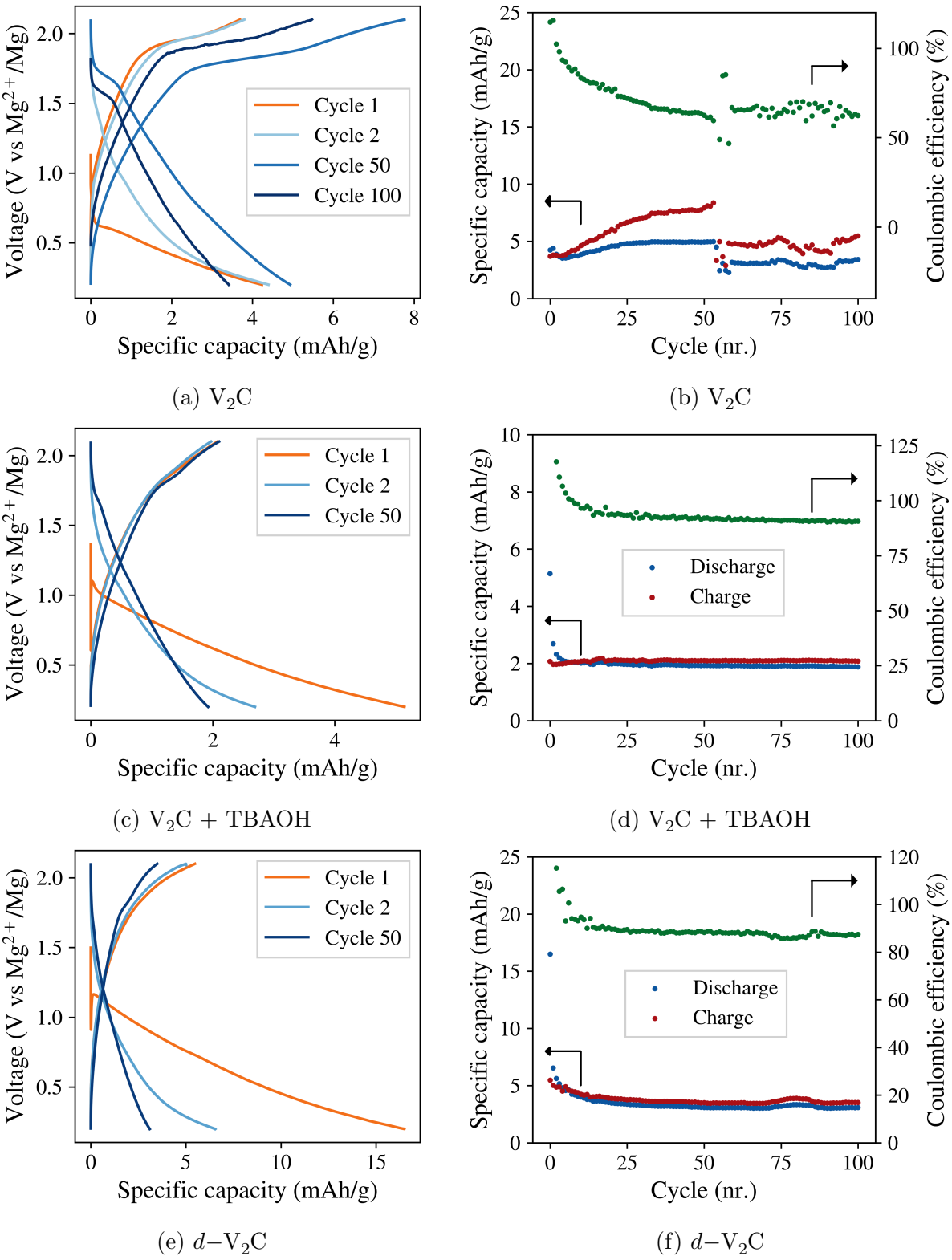

(a) V_2C

(b) V_2C

(c) V_2C + TBAOH

(d) V_2C + TBAOH

(e) $d-V_2C$

(f) $d-V_2C$

Figure 4.14: Voltage profiles and capacity (mAh/g active material) per cycle of cells containing the APC:THF electrolyte, operated with a C-rate of 0.02 C (9.4 mA/g) at room temperature. The subcaptions describe the utilized active material.

Common for these voltage profiles is a low capacity, and a general sloping of the (dis)charge curves. A charge plateau at around 1.8 V can be observed for most of the active materials, where the plateau is most obvious for the V_2C active material (Figure 4.14a). The same cell also showed a tiny discharge plateau at a slightly lower voltage of 1.6-1.7 V. Noteworthy, as can be seen in the capacity plot (Figure 4.14b), this cell showed a substantial reduction of capacities at the 54th cycle. The cell stabilized once again, however with a higher overpotential between the charge and discharge reactions, as seen in the cycling plot.

Most of the cells had a relatively high first discharge (5-16 mAh/g active material), before quickly stabilizing at a certain capacity after a few cycles. The V_2C + V_4C_3 stabilized to the highest coulombic efficiency of all the cells ($\sim$ 100%), albeit with the lowest capacity (<2 mAh/g active material). The $d-V_2C$ active material showed the highest capacity after 100 cycles, but still only around 3 mAh/g.

The reference results from the carbon black cathode (Figure 4.15) show sloped voltage profiles and capacities stabilizing at around 2 mAh/g and 100% efficiency.

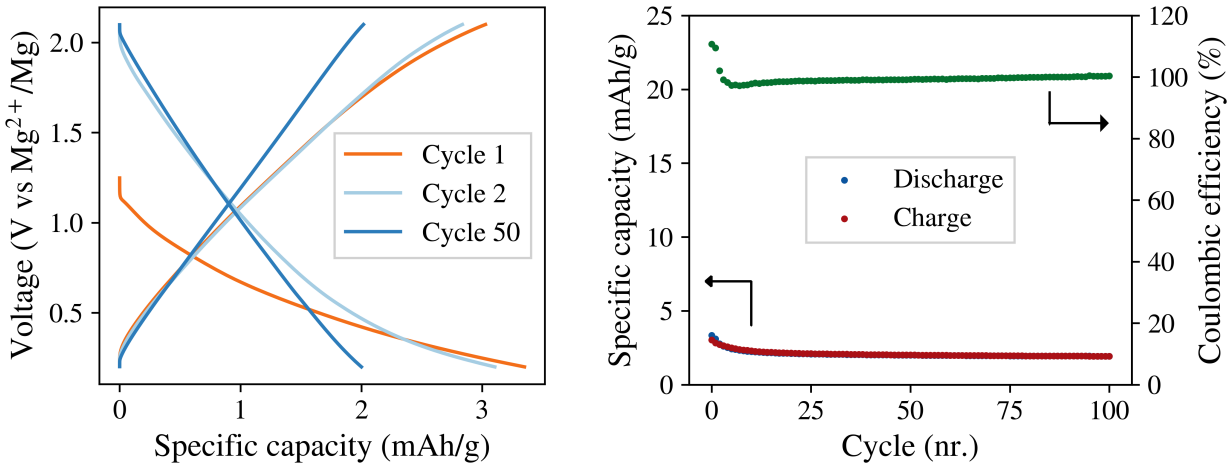

(a) Carbon black

(b) Carbon black

Figure 4.15: Voltage profiles (a) and capacity (mAh/g active material) per cycle (b) of a carbon black cathode, operated at room temperature, with the APC:THF electrolyte.

Cycling at 50 °C

Figures 4.16 and 4.17 present the cycling results from the four different active materials, with the APC:THF electrolyte and an operating temperature of 50 °C. The former figure shows the results from the untreated active material (V_2C + V_4C_3 and V_2C), while the latter shows the active materials obtained from different treatments of MAX phase batch 5 (V_2C + TBAOH and d−V_2C).

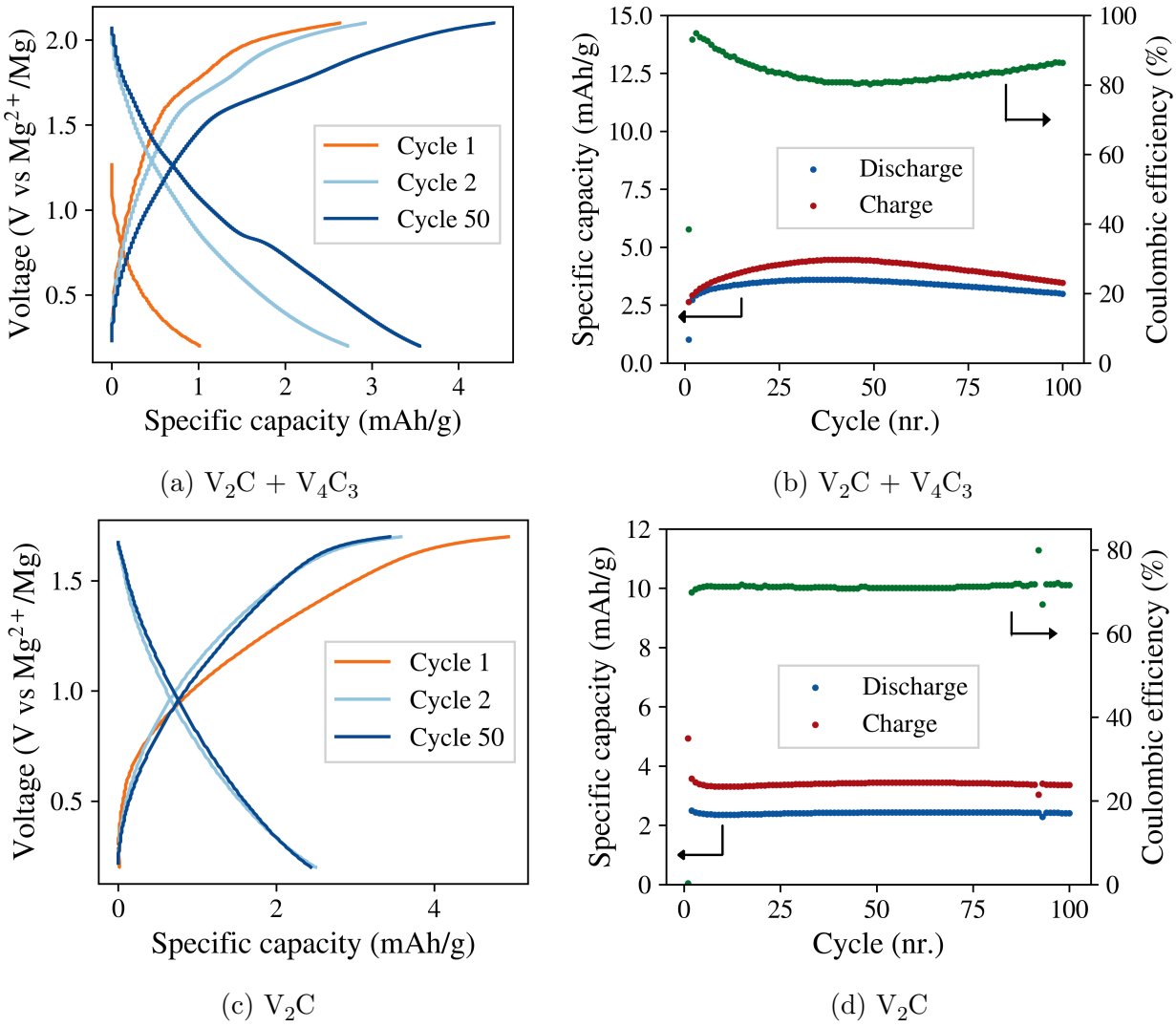

(a) V_2C + V_4C_3

(b) V_2C + V_4C_3

(c) V_2C

(d) V_2C

Figure 4.16: Voltage profiles (a) and capacity (mAh/g active material) per cycle (b) of cells utilizing the APC:THF electrolyte, operated with a C-rate of 0.02 C (9.4 mA/g) at 50 °C. The subcaptions describe the utilized active material.

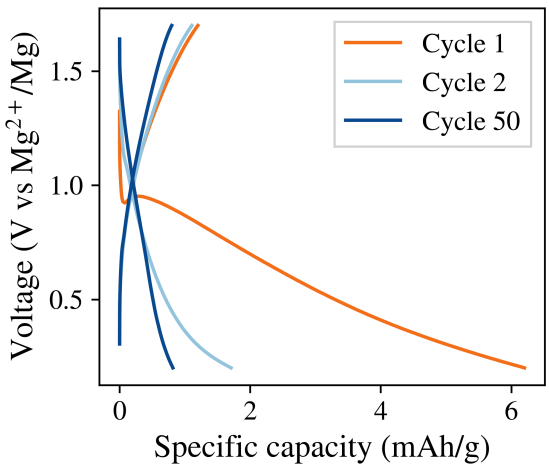

(a) V_2C + TBAOH

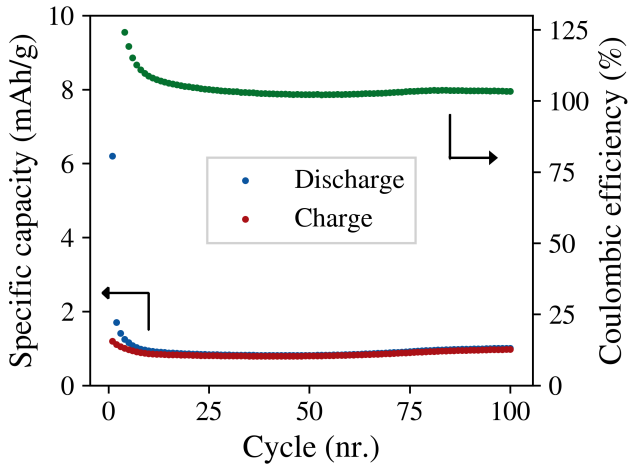

(b) V_2C + TBAOH

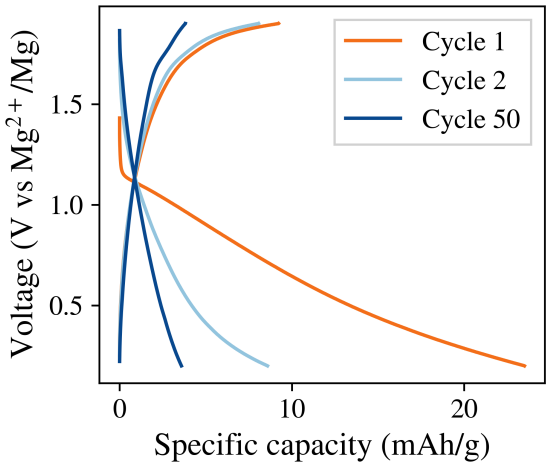

(c) d−V_2C

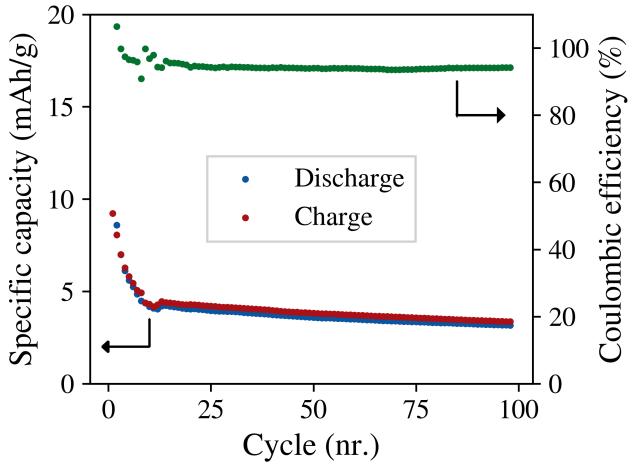

(d) d−V_2C

Figure 4.17: Voltage profiles and capacity (mAh/g active material) per cycle of cells containing the APC:THF electrolyte, operated with a C-rate of 0.02 C (9.4 mA/g) at 50 °C. The subcaptions describe the utilized active material.

In similarity to the cells operated at room temperature, these cells show a low capacity upon cycling, as well as a general sloping of the (dis)charge curves. No significant changes in capacity or coulombic efficiency compared to the cells operated at room temperature can be observed.

Being the only cell to be charged up to 2.1 V, the V_2C + V_4C_3 containing cell is the only one that shows tendencies towards charge plateaus at around 1.6 V. It also shows a discharge plateau at the 50th cycle, and a general reduction in the overpotential between the discharge and charge curves.

4.3.4 Lithium containing electrolyte

Cycling at room temperature

Figure 4.18 and 4.19 present the cycling results from a representative battery of the V_2C + V_4C_3, V_2C and V_2C + TBAOH active materials, with the APC/LiCl:THF electrolyte and being operated at room temperature. Some of these cells were tested at higher C-rates than 0.02C, which is indicated in the given figures.

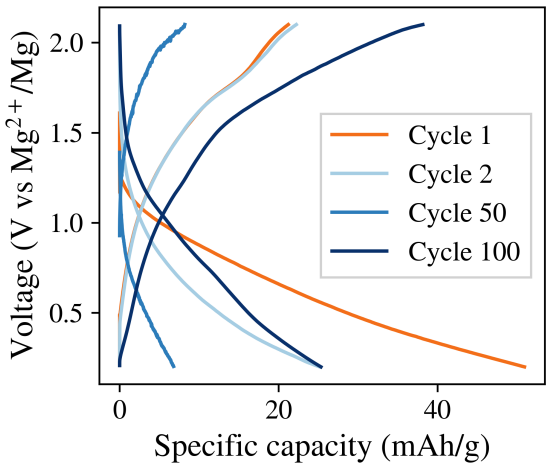

(a) V_2C + V_4C_3

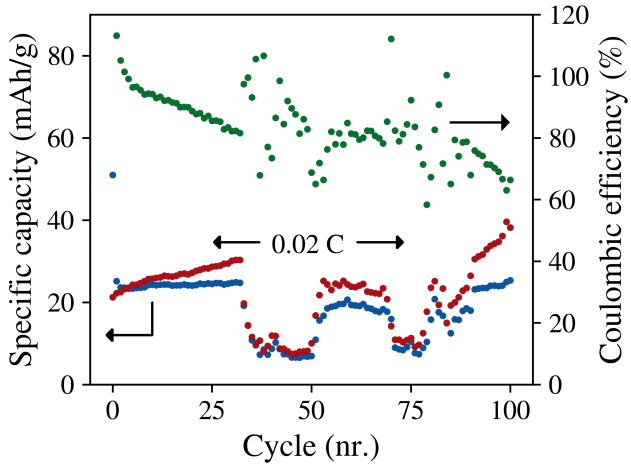

(b) V_2C + V_4C_3

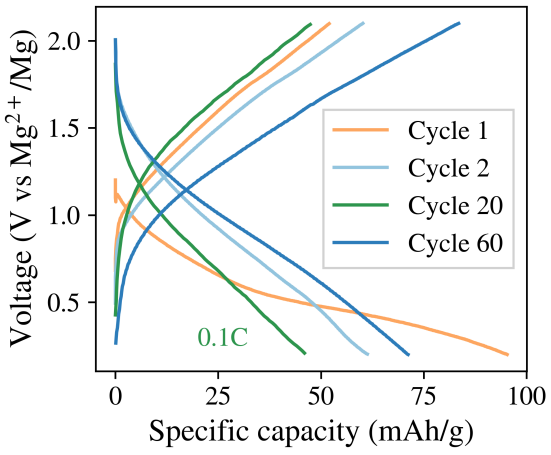

(c) V_2C

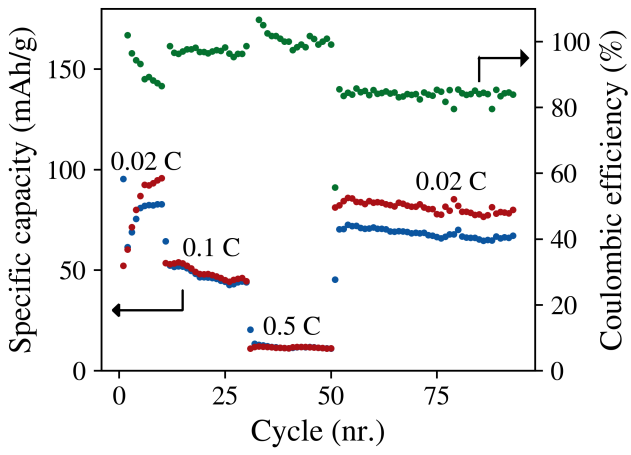

(d) V_2C

Figure 4.18: Voltage profiles and capacity (mAh/g active material) per cycle of cells containing the APC/LiCl:THF electrolyte, operated at room temperature. The subcaptions describe the active material, and where not specified a C-rate of 0.02 C (9.4 mA/g) was utilized.

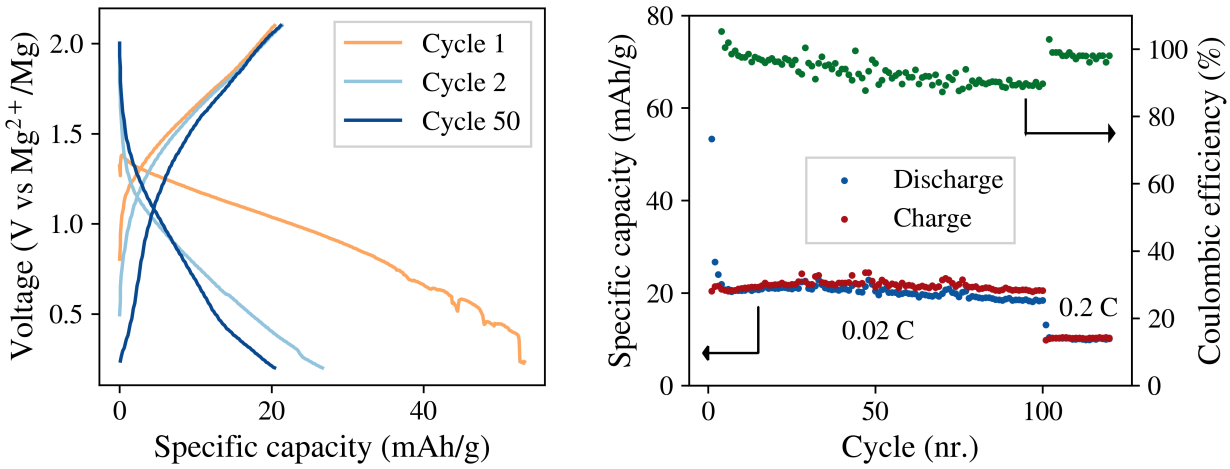

(a) V_2C + TBAOH (b) V_2C + TBAOH

Figure 4.19: Voltage profiles and capacity (mAh/g active material) per cycle of cells containing the APC/LiCl:THF electrolyte, operated at room temperature. The subcaptions describe the active material, and where not specified a C-rate of 0.02 C (9.4 mA/g) was utilized.

The cycling results from the LiCl-containing electrolyte show a significant increase of capacity, as compared to APC:THF containing cells. With first discharge capacities between 50 and 100 mAh/g, this represents more than a tenfold increase. The tenfold increase also holds for the retained (dis)charge capacities. The efficiency development of these cells is, on the other hand, more unstable than those obtained with the APC:THF electrolyte.

The V_2C + V_4C_3 containing cell showed some interesting behaviour. On the 34th cycle, the capacity suddenly dropped with around 80%, which also resulted in an unstable voltage profile, as shown in the 50th cycle (Figure 4.18a). It also resulted in a significantly unstable coulombic efficiency, varying by up to 40% between certain cycles. However, upon prolonged cycling , it once again recovered the capacity, showing its highest (dis)charge capacities at the last cycle. This cell was also the only cell to show voltage plateaus at around 1.6 V upon charge, with the use of the APC/LiCl:THF electrolyte.

The increased C-rates resulted in increased efficiencies, however, at the cost of reduced capacities. For the V_2C containing cell (Figure 4.18d), increasing the C-rate from 0.02 to 0.1 resulted in halving the capacity, which also was the case for the V_2C + TBAOH active material upon increasing the C-rate from 0.02C to 0.2C.

Cycling at 50 °C

Figures 4.20 and 4.21 present the cycling results from a representative battery of the V_2C + V_4C_3, V_2C and V_2C + TBAOH active materials, with the APC/LiCl:THF electrolyte, operated at 50 °C. Some of these cycling measurements were not completed before the end of this project, and thus only a limited amount of cycles are presented here.

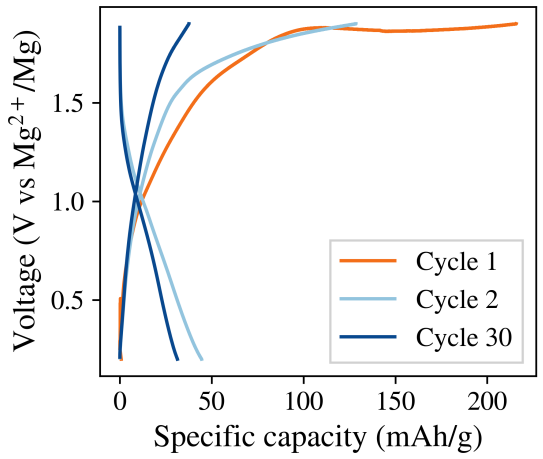

(a) V_2C + V_4C_3

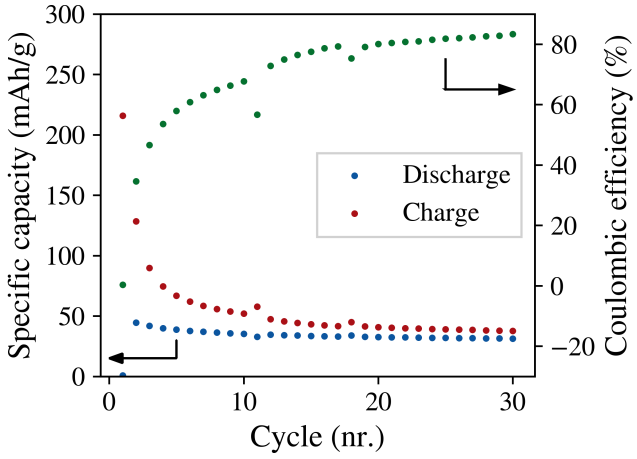

(b) V_2C + V_4C_3

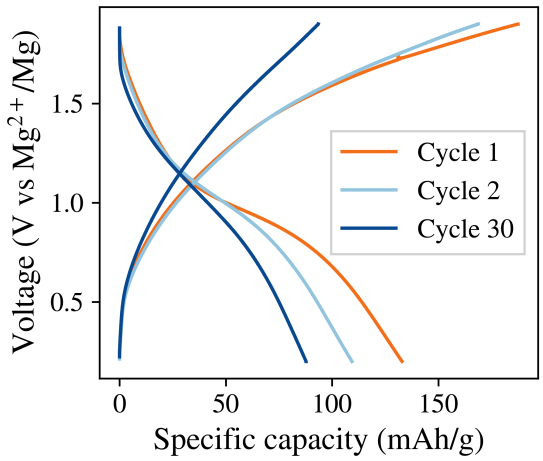

(c) V_2C

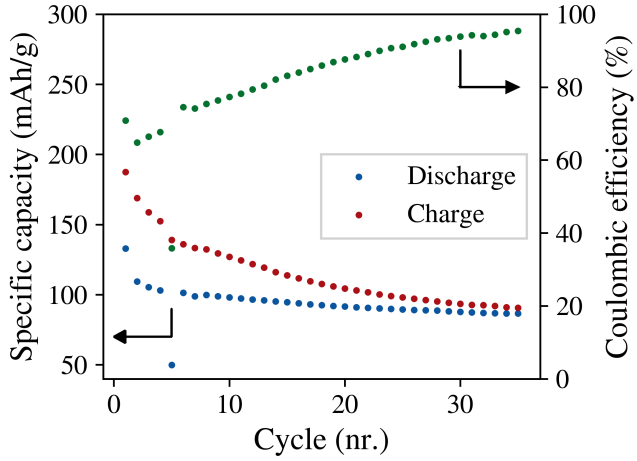

(d) V_2C

Figure 4.20: Voltage profiles and capacity (mAh/g active material) per cycle of cells containing the APC/LiCl:THF electrolyte, operated with a C-rate of 0.02 C at 50 °C. Plots (a-d) contain only a limited amount of cycles, due to the fact that these measurements were not completed before this thesis was to be submitted. The subcaptions describe the utilized active material.

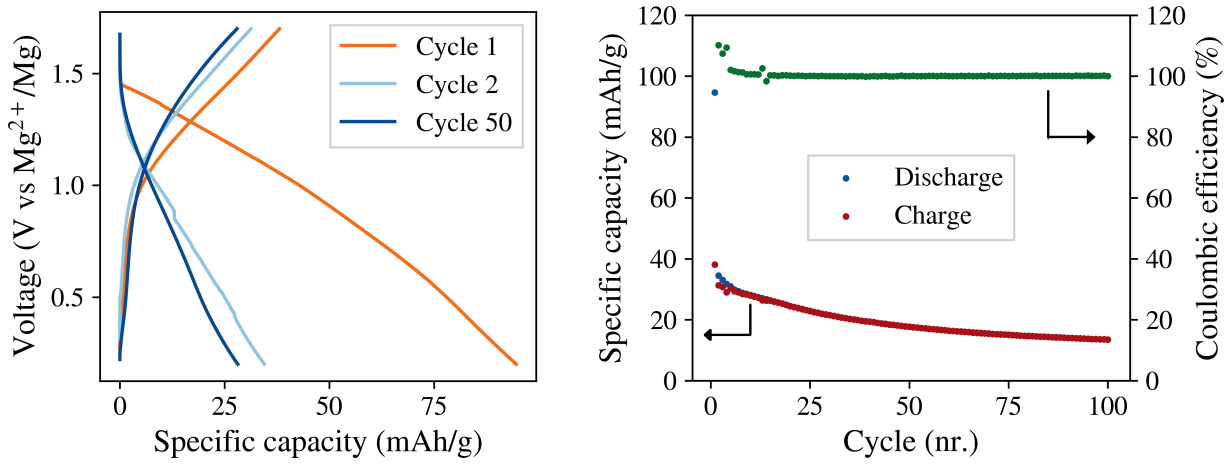

(a) V_2C + TBAOH (b) V_2C + TBAOH

Figure 4.21: Voltage profiles and capacity (mAh/g active material) per cycle of cells containing the APC/LiCl:THF electrolyte, operated with a C-rate of 0.02 C at 50 °C. Plots (a-d) contain only a limited amount of cycles, due to the fact that these measurements were not completed before this thesis was to be submitted. The subcaptions describe the utilized active material.

Compared to the room temperature cycled cells, Figures 4.20 and 4.21 show that an elevated temperature of 50 °C increases the obtained capacity with the Li-containing electrolyte.

The V_2C + TBAOH active material (Figure 4.21a), being the only cell charged up to 1.7 V, showed a first discharge capacity of almost 100 mAh/g. After being charged up to only 1.7 V, the capacity quickly dropped to below 40 mAh/g, followed by a continuous capacity reduction, stabilizing at a coulombic efficiency of around 100%. The other cells show initially high charge capacities, closing in on the discharge capacity upon further cycling, continuously increasing the efficiency.

4.3.5 Summary of cycling performance

A summary of the capacities and average discharge voltages obtained for the different cells is shown in Table 4.7. This table presents the 1st, 2nd, 10th and 50th discharge capacity of the cells, together with the loading of the active material. It also presents an average discharge voltage of the 2nd discharge, indicating an approximate operating voltage of the cells.

Table 4.7: A summary of the cycling results obtained from the different cells; including the loading, the discharge capacity at four different cycles, and the average discharge voltage of the 2nd discharge. The TBAOH-treated V_2C have been denoted TBAOH-V_2C, in order to minimize the space. Some of the capacities were obtained at other cycles than the 50th: * 54th cycle, and ** 30th cycle.

			Loading	Disch. capacity (mAh/g)				Volt.
Electrolyte	Temp.	Act. material	(mg/cm^2)	1st	2nd	10th	50th	(V)
APC:THF	RT	V_2C + V_4C_3	2.21	5.5	2.1	1.5	1.5	0.54
		V_2C	2.80	4.2	4.4	3.9	4.9	0.59
		V_2C+TBAOH	2.82	5.1	2.7	2.0	1.9	0.64
		$d-V_2C$	0.95	16.5	6.6	4.0	3.1	0.58
		Carbon black	0.89	3.4	3.1	2.3	2.0	0.82
	50 °C	V_2C + V_4C_3	2.21	1.0	2.7	3.3	3.6	0.78
		V_2C	3.18	0.1	2.5	2.4	2.4	0.71
		V_2C+TBAOH	3.22	6.2	1.7	0.9	0.8	0.52
		$d-V_2C$	0.72	23.5	8.6	4.2	3.6	0.60
APC/ LiCl:THF	RT	V_2C + V_4C_3	1.98	51.0	25.2	24.3	6.9	0.57
		V_2C	3.68	90.3	61.4	82.8	70.3*	0.84
		V_2C+TBAOH	2.27	53.3	26.7	20.5	21.9	0.68
	50 °C	V_2C + V_4C_3	1.98	0.8	44.5	35.2	31.3**	0.76
		V_2C	3.12	132.9	109.4	98.1	86.6**	0.94
		V_2C+TBAOH	2.90	94.6	34.5	28.2	17.7	0.74

Chapter 5

Discussion

5.1 Overview

This chapter is similarly to the previous one divided into two main sections, addressing the synthesis of V_2C, and the electrochemical characterization of the assembled batteries. The synthesis process will be addressed first, where the emphasis will be on the most critical aspects necessary to obtain phase pure V_2C with high yield, and with suitable particle size distribution and morphology. The second section evaluates V_2C as cathode material for rechargeable magnesium batteries, focusing on reasons for the obtained low capacity and routes to improve the performance. Additionally, hybrid Mg-Li batteries are discussed in light of the performance of the Li-containing electrolyte.

5.2 V_2C MXene synthesis

5.2.1 V_2AlC MAX phase synthesis

As described in Section 4.2.1, MAX phases with different phase purity and particle sizes were obtained from the different synthesis methods. Here, the effects of the drying procedure, the interparticle contact during sintering, and the method used for downsizing the sintered powder will be discussed.

Effect of drying procedure

The drying procedure was found to heavily influence the phase purity of the synthesized V_2AlC MAX phase. Despite being the simplest method, drying in a beaker (1:AIR) resulted in a large range of impurities. The presence of the V_4AlC_3 MAX phase was considered particularly undesirable, considering that it would perturb the results obtained from the etching of the MAX phase, and possibly alter the cathode properties of the active material. Since this thesis aimed for evaluation of the cathode properties of only V_2C, increased V_2AlC purity was desired.

Drying directly in the crucible (2:AIRCR) resulted in a reduction of V_4AlC_3, albeit with a substantial increase in other impurities and reduction of V_2AlC as well. The formation of two separate layers upon sintering, together with the appearance of other impurities, indicate several differences from the other MAX phase batches. With a significant increase in oxygen-containing impurities, the presence of oxygen during the sintering process seems apparent. This oxygen might have come from oxidation of the metal powders before or during the sintering process. However, as the air exposure was not significantly changed from the first batch, this seems rather unlikely, if not the tube furnace was leaking oxygen into the chamber. Another possibility may be that not all of the isopropanol had evaporated from the crucible after the flushing step of the sintering process. This hypothesis is supported by an adjoined increase of carbon-rich impurities (Al_4C_3 and VC), indicating a shift in the V:C molar ratio from the initially weighed powders.

Utilizing the rotavapor to evaporate the isopropanol improved the phase purity of V_2AlC substantially, in addition to reducing the evaporation time. The combined rotation and evaporation enabled by the rotavapor leave a homogeneous powder mixture, whereas drying without rotation will cause the heavier elements to sediment. This is supported by the observed two layers in batch 2, where two additional light impurities (Al_4C_3 and Al_4O_4C) was only observed in the top layer. For batch 1 this was not as apparent, and may be explained by the fact that the beaker was moved during the evaporation, and that the dried powder was mixed once again when being scooped over to the crucible. Even though the rotavapored powder mixtures resulted in less impurities compared to the first batch, the sintered powder in batch 3 (3:ROTA) still showed signs of V_4AlC_3 impurity peaks. This demonstrates that the use of the rotavapor alone, is not enough to prevent the formation of this secondary MAX phase.

Effect of interparticle contact

The contact between the particles upon sintering also showed an effect on the obtained V_2AlC phase purity. First by pellet pressing of the powder mixture, prior to the sintering process, was the V_4AlC_3 MAX phase completely removed. Pressing the particles together thus resulted in an increase of the contact points between the particles during the sintering process, which then reduced local concentration differences.

The drying of the second batch (AIRCR) was an attempt of increasing the contact between the particles, by formation of a continuous film in comparison to the randomly distributed powder in batch 1 (Figure 3.3a). However, as mentioned above, this batch resulted in significant amounts of impurities, indicating that this did not work as intended, or that other aspects were dominating.

Even though the improved phase purity of batch 3 (3:ROTA) has been attributed to the use of the rotavapor, some of the difference in phase purity to the first batch may also be a result of increased contact between the particles. Instead of randomly spreading the powder in the crucible, the powder from the 3rd batch was evenly distributed, lightly packed together by the plastic spatula (Figure 3.3a and 3.3c). It is difficult to tell how much of an effect this had on the result, as this was not the only difference between the two batches. Nonetheless, both the rotavapor and the increase of interparticle contact (by pellet pressing) are found to be important factors for obtaining the correct stoichiometry of the targeted MAX phase.

Effect of downsizing

It was found that the downsizing methods utilized on the sintered powders resulted in significant variations in particle size distributions. As seen in Figure 4.2a-d, dry planetary milling of the powders caused a large amount of submicron particles that agglomerated onto the larger particles. This explains why a long milling time of several hours does not seem to downsize the particles effectively. Figure A.9b also shows how the powder got stuck onto the milling balls and jar after the milling processes, leading to larger losses. In comparison, the mortared powder was easily sieved through the 325 mesh sieve after only $\sim$ 30 min of mortaring, making it the favoured method of these two.

The planetary milling of batch 4 also resulted in a significant broadening of the XRD peaks (Figure 4.1, 4:ROTA-PEL and 4:ROTA-PEL-MIL), which is attributed to reduced crystallite sizes and/or strain within the particles. This is to be expected with the use of high

energy milling [118], and therefore has to be taken into account when choosing a method for downsizing the MAX phase powder.

Synthesis evaluation

With respect to phase purity, yield, time efficiency and a narrow size distribution, it is found that using the rotavapor for drying, pellets during sintering, followed by downsizing using a mortar gave the best V_2AlC MAX phase in this work. Still, there are several adjustments that could improve the V_2AlC powder before the subsequent etching step.

Regarding the phase purity of the synthesized material, there is still room for improvements. As seen in the XRD plot of the last MAX phase batch (5:ROTA-PEL-MOR, replotted for clarity in Figure 5.1), there are still some impurity peaks left after utilizing both the rotavapor and pellet pressing. These impurities consist of Al_2O_3, Al_4C_3, VAl_3 and VC, where all of them have been observed in previous reports [116, 119]. In order to further optimize the phase purity of the synthesized V_2AlC MAX phase, there are several parameters that can be adjusted; optimization of the molar ratio of V:Al:C, minimization of the exposure to air, optimization of the pressure used for pellet pressing and the sintering program (gas composition, dwelling step, heating rate, max temperature, time at max temperature, cooling rate). For example, Hu et al. [119] have reported the synthesis of phase pure V_2AlC with a reduced carbon content and a smaller excess of Al (V:Al:C = 2:1.2:0.9) compared to this work (2:1.3:1), by hot pressing of the pellets during sintering. Adapting this molar ratio could be a promising approach as the observed impurities in this work generally contain more Al and C as compared to V, and considering that a reduced carbon content has worked for the synthesis of other MAX phases as well [120, 121].

Reducing the particle sizes also reduces the time needed to etch out the aluminum from the MAX phase, and may therefore be preferred for the synthesis of V_2C. Naguib et al. demonstrated that while the 400 mesh powder needed 90 h to be completely etched, the attrition milled powder required only an etching time of 8 h to complete the aluminum exfoliation [34]. On the other hand, obtaining an acceptable size distribution of such small particles was found difficult using dry planetary milling. In order to improve the homogeneity of the size distribution of the particles, other methods for downsizing should be considered. For example, the agglomeration of submicron particles could be prevented by the use of wet milling with an aqueous surfactant [122], thereby allowing for a continued size reduction of the particles. To further narrow the particle size distribution, one opportunity would also be to separate the particles by mass with the use of centrifugation [123, 124].

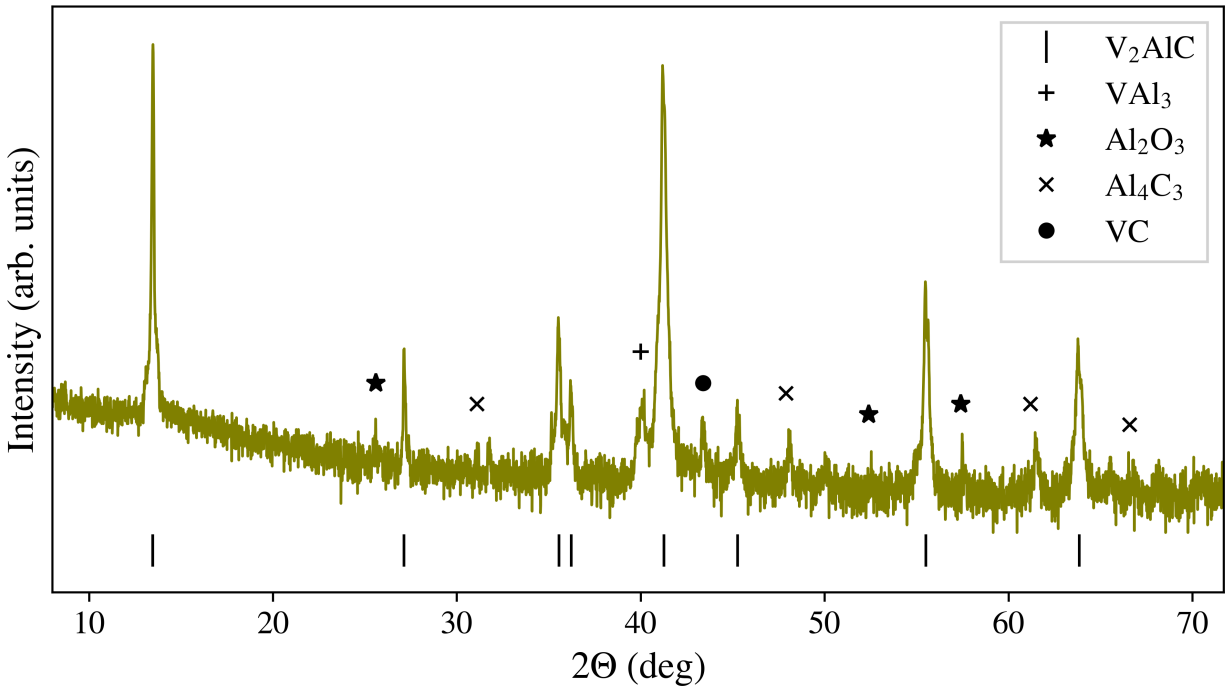

Figure 5.1: Larger logarithmic XRD plot of MAX phase batch 5, as already presented in Figure 4.1.

It should be noted that the XRD scans were relatively quick (<1 h) , resulting in rather rough spectra (much noise). In order to do useful quantitative analysis on the structural content, i.e. by Rietveld analysis, together with an improved qualitative analysis, finer XRD scans would be preferred. Additionally, due to the large variation in peak intensity ratios between the two major V_2AlC peaks (at 13.5° and 41.3°), which is assumed to come from the preferred basal orientation of the particles, an improved standardized method for sample preparation should possibly be aimed for.

5.2.2 Etching of V_2AlC MAX phase

Effect of the HF concentration and etching time

As mentioned in Section 2.3.2, three of the most critical etching parameters are the HF concentration, etching time and the size of the MAX phase particles, which were also observed in this work. Considering that the attrition milled powder in [34] only required 8 h in a 50% HF solution for successful Al-exfoliation, together with the HSE issues associated with the handling of concentrated HF solutions, it was decided to first test a lower HF concentration,

to see if it resulted in any signs of V_2C being formed. With 10% HF etching for 48 h, it resulted in negligible change of the first MAX phase batch, removing only the VAl_3 impurity. This indicates that the etching of aluminum atoms from the VAl_3 impurity happens before the onset of exfoliation of the V_2AlC MAX phase. By extending the etching time with the same concentration, it is possible that more changes could have occurred. However, to the author's knowledge, there has been no reports of successful etching of V_2AlC with HF concentrations lower than 48%, which might indicate a certain concentration needed to initiate the exfoliation.

The second etching was extended to follow the reported parameters of 48% HF etching for 96 h. This resulted in a complete removal of V_4AlC_3 and Al_4C_3, a significant reduction of V_2AlC, remaining impurities of VC and Al_2O_3, and the formation of MXenes, as indicated by the (002) peaks at lower 2Θ angles. Noteworthy, the strong reduction of V_4AlC_3, as compared to V_2AlC, may indicate a difference in V-Al bond strengths of the two MAX phases, considering that a significant amount of V_2AlC still remains after the etching. This is different from the Ti-based MAX phases, where Ti_3AlC_2 shows stronger Ti-Al bonds than Ti_2AlC [125], and generally require higher HF concentrations[106]. Another explanation could be that the amount of V_4AlC_3 impurities consist of smaller particles than V_2AlC, which results in a reduced etching time needed for complete exfoliation.

The same HF concentration (48%) and etching time (96 h) showed similar results for the last two etching processes, demonstrating that these etching conditions are able to exfoliate substantial amounts of Al from the V_2AlC MAX phase structure, and increase the interlayer distances of the V_2C MXene versus the V_2AlC. Estimating the ratio between V_2C and V_2AlC from the XRD plots is not straightforward, due to the less ordered structure of the etched particles, producing weaker and broadened diffraction peaks. The intensity differences of the V_2AlC (002) peak before and after the etching may, however, give a certain indication to how much of the MAX phase that remains unreacted. With etching 4 (Batch 5 - 96 h, 48%) resulting in the largest reduction, it is apparent that this powder resulted in the highest degree of exfoliation. From the change of aluminum content presented in Table 4.6, an approximate MXene yield of 91% can be calculated, when assuming V_2AlC to be the only contributor of Al. The same table also shows a significant increase in F content after the etching, which indicates the formation of a considerable amount of F termination groups on the V_2C surfaces (V_2CF_x) under the given etching parameters.

Even though the three last etching processes utilized the same HF concentration and etching time, they resulted in substantial differences in the obtained interlayer distances, the particle morphology and the mass yield.

Effect of particle size distribution and morphology

One significant effect of the particle size distributions was the mass yield, as shown in Table 4.3. For etching 2 (batch 1 - 96 h, 48%), more than 80% of the initial powder was lost during the synthesis. Even though the etching process removes most of the aluminum from the structure, this should only represent a reduction of less than 20% from the initial V_2AlC material. One of the reasons for the excessive losses, is related to the vacuum filtration of the etched powders, where a significant amount of the etched powder remained on the 0.45 µm pore sized filter paper (Figure A.7a). In order to reduce the amount of stuck powder, the pore sizes of the filter paper should ideally be much smaller than the dried particles, and therefore a 0.22 µm pore sized filter paper was bought and utilized for the following filtration processes. This worked nicely for the mortared powder from MAX phase batch 5, resulting in the highest yield of all the materials etched at 48% for 96 h. However, the planetary milled powder (MAX phase batch 4) still had difficulties being removed from the 0.22 µm filter paper, presumably due to the smaller particle sizes compared to the only mortared powder. In order to keep the losses to a minimum, either filter paper with smaller pores has to be used, or a limited particle size reduction prior to the etching would be required. Other ways of drying the powder could also be a possibility.

Another factor leading to losses is related to the difficulty of sedimenting small particles upon washing of the etched powder. Figure A.9a shows the formation of a green supernatant after the first centrifugation step, which was discarded due to the high concentration of HF. This colour has also been observed during the etching of the Ti_3AlC_2 MAX phase, and has been explained by a colloidal dispersion of Ti_3C_2 MXene [126]. With a maximum rotation speed of 4350 rpm, a longer centrifugation time would possibly be needed in order to fully sediment the etched powders of smaller size. However, in order to complete the washing of the powders within a reasonable amount of time, the centrifugation time per washing iteration was not increased, and a certain amount of powder loss was therefore expected. An increased rotation speed would be preferred in order to increase the yield of the etching process.

The etching had a small effect on the obtained particle sizes of the MXene particles. As a result of the smaller particles being lost in the etching process, the etching step generally removed most of the agglomerated submicron particles from the MAX phase powders. Beyond that, the particle sizes remain relatively stable upon etching, where the obtained particle sizes reflects the particle sizes of the initial MAX phase, which was as expected (Section 2.3.2).

The general disc-like morphology of the MAX phase particles may also have played an im-

portant role for the etching results. Considering that the HF molecules diffuse in between the V_2AlC layers, it is in fact these lateral dimensions of the particles that would define the etching conditions required for complete exfoliation. The formation of the V_2C macro-flakes comes from the expansion of H_2 gas molecules being formed within the particles, during the etching of the aluminum atoms (Equation 2.13). This gives rise to the accordion-like morphology of the etched particles, which seemed apparent for all the etched powders (Figure 4.7), but most distinct for the only mortared powder (batch 5 - 96 h, 48%). One possible explanation could be a lower degree of exfoliation, resulting in only small regions of the particles being etched, and thus allowing the van der Waals forces to hold the macro-flakes together. This could possibly have come from the agglomerated particles shielding the surfaces of the larger particles from the HF molecules upon the initial stages of the etching process. Another possibility is the complete separation of the macro flakes from the remaining particles, due to increased amounts of dislocations in the planetary milled powders (batch 1 and 4). As seen in Figure 4.10, cracks in the V_2C macro-flakes occur, and with more dislocations, it is not unlikely that these flakes will be completely detached from the host particle. Due to a lower mass, these detached macro-flakes would then presumably be discarded with the supernatant solutions upon washing of the etched powders.

For battery applications, the formation of macro-flakes may be both positive and negative. On one side, it opens up the material, increasing the surface area of easily accessible MXene. On the other side, it also increases the volume of the particles, without increasing the number of intercalating sites. Considering that the V_2C MXene is meant to work as an intercalating cathode material, the macro-flakes therefore results in a decrease in the obtainable volumetric capacity.

Differences in interlayer distances

Even with the use of equal HF concentrations and etching times, none of the etching processes resulted in similar interlayer distances. As presented in Table 4.5, the interlayer distances varied from 7.3 Å (batch 5 - 96 h, 48%), to 15.4 Å (batch 1 - 96 h, 48%). In comparison, the articles following a similar procedure [37, 34, 36], also reported of varying interlayer distances, being either around 10 Å or 8 Å. The latter report also showed a 2.3 Å expansion of the interlayer distance after insertion of sodium-ions. Common for all of them is the formation of only one (002) peak, and thus only one interlayer distance, dissimilar to what was obtained after the etching of MAX phase batch 1 and 4 (96 h, 48%). For the etching of batch 1, the two peaks can presumably be explained by the presence of two different

MAX phases in the etched powder (V_2AlC and V_4AlC_3). However, the etched powder from MAX phase batch 4 contained only one of the MAX phases (V_2AlC), implying that the peaks represent 2 distinct interlayer distances of the same MXene material. One possible explanation for multiple interlayer distances might be the large variation of particle sizes for the planetary milled powder (batch 4 - 96 h, 48%). Naguib et al. [34] showed that the attrition milled MAX phase resulted in a lowering of the peak angle for the (002) planes, which might suggest the effect of different particle sizes being etched. On the other hand, the shift of the peak angle was achieved using other etching conditions than for the non-attrition milled particles, which makes this explanation uncertain.

With the limited characterization information available, it is difficult to explain the large variation in interlayer distances. As mentioned in Section 2.3.3, water molecules tend to intercalate into the V_2C structure, and various amounts of water molecule layers may therefore represent one possible explanation. However, considering that all of the powders were etched, and more importantly dried, similarly, this seems unlikely, as a difference of up to 8 Å would represent several layers of water molecules. Further investigation of the water content, i.e. by extended vacuum drying of the powders, would therefore be of interest in order to ensure the water content within the MXenes. Fourier-transform infrared spectroscopy (FTIR) and could also be utilized to inspect the presence of O-H bonds related to water molecules.

Synthesis evaluation

With respect to the exfoliation of Al from the V_2AlC MAX phase structure, it is found that a high HF concentration (48%) and long etching time (96 h) was needed in order to result in substantial formation of V_2C MXene. Furthermore, the particle size of the initial MAX phase material is shown to affect the MXene yield, the general mass yield of the process, and the particle size of the etched powder. Still, there are many parameters that have not been addressed in this thesis that influence the etching results. Hence, there are many possibilities for optimizing the resulting V_2C material for a RMB cathode application, where the most important factors are listed as follows:

- Increase phase purity of V_2C
- Reduce V_2C particle sizes
- Alteration of the termination groups
- Increase the interlayer distance

In order to increase the phase purity of the V_2C material, there are mainly two improvements that would be required. The first one relates to the increased phase purity of the etched MAX phase powder, considering that the VC and Al_2O_3 impurities are not removed during the etching process. Secondly, the V_2AlC material would have to be completely etched, in order to optimize the yield of V_2C. The most obvious answer would be to extend the etching time, ensuring enough time for all particles to be completely etched. However, due to the currently unknown effects of excess etching, further investigation would be required. In order to ensure equal etching of all the particles, it would be necessary to also have a narrow lateral size distribution of the initial MAX phase particles. Furthermore, other etching conditions, together with different etchants, can be explored as a means of increasing the phase purity of the etched powder. There are several parameters that could be optimized, such as the ratio of MAX phase powder to HF solution, the etching temperature that is utilized as well as the HF concentration. One report also shows the selective etching of Al from the V_2AlC MAX phase with the use of NaF and HCl (forming HF *in situ*) [35], which reduces the need for direct handling of HF solutions.

Further reduction of V_2C particle sizes would result in generally larger surface area and reduced diffusion lengths for possible intercalants, and can be achieved by several methods. First of all, the particle size of the initial MAX phase powder can be reduced. However, this would likely result in reduced mass yield, as discussed earlier. Another option would be to downsize the etched powder by mortaring or some other sort of dry milling method. This would avoid the problem of vacuum drying smaller particles, but will likely also affect the morphology of the etched particles. An additional possibility is to delaminate the particles, which has been attempted here, and will discussed in the upcoming section.

An aspect of the V_2C MXene that has not been fully addressed in this thesis is the importance of the termination groups. The material properties, including the theoretical capacity and Mg-ion diffusion, are dependent on the surface termination groups [32, 127], and should therefore be controlled in order to optimize the Mg-ion intercalation capabilities of the V_2C structure. As the EDX measurements showed high amounts of F, in addition to O, it is likely that the main termination groups were -F, -O and -OH, which is to be expected (Section 2.3.2). The high amount of -F terminations can be attributed to the use of concentrated HF. However, further characterization is needed, such as FTIR and/or XPS, in order to determine the termination groups quantitatively.

With the highest V_2C yield, the most homogeneous size distribution, and only one distinct interlayer distance, the powder from etching 4 (MAX phase batch 5) was defined to result in the best V_2C MXene of the last two etching processes. It was therefore utilized for the

further treatments of the V_2C material.

5.2.3 Preintercalation and delamination of V_2C

TBAOH preintercalation

As mentioned in Section 3.2.3, the main motivation for treating the V_2C material with a TBAOH solution is to increase the interlayer distances, together with the possible alterations of termination groups. The former was accomplished, resulting in a 2.2 Å increase in interlayer distance from the pristine V_2C. The sharpening of the (002) peak also indicates a more defined interlayer distance than for the untreated V_2C, which presumably comes from the intercalated molecules being of equal size. The mass increase of more than 30% (Table 4.4) also confirms the addition of more material into the MXene powder. On the other hand, with the introduction of potassium (Table 4.6) it is likely to assume that a significant amount of this increased mass comes from spontaneously preintercalated potassium cations. As the previously reported changes in interlayer distances after similar TBAOH treatment have been 9.4 Å [23] and 5.7 Å [37], it might even be that no TBAOH molecules have preintercalated into the structure at all. Without supporting EDX data indicating a significant increase of nitrogen content, there is in fact no clear evidence of the preintercalation of TBAOH molecules into the structure. Further characterization, using nuclear magnetic resonance spectroscopy (NMR) and/or FTIR would therefore be needed in order to define the exact outcome of this treatment method.

To explain the possible failure of TBAOH preintercalation, one significant difference from the previous reports was the initial low interlayer distance between the pristine V_2C material. This may have resulted in a too small gap for the TBAOH molecules to preintercalate into. In comparison, both the mentioned reports started off with interlayer distances of around 10 Å, whereas the spacing of the V_2C used in this work was only 7.3 Å. The smaller spacing could have lead to higher energy barriers for the TBAOH molecules to enter into the structure. Then, after the preintercalation of K-ions, the interlayer gaps may simply have been filled up, leaving no room for more molecules to enter. In general, a purer TBAOH solution should be utilized for future TBAOH treatments, in order to reduce the preintercalation of impurity cations, and thereby simplify the verification of TBAOH preintercalation.

Due to the alkaline TBAOH solution, a substitution of F-terminations with OH-termination was to be expected (Section 2.3.3). However, the EDS measurements indicated no reduction

of F content, even though a slight increase in oxygen is apparent. The alkaline treatment therefore seem to have failed in substituting the F-termination groups on the V_2C surfaces. In order to verify this, more advanced characterization techniques, such as FTIR and XPS, are needed.

Delamination

Before discussing the results of the delamination attempts, it is important to note that the goal was to separate single-layered V_2C flakes, and not the observed macro-flakes, consisting of tens of layers. However, without the use of characterization methods with atomic resolution, the verification of these delamination attempts remains unclear. Still, there are some observed differences before and after delamination. While most of the XRD spectra remains unchanged, there is an apparent reduction of the V_2AlC-related peaks after delamination. Assuming that the remaining V_2AlC after the etching process consists of mostly larger particles, this reduction is reasonable, considering that the larger particles will sediment faster than the smaller ones upon centrifugation and it is the supernatant that is being collected. As seen in the SEM images after the delamination (Figures 4.9c-4.9d), only smaller particles remained in the supernatant, resulting in a substantial reduction of particle size as compared to the non-delaminated particles.

One of the most obvious challenges with the delamination of V_2C is related to the extremely low yield, where most of the powder remained stuck on the filter paper upon vacuum filtration. In contrast, previous reports have demonstrated the formation of free-standing films of the delaminated V_2C MXene, by utilizing filter paper with similar pore size (0.22 µm) [128, 23]. In order to achieve this, three aspects need to be changed. First of all, changing to a hydrophobic filter paper should reduce the amount of powder stuck on the filter paper, and thus make it possible to detach (more of) the dried powder/film. Secondly, the yield of delaminated V_2C in the supernatants should be increased. Due to the small increase in interlayer distance from the TBAOH treatment, as compared to previous reports, the limited swelling of the multilayered V_2C particles may not have been enough to allow for delamination of single- or few-layered flakes. Additionally, the powder/water ratio could be reduced, in order to make room for more delamination. A ratio of around 1 g per 200 ml was used in this work, which is twice the amount of powder as compared to the two mentioned reports. Lastly, in order to form free-standing films of significant size, the pores of the Büchner funnel should be changed, as most of the dried powder was observed to accumulate in small circles over the pores (Figure A.8).

5.3 Electrochemical characterization

5.3.1 Electrolyte verification

The CV scans (Figure 4.12) indicated whether or not the two electrolytes were compatible with the Mg anode, the carbon paper current collector and the remaining coin cell components, within the voltage range at which the cycled cells were operated. The APC:THF electrolyte showed small overpotential and reversible Mg deposition and stripping (Figure 4.12a). In contrast, the $Mg(TFSI)_2/MgCl_2$:DME electrolyte demonstrated a large overpotential, where the Mg stripping started at 1.5-2V. This anodic current could in fact also have been electrolyte oxidation, and generally describes the incompatibility of the $Mg(TFSI)_2/MgCl_2$:DME electrolyte to the utilized battery components.

One possible explanation for this incompatibility may come from $MgCl_2$ not being fully dissolved. Shterenberg et al. have presented similar CV scans in their work [129], showing that increased solvation of $MgCl_2$ greatly reduces the overpotential of the Mg stripping. As the $MgCl_2$ powder was of relatively low purity ($\geq$98%), this might have reduced the solubility of $MgCl_2$ and possibly caused precipitation, which again may have resulted in blocking of the electrodes. Additionally, the Mg electrode may also have been affected by the high water content of the $Mg(TFSI)_2$ powder (7.4%), and thus hindered the stripping/plating properties of the metal. As described in Section 2.2.5, Mg anodes are found to be unstable with water concentrations exceeding 0.1% in non-aqueous electrolytes [92].

Notable for the APC:THF electrolyte is the instability at higher temperatures. As some of the APC:THF containing cells were unable to reach 2.1 V upon charging, it is apparent that the electrochemical window of the electrolyte is sensitive to changes in temperature. Considering that the boiling temperature of the THF solvent is 66 °C, it is, however, not surprising that it is affected by an operating temperature of 50 °C.

The APC:LiCl/THF electrolyte was not tested during this project. However, it was here assumed that it would behave similarly to the APC:THF electrolyte, considering that the standard electrode potential of Li (-3.04 V) is significantly lower than for Mg (-2.38 V) [130]. Li plating would therefore be expected to start at a negative voltage vs. Mg, meaning that it will not react with the anode.

5.3.2 Evaluation of V_2C as a rechargeable magnesium battery cathode material

Clarification

When discussing the results from the cycling of the different batteries, it should be mentioned that these results are based on a limited amount of battery coin cells. The chosen plots for each group of active material are chosen based on being the most representative performance of their respective groups, but still only gives an indication of the effects of different active materials, electrolytes and operating temperatures.

Cycling performance with the APC:THF electrolyte

Considering that the aim of this project has been to explore V_2C as cathode material for RMBs, the most interesting parameter would therefore be the obtained capacity and operating voltage. As summarized in Table 4.7, none of the active materials resulted in significant capacities with the use of the APC:THF electrolyte. Together with the generally sloped voltage profiles, this indicates that most of the capacity comes from the capacitive properties of the material, rather than redox reactions. It is also likely that the carbon black content of the electrode contributes to the obtained capacity, considering that the carbon black cathode exhibited similar capacities and voltage profiles as the V_2C-containing cathodes. There are, however, some significant differences from the voltage profiles of the fully capacitive carbon black cathode.

The voltage profiles from the V_2C-containing cathodes show a trend of higher first discharge capacities, compared to the following charge capacity and subsequent cycles. This might come from the Mg-ions being irreversibly intercalated in between the opening of the V_2C layers. It can also be the result of side reactions. In LiBs, the first cycles are usually used to form the stable SEI layer, resulting in significantly higher initial capacities. However, for RMBs, this is not expected, seeing that the electrolyte is supposed to be stable within the operating voltage window. One common problem for RMB cathodes containing oxygen, is an undesired conversion reaction of insoluble MgO [17]. Due to the probable presence of O- and F-termination groups, it might be that precipitates of MgO, and the even more insoluble MgF_2 may be formed upon cycling, preventing further reactions at later cycles. The generally low coulombic efficiencies do at least indicate some side reactions taking place. In order to obtain information about these reactions, inspection of the cells after cycling would be of

interest, in order to characterize the differences that has occurred.

Another important observation is the voltage plateaus upon both charge and discharge of the cells. While the charge plateaus generally are present from the first cycle, the plateaus for the discharge curves first become observable after the second cycle, which is most obvious for the V_2C active material in Figure 4.14a. While the charge plateau remains at 1.7-2.0 V for all the four presented cycles (1,2,10 and 50), the discharge plateau first appears after the 2nd cycle. This might be an indication of slow reaction kinetics related to the discharge process, which is improved upon prolonged cycling, thereby explaining the sloped voltage curves of the initial discharges. However, without any further characterization of the cathode upon the different stages of the cycling, it is hard to tell what reactions are taking place. CV scans would also enable a better localization of the operating voltages for the different reactions. Interestingly, if the discharge plateau observed at 1.6-1.7 V actually represents Mg-ion intercalation, then it would represent one of the highest operating voltages achieved for a RMB [58].

Effect of elevated operating temperature

The fact that the increased temperature did not result in significant changes on the cycling performance with the APC:THF electrolyte, shows that this alone is not enough to reduce the Mg-ion migration barriers within the V_2C particles. In comparison, increasing the temperature turned out to significantly increase the capacity and stability of the cells utilizing the APC/LiCl:THF electrolyte. This is a significant sign for ion intercalation occurring in the APC/LiCl:THF containing cells.

Comparison of active materials

The similar results for most of the active materials indicates no significant effect of the different treatments of the V_2C particles. In fact, increasing the interlayer distance of the multilayered V_2C by TBAOH treatment resulted in a reduction of the specific capacity of the cathodes. This capacity reduction could partially be a result of the increased mass of the treated particles, which, with no significant increase in Mg-ion intercalation sites, has resulted in a reduction of the specific capacity (mAh/g). Another explanation, could be that the K-impurities block some of the intercalation sites for the Li-ions (with the Li-containing electrolyte), and thus reduces the obtainable capacity. The delaminated particles on the other hand, consisted of significantly smaller particles. The slight increase of capacity for

this active material may therefore be a result of an increase in the surface area, and the more detached morphology of the particles, which increases the number of sites for capacitive contribution. The probable reduced amount of -F terminations may also have enabled for larger capacities. Furthermore, it is apparent that the presence of V_4C_3 MXene did not result in a significant increase in capacity, indicating that this structure was not able to increase the Mg-ion intercalation into the MXene cathode.

5.3.3 Routes for improvements

There may be several explanations as to why the Mg-ions did not intercalate into the V_2C cathode. As mentioned in Section 2.2, the main challenge for RMBs usually relates to the high charge density of the Mg-ions, which again leads to high Mg-ion migration barriers within the structure. Considering the low amount of obtained capacity, it is likely to assume that the same problem occurs for the V_2C cathode material.

One way to reduce the migration barriers is by changing the termination groups to more polarizable ones than the F-terminations. O- and OH-termination groups would be the easiest ones to achieve, and would at least reduce the amount of F-terminations. S is even more polarizable, and is generally used in most RMB cathodes, making it an interesting termination group to allow for Mg-intercalation. In addition P- and Si-terminations have been calculated to significantly reduce the energy barriers related to ion diffusion within the V_2C structure [131]. One challenge with the latter three termination groups (S, P and Si) relates to the synthesis, as, to the author's knowledge, no reports have demonstrated the formation of such termination groups. This makes room for more further work related to MXene treatment. However, it should be noted that increasing the polarizability of the structure, usually comes at the cost of reduced operating voltages. Considering that both capacity and operating voltage are important for the energy density of the cell, it would be extremely important to optimize the polar environment of the MXenes.

Water molecules may also represent a possible way of shielding the cations upon intercalation. As already mentioned, water molecules are found to easily intercalate into the MXene structures. With their dipole moment, they may therefore shield the electric charge of intercalating cations, and therby help to significantly increase the ion migration. In fact, Mg-ions have already been reported to spontaneously intercalate into the Ti_3C_2 MXene in aqueous solutions of 1 M $MgSO_4$ [132] and 0.5 M $MgCl_2$ [133]. Therefore, it would be interesting to see if this also applies for the V_2C MXene. Even though aqueous electrolytes are not compat-

ible with a Mg metal anode, it would still prove a concept for the intercalating possibilities of the MXene material. If this is found to work, experimenting with extra intercalation of water within the MXene structure, while using a non-aqueous electrolyte, might be a way of overcoming the Mg-ion migration barriers. Due to the expected favoured intercalation of water molecules into the MXene structure, it may be that they would remain there upon cycling, preventing the degradation of the metal anode.

Different electrolytes may also have an effect on the intercalation of Mg-ions. More accessible Mg-ions from $MgCl_2$-dissolved solutions, such as the $Mg(TFSI)_2/MgCl_2$:DME electrolyte, may result in weaker interaction energies, and thereby lower overpotentials related to the desolvation of Mg-ions. One natural choice would be to synthesize a new $Mg(TFSI)_2/MgCl_2$:DME electrolyte with higher purity powders. Adjusting the APC concentration in the THF solvent may also affect the properties of the APC:THF electrolyte.

To date, there has only been one report of a MXene cathode showing significant specific capacity. This was done recently by Xu et al. who utilized the filtration of a cationic surfactant (cetrimonium bromide - CTAB) through an already delaminated Ti_3C_2, and thus were able to achieve specific capacities of 90 mAh/g, after initial stabilizing cycles [134]. They also demonstrated a high reversibility of the Mg-intercalation, which was supported by theoretical calculations, showing that the intercalated CTA^+ cations reduced the migration barriers of Mg-ions on the MXene surface. This presents a new intercalant that should be tested for V_2C, namely CTAB, which is similar to TBAOH, consisting of a positively charged, relatively large organic molecule. These results also suggests a requirement of successful cation preintercalation and delamination, in order to achieve Mg-ion intercalation.

An additional possibility would also be to utilize other MXene compositions. Different structures and elements would lead to changes in conditions for the ion intercalation, and may be a way to increase either the capacity or the operating voltage of the MXene cathode. Considering the great amount of MXene candidates (i.e. Ti_3C_2, Ti_2C, Nb_2C, (TiV)C and Ti_3CN) there are a lot of possible MXene candidates that could be tested as RMB cathode material [33]. It should be noted that the co-supervisor of this thesis has worked with the Ti-based MXenes (Ti_2C and Ti_3C_2), during this period. Currently, the results from these MXenes show similar performance to the V_2C MXene presented here.

5.3.4 Hybrid Mg-Li batteries

Li-ion intercalation

In contrast to the APC:THF electrolyte, the Li-containing electrolyte (APC/LiCl:THF) resulted in relatively large capacities (Figures 4.18 and 4.18), proving the ion host capabilities of the V_2C MXene. This is attributed to the smaller charge density of the Li-ions and thereby reduced diffusion migration barriers. As mentioned in Chapter 1, the V_2C MXene has already been reported to work for Li-intercalation. Nevertheless, to the author's knowledge, this is the first demonstration of V_2C MXene as a hybrid Mg-Li battery cathode material.

Ti_3C_2 was the first MXene to be reported as a hybrid Mg-Li battery cathode material, one year ago [135]. The report demonstrated a capacity of (35 mAh/g) with the use of pristine $ml-Ti_3C_2$ at a current density (10 mA/g) similar to what was utilized in this work (9.4 mA/g). As the pristine $ml-V_2C$ in this work demonstrated a discharge capacity of 70 mAh/g even on the 54th cycle, it represents a doubling of capacity from the previously reported Ti_3C_2, indicating a great potential of the V_2C MXene. By delaminating Ti_3C_2, and mixing it with carbon nanotubes, the report also demonstrated a threefold increase in capacity, and a significantly improved rateability. If the same improvement could be achieved with the V_2C MXene, a capacity of more than 200 mAh/g would be obtained, making it a highly interesting cathode material.

Given the used amount of electrolyte (75 µl), the Li concentration (0.4 M) and the amount of active material in the cathode (7.4 mg), the Li-ions could be responsible for all the obtained capacity. By increasing the concentration, an even higher capacity could possibly be achieved.

What makes hybrid Mg-Li batteries especially interesting is the potential of combining high capacity, high voltage, and fast Li-ion intercalation cathodes together with the high capacity, low cost and dendrite-free Mg metal anodes. Still, in order to allow for the use of Mg metal anodes, the number of suitable electrolytes is still very limited. The highest achieved operating voltage has come from the use of a spinel LiMn2O4 cathode (∼2.8 V), resulting in an initial discharge capacity of 106 mAh/g [136]. However, most of the high voltage cathodes suffer from large capacity retentions [137]. One of the best hybrid Mg-Li batteries to date comprise of the Mo_6S_8 chevrel phase and a similar electrolyte (APC/LiCl:THF), demonstrating superb capacity retention (<5% fade for 3000 cycles) and high coloumbic efficiencies, yielding 126 mAh/g at an operating voltage of 1.3 V [138].

Energy density comparison

From Table 4.7 it is apparent that the cell showing the best cycling values was the pristine V_2C cycled at 50 °C. At the 2nd discharge it delivered a specific capacity of 109 mAh/g at an average operating voltage of 0.94 V, which then results in a specific energy density of 103 mWh/g active material. This is 37% less than what is achieved by the best Mg-Li hybrid cathode (164 mWh/g active material), as mentioned earlier. Compared to a commonly utilized LiB cathode material (NMC333), with an energy density of around 565 mWh/g active material [139], the V_2C hybrid Mg-Li cathode material is still far behind. However, if a threefold increase in capacity is achievable by delamination of the V_2C MXene, an energy density of around 300 mAh/g would be obtained. This would make V_2C a very promising cathode material for hybrid Mg-Li batteries.

Chapter 6

Conclusions

The synthesis of phase pure V_2C MXene with high yield, a suitable particle size distribution and morphology was found to be strongly dependent on the synthesis procedure of the V_2AlC MAX phase, as well as the subsequent etching conditions. Optimizing the phase purity of V_2AlC was found to be an important factor in obtaining phase pure V_2C, considering that some of the impurities from the MAX phase remained after etching. The purest V_2AlC MAX phase was achieved by utilization of a rotavapor for the isopropanol evaporation, followed by pellet pressing of the dry powder mixture prior to the sintering process. Upon etching of the MAX phase powder, it was found that high HF concentrations (48 %) and long etching times (96 h) were needed in order to exfoliate substantial amounts of Al. However, in order to ensure the highest degree of etching, a narrow particle size distribution of the MAX phase was found optimal. Dry planetary milling of the MAX phase powders resulted in significant amounts of submicron particles, and a relatively large particle size distribution, leaving steel mortaring as the favoured choice for particle downsizing. The downsizing methods were also found to affect the mass yield of the etching process, and the obtained interlayer distance and morphology of the etched particles. The etching of the planetary milled powders generally resulted in lower mass yield, less separation of V_2C macro-flakes and larger interlayer distances than the etching of the mortared powder. The lower mass yield was explained by the loss of smaller particles in the washing or filtration step of the etching process. The difference in V_2C macro-flakes and interlayer distances were assumed to be a result of less stable macro-flakes and more intercalated water in the possibly more strained particles after milling.

By utilizing the APC:THF electrolyte, poor capacities were achieved (<4 mAh/g active material), where most of the capacity was assumed to come from capacitive properties of the relatively small V_2C particles. The low capacity that was obtained was attributed to the high

charge density of the Mg-ions, which leads to high migration barriers. On the other hand, small plateaus were observed in the voltage profiles at around 1.6-1.9 V, indicating some redox reactions taking place. Furthermore, the V_2C treatments (TBAOH and delamination) did not result in significant changes in obtained capacity, even though the TBAOH treatment resulted in an increase in interlayer distance (2.2 Å) and the delamination lead to a significant reduction of particle sizes. This might, however, be a result of possibly unsuccessful TBAOH preintercalation and delamination attempts.

The inclusion of LiCl into the electrolyte (APC/LiCL:THF) resulted in a significant increase in capacity, which was attributed to the intercalation of less charge dense Li-ions. With a capacity of 70 mAh/g on the 54th cycle achieved by the pristine $ml-V_2C$, this represents an interesting application for V_2C as a cathode material for hybrid Mg-Li batteries.

To sum up, although multilayered V_2C MXene was successfully synthesized, the as-synthesized material was not found to allow for significant Mg-ion intercalation, leading to poor cycling performance as a RMB cathode. However, there are still several alterations that can be done to the V_2C MXene that might improve the intercalating properties of the material, and thereby enable Mg-ion intercalation. Much further work is therefore needed, in order to fully explore the possibilities of this material, and thereby verify its compatibility as a RMB cathode material.

Chapter 7

Further Work

This work has barely scratched the surface when it comes to both the synthesis of V_2C MXene and its possible utilization as a cathode material for rechargeable magnesium batteries. Hence, there are a lot of things that can be improved, building upon the results from this work.

To start off with the initial V_2AlC MAX phase synthesis, it would be interesting to test hot pressing, together with an adjusted molar ratio (V:Al:C of 2:1.2:0.9), in order to further improve the purity of the obtained V_2AlC. A new method for downsizing the synthesized powder would also be required in order to improve the particle size distribution, and possibly allow for further reduction of the particle sizes. An interesting alternative would be to utilize wet planetary milling, with the use of a surfactant.

Regarding the etching of the V_2AlC MAX phase, all of the etching parameters should be optimized, in order to achieve V_2C with suitable properties. Obtaining a correlation between the particle sizes and the etching conditions (ratio of powder to HF solution, HF concentration, temperature, etching time) needed to completely exfoliate the Al layer would be of great interest in the optimization of the etching process. To accomplish this, a more accurate determination of the MAX phase particle sizes would be required, which could be acquired by laser diffraction. Achieving a better understanding of how the etching conditions also affect the formation of different termination groups on the V_2C surface would be an important step in controlling the properties of the V_2C material. In order to do this, new characterization techniques would be needed to identify and quantitatively analyze the termination groups. EDX may continue to be used for a rough approximation of elemental content, accompanied by the use of FTIR, XPS and NMR. Posible alterations of termination groups should also

be investigated, in order to minimize the Mg-ion migration barriers, while at the same time retaining a high as possible operating potential. Due to the high electronegativity of the F-termination, these groups should be removed, and possibly substituted by more polarizable groups, such as O, OH, S, P or Si. As O- and OH-groups are found to be formed upon base treatment of the MXene material, an interesting treatment would therefore be to test a stronger base than the TBAOH solution used in this work.

As the best capacities obtained for MXenes come from cation preintercalated and delaminated MXenes, substantial effort should be directed towards improving these processes. First of all, utilization of a purer TBAOH solution should be tested, but also the use other molecules would be interesting, such as CTAB. The preintercalation of the molecules should then be verified by FTIR or XPS measurements together with EDX and XRD. TEM imaging would also be interesting, in order to visually inspect the interlayer distance between the V_2C layers.

For improved delamination of the preintercalated particles, several parameters could be optimized. Firstly, the interlayer distance of the multilayered V_2C particles should probably be larger than what was achieved after the TBAOH treatment (9.5 Å) in order to sufficiently swell the V_2C particles. This can be achieved by the preintercalation of several organic molecules (i.e. TBAOH and CTAB), or even water molecules. Secondly, a possibly higher centrifugation speed might be needed in order to separate the smaller delaminated flakes from the larger non-delaminated flakes, and thus ensure the removal of non-delaminated V_2C from the utilized supernatant. Lastly, hydrophobic filter paper should be tested, in order to increase the yield of the delamination processes, and possibly enable the formation of free-standing thin films. Hydrophobic filter paper would also be a possible upgrade for all of the vacuum drying processes related to V_2C synthesis and V_2C treatment. In order to verify the presence of delaminated V_2C, and to inspect the number of layers (single- or few-layered V_2C), either TEM or AFM could be utilized.

Considering the complexity of batteries, possible changes to battery components should also be tested. First of all, different electrolytes, with more accessible Mg-ions should be tested, as this may reduce the energy barriers related to Mg-ion intercalation. A possible candidate would be an improved $Mg(TFSI)_2/MgCl_2$:DME, synthesized with purer materials. Considering that extra water within the MXene may help to reduce the migration barriers of the Mg-ions, it would be interesting to test the use of a water intercalated V_2C cathode, and its compatibility with the Mg metal anode. Additionally, testing of an aqueous electrolyte would also be interesting as a proof-of-concept, in order to inspect if the aqueous environment allows for Mg-ion intercalation into the V_2C structure.

Furthermore, in order to better understand the electrochemical performance of the V_2C MXene, the changes of the V_2C cathode upon cycling should be inspected. Structural changes after cycling may be characterized by post-mortem XRD analysis, where a shift in the interlayer distance might be an indication of Mg-ion intercalation. *In situ* in operando XRD would simplify the process, making it easier to observe the changes of a cell at different stages in each cycle. *In situ* XPS and *In situ* in operando XANES could be used to inspect differences in oxidation number of the V atom, indicating whether or not redox reactions are taking place. Additionally, FTIR could be used to indicate possible side reactions.

Så enten in situ XPS (at du overfører sykled elektrode inert til XPS), eller in situ in operando XANES (X-ray absorption near edge structure) for å se på oksidasjonstall under sykling (XANES var det jeg hadde håpet å gjøre).

In light of the interesting performance of V_2C as a cathode material for hybrid Mg-Li batteries, it would also be interesting to test the above-mentioned alterations with a Li-containing electrolyte. If significant improvements could be achieved, this could possibly be a competitive solution to LiBs.

Finally, the experimental results should also be accompanied with more theoretical calculations and simulations, in order to better understand the properties of the V_2C MXene material. This could also be used to give meaningful insight into the challenges related to intercalation of Mg-ions.

The findings and further suggestions will hopefully contribute to continued work on V_2C as cathode material for rechargeable magnesium batteries, possibly opening up for the battery technology to live up to its full potential.

Bibliography

[1] R.L. Desjardins. Climate change—a long-term global environmental challenge. *Procedia - Social and Behavioral Sciences*, 77:247 – 252, 2013. The Harmony of Civilization and Prosperity for All: Selected Papers of Beijing Forum (2009-2010).

[2] P. Kurzweil. Gaston planté and his invention of the lead–acid battery—the genesis of the first practical rechargeable battery. *Journal of Power Sources*, 195(14):4424 – 4434, 2010. Celebration of lead-acid 150 years.

[3] Christophe Pillot. Global market issues and trends, 2014. [Accessed July 11th, 2018].

[4] Jeff Desjardins. Explaining the surging demand for lithium-ion batteries, 2016. [Accessed July 6th, 2018].

[5] Elena M. Krieger, John Cannarella, and Craig B. Arnold. A comparison of lead-acid and lithium-based battery behavior and capacity fade in off-grid renewable charging applications. *Energy*, 60:492 – 500, 2013.

[6] R.A. Hanifah, S.F. Toha, and S. Ahmad. Electric vehicle battery modelling and performance comparison in relation to range anxiety. *Procedia Computer Science*, 76:250 – 256, 2015. 2015 IEEE International Symposium on Robotics and Intelligent Sensors (IEEE IRIS2015).

[7] Liu Jun. Addressing the grand challenges in energy storage. *Advanced Functional Materials*, 23(8):924–928.

[8] Naoki Nitta, Feixiang Wu, Jung Tae Lee, and Gleb Yushin. Li-ion battery materials: present and future. *Materials Today*, 18(5):252 – 264, 2015.

[9] Fraunhofer ISI. Energiespeicher-roadmap (update 2017): Hochenergie-batterien 2030+ und perspektiven zukünftiger batterietechnologien, 2014.

[10] Thomas Waldmann, Björn-Ingo Hogg, and Margret Wohlfahrt-Mehrens. Li plating as unwanted side reaction in commercial Li-ion cells – a review. *Journal of Power Sources*, 384:107 – 124, 2018.

[11] Dongxu Ouyang, Jiahao Liu, Mingyi Chen, and Jian Wang. Investigation into the fire hazards of lithium-ion batteries under overcharging. *Applied Sciences*, 7:1314, 12 2017.

[12] United Parcel Service of America. International lithium battery regulations, 2016.

[13] Fredrik Larsson, Petra Andersson, Per Blomqvist, and Bengt-Erik Mellander. Toxic fluoride gas emissions from lithium-ion battery fires. *Scientific Reports*, 7(1):10018, 2017.

[14] A. Mauger and C. M. Julien. Critical review on lithium-ion batteries: are they safe? sustainable? *Ionics*, 23(8):1933–1947, Aug 2017.

[15] Joseph Heelan, Eric Gratz, Zhangfeng Zheng, Qiang Wang, Mengyuan Chen, Diran Apelian, and Yan Wang. Current and prospective Li-ion battery recycling and recovery processes. *JOM*, 68(10):2632–2638, Oct 2016.

[16] The electric vehicle world sales database. Global plug-in sales for 2016. [Accessed July 6th, 2018].

[17] Pieremanuele Canepa, Gopalakrishnan Sai Gautam, Daniel C. Hannah, Rahul Malik, Miao Liu, Kevin G. Gallagher, Kristin A. Persson, and Gerbrand Ceder. Odyssey of multivalent cathode materials: Open questions and future challenges. *Chemical Reviews*, 117(5):4287–4341, 2017. PMID: 28269988.

[18] Markus Jäckle and Axel Groß. Microscopic properties of lithium, sodium, and magnesium battery anode materials related to possible dendrite growth. *The Journal of Chemical Physics*, 141(17):174710, 2014.

[19] Doron Aurbach, Z Lu, Alex Schechter, Yossef Gofer, H Gizbar, R Turgeman, Y Cohen, Mordechay Moshkovich, and Levi Mikhael. Prototype systems for rechargeable magnesium batteries. *Nature*, 407:724–7, 11 2000.

[20] Michael Naguib, Murat Kurtoglu, Volker Presser, Jun Lu, Junjie Niu, Min Heon, Lars Hultman, Yury Gogotsi, and Michel Barsoum. Two-dimensional nanocrystals produced by exfoliation of Ti_3AlC_2. *Advanced materials (Deerfield Beach, Fla.)*, 23:4248–53, 10 2011.

[21] Michael Ghidiu, Maria Lukatskaya, Meng-Qiang Zhao, Yury Gogotsi, and Michel Barsoum. Conductive two-dimensional titanium carbide 'clay' with high volumetric capacitance. *Nature*, advance online publication, 11 2014.

[22] US Government. *Mineral Commodity Summaries 2017*. US Govt Printing Office, S.l, 2017. ISBN: 978-1-4113-4104-3.

[23] Michael Naguib, Raymond R. Unocic, Beth L. Armstrong, and Jagjit Nanda. Large-scale delamination of multi-layers transition metal carbides and carbonitrides (MXenes). *Dalton Trans.*, 44:9353–9358, 2015.

[24] Seon Joon Kim, Hyeong-Jun Koh, Chang E. Ren, Ohmin Kwon, Kathleen Maleski, Soo-Yeon Cho, Babak Anasori, Choong-Ki Kim, Yang-Kyu Choi, Jihan Kim, Yury Gogotsi, and Hee-Tae Jung. Metallic $Ti_3C_2t_x$ MXene gas sensors with ultrahigh signal-to-noise ratio. *ACS Nano*, 12(2):986–993, 2018. PMID: 29368519.

[25] Lingxia Wu, Xianbo Lu, Dhanjai, Zhong-Shuai Wu, Yanfeng Dong, Xiaohui Wang, Shuanghao Zheng, and Jiping Chen. 2d transition metal carbide MXene as a robust biosensing platform for enzyme immobilization and ultrasensitive detection of phenol. *Biosensors and Bioelectronics*, 107:69 – 75, 2018.

[26] Li Ding, Yanying Wei, Libo Li, Tao Zhang, Haihui Wang, Jian Xue, Liang-Xin Ding, Suqing Wang, Jürgen Caro, and Yury Gogotsi. MXene molecular sieving membranes for highly efficient gas separation. *Nature Communications*, 9(1):155, 2018.

[27] Chang E. Ren, Kelsey B. Hatzell, Mohamed Alhabeb, Zheng Ling, Khaled A. Mahmoud, and Yury Gogotsi. Charge- and size-selective ion sieving through $Ti_3C_2t_x$ MXene membranes. *The Journal of Physical Chemistry Letters*, 6(20):4026–4031, 2015. PMID: 26722772.

[28] R. B. Rakhi, Bilal Ahmed, M. N. Hedhili, Dalaver H. Anjum, and H. N. Alshareef. Effect of postetch annealing gas composition on the structural and electrochemical properties of Ti_2CT_x MXene electrodes for supercapacitor applications. *Chemistry of Materials*, 27(15):5314–5323, 2015.

[29] Jingrun Ran, Guoping Gao, Fa-Tang Li, Tian-Yi Ma, Aijun Du, and Shi-Zhang Qiao. Ti_3C_2 MXene co-catalyst on metal sulfide photo-absorbers for enhanced visible-light photocatalytic hydrogen production. *Nature Communications*, 8:13907 EP –, Jan 2017. Article.

[30] Zhonglu Guo, Jian Zhou, Linggang Zhu, and Zhimei Sun. MXene: a promising photocatalyst for water splitting. *J. Mater. Chem. A*, 4:11446–11452, 2016.

[31] Hui Pan. Ultra-high electrochemical catalytic activity of MXenes. *Scientific Reports*, 6:32531 EP –, Sep 2016. Article.

[32] Christopher Eames and M. Saiful Islam. Ion intercalation into two-dimensional transition-metal carbides: Global screening for new high-capacity battery materials. *Journal of the American Chemical Society*, 136(46):16270–16276, 2014. PMID: 25310601.

[33] Babak Anasori, Maria Lukatskaya, and Yury Gogotsi. 2d metal carbides and nitrides (MXenes) for energy storage. *Nature Reviews Materials*, 2:16098, 01 2017.

[34] Michael Naguib, Joseph Halim, Jun Lu, Kevin M. Cook, Lars Hultman, Yury Gogotsi, and Michel W. Barsoum. New two-dimensional niobium and vanadium carbides as promising materials for Li-ion batteries. *Journal of the American Chemical Society*, 135(43):15966–15969, 2013. PMID: 24144164.

[35] Fanfan Liu, Jie Zhou, Shuwei Wang, Bingxin Wang, Cai Shen, Libo Wang, Qianku Hu, Qing Huang, and Aiguo Zhou. Preparation of high-purity V_2C MXene and electrochemical properties as Li-ion batteries. *Journal of The Electrochemical Society*, 164:A709–A713, 01 2017.

[36] Yohan Dall'Agnese, Pierre-Louis Taberna, Yury Gogotsi, and Patrice Simon. Two-dimensional vanadium carbide (MXene) as positive electrode for sodium-ion capacitors. *The Journal of Physical Chemistry Letters*, 6(12):2305–2309, 2015. PMID: 26266609.

[37] Armin VahidMohammadi, Ali Hadjikhani, Sina Shahbazmohamadi, and Majid Beidaghi. Two-dimensional vanadium carbide (MXene) as a high-capacity cathode material for rechargeable aluminum batteries. *ACS Nano*, 11(11):11135–11144, 2017. PMID: 29039915.

[38] Yu Xie, Yohan Dall'Agnese, Michael Naguib, Yury Gogotsi, Michel W. Barsoum, Houlong L. Zhuang, and Paul R. C. Kent. Prediction and characterization of MXene nanosheet anodes for non-lithium-ion batteries. *ACS Nano*, 8(9):9606–9615, 2014. PMID: 25157692.

[39] Oxford Dictionaries. Definition of battery in english, June 2018.

[40] John B. Goodenough and Kyu-Sung Park. The Li-ion rechargeable battery: A perspective. *Journal of the American Chemical Society*, 135(4):1167–1176, 2013. PMID: 23294028.

[41] Pankaj Arora and Zhengming (John) Zhang. Battery separators. *Chemical Reviews*, 104(10):4419–4462, 2004. PMID: 15669158.

[42] Adam H. Whitehead and Martha Schreiber. Current collectors for positive electrodes of lithium-based batteries. *Journal of The Electrochemical Society*, 152(11):A2105, 2005.

[43] The New York Times. Australia powers up the world's biggest battery — courtesy of elon musk, June 2018. [Accessed July 6th, 2018].

[44] Rosemary Gene Ehl and Aaron J. Ihde. Faraday's electrochemical laws and the determination of equivalent weights. *Journal of Chemical Education*, 31(5):226, 1954.

[45] J.O.M. Bockris, A.K.N. Reddy, and M.E. Gamboa-Aldeco. *Modern Electrochemistry 2A: Fundamentals of Electrodics*. Modern Electrochemistry. Springer US, 2007. ISBN: 9780306476051.

[46] Eric K. Rideal. Overpotential and catalytic activity. *Journal of the American Chemical Society*, 42(1):94–105, 1920.

[47] G. D. Short and Edmund. Bishop. Concentration overpotentials on antimony electrodes in differential electrolytic potentiometry. *Analytical Chemistry*, 37(8):962–967, 1965.

[48] John B. Goodenough and Youngsik Kim. Challenges for rechargeable Li batteries. *Chemistry of Materials*, 22(3):587–603, 2010.

[49] Martin Winter and Ralph J. Brodd. What are batteries, fuel cells, and supercapacitors? *Chemical Reviews*, 104(10):4245–4270, 2004. PMID: 15669155.

[50] Masaki Matsui. Study on electrochemically deposited Mg metal. *Journal of Power Sources*, 196(16):7048 – 7055, 2011. 15th International Meeting on Lithium Batteries (IMLB).

[51] Hyun Deog Yoo, Ivgeni Shterenberg, Yosef Gofer, Gregory Gershinsky, Nir Pour, and Doron Aurbach. Mg rechargeable batteries: an on-going challenge. *Energy Environ. Sci.*, 6:2265–2279, 2013.

[52] J.-M. Tarascon and M. Armand. Issues and challenges facing rechargeable lithium batteries. *Nature*, 414:359 EP –, Nov 2001.

[53] William Haynes. *CRC handbook of chemistry and physics : a ready-reference book of chemical and physical data*. CRC Press, Boca Raton, FL, 2011. ISBN: 978-1439855119.

[54] Peter C. K. Vesborg and Thomas F. Jaramillo. Addressing the terawatt challenge: scalability in the supply of chemical elements for renewable energy. *RSC Adv.*, 2:7933–7947, 2012.

[55] Investing.com. Magnesium: New trillion dollar industry to revolutionize global economy, 2014. [Accessed July 6th, 2018].

[56] Advanced Light Source Berkeley lab. Toyota invests in promising magnesium battery research at the als, 2013. [Accessed July 6th, 2018].

[57] Rana Mohtadi and Fuminori Mizuno. Magnesium batteries: Current state of the art, issues and future perspectives. *Beilstein Journal of Nanotechnology*, 5:1291–1311, 2014.

[58] John Muldoon, Claudiu B. Bucur, and Thomas Gregory. Quest for nonaqueous multivalent secondary batteries: Magnesium and beyond. *Chemical Reviews*, 114(23):11683–11720, 2014. PMID: 25343313.

[59] Koji Makino, Yasushi Katayama, Takashi Miura, and Tomiya Kishi. Electrochemical insertion of magnesium to $Mg_0.5Ti_2(PO_4)^3$. *Journal of Power Sources*, 99(1):66 – 69, 2001.

[60] Na Wu, Ying-Chun Lyu, Rui-Juan Xiao, Xiqian Yu, Ya-Xia Yin, Xiao-Qing Yang, Hong Li, Lin Gu, and Yu-Guo Guo. A highly reversible, low-strain Mg-ion insertion anode material for rechargeable Mg-ion batteries. *Npg Asia Materials*, 6:e120 EP –, Aug 2014. Original Article.

[61] Jing Zeng, Yang Yang, Chao Li, Jiaqi Li, Jianxing Huang, Jing Wang, and Jinbao Zhao. Li3vo4: an insertion anode material for magnesium ion batteries with high specific capacity. *Electrochimica Acta*, 247:265 – 270, 2017.

[62] Seoung-Bum Son, Tao Gao, Steve P. Harvey, K. Xerxes Steirer, Adam Stokes, Andrew Norman, Chunsheng Wang, Arthur Cresce, Kang Xu, and Chunmei Ban. An artificial interphase enables reversible magnesium chemistry in carbonate electrolytes. *Nature Chemistry*, 10(5):532–539, 2018.

[63] Fuminori Mizuno, Nikhilendra Singh, Timothy S. Arthur, Paul T. Fanson, Mayandi Ramanathan, Aadil Benmayza, Jai Prakash, Yi-Sheng Liu, Per-Anders Glans, and Jinghua Guo. Understanding and overcoming the challenges posed by electrode/electrolyte interfaces in rechargeable magnesium batteries. *Frontiers in Energy Research*, 2:46, 2014.

[64] T.D. Gregory, R.J. Hoffman, and R.C. Winterton. Nonaqueous electrochemistry of magnesium; applications to energy storage. *Journal of the Electrochemical Society*, 21, 03 1990.

[65] Oren Aviv, Nir Amir, Elad Pollak, Orit Chusid, Vered Marks, Hugo Gottlieb, Liraz Larush, Ella Zinigrad, and Doron Aurbach. Electrolyte solutions with a wide electrochemical window for rechargeable magnesium batteries. *Journal of The Electrochemical Society - J ELECTROCHEM SOC*, 155, 01 2008.

[66] Nir Pour, Yossi Gofer, Dan T. Major, and Doron Aurbach. Structural analysis of electrolyte solutions for rechargeable Mg batteries by stereoscopic means and dft calculations. *Journal of the American Chemical Society*, 133(16):6270–6278, 2011. PMID: 21456525.

[67] Pieremanuele Canepa, Saivenkataraman Jayaraman, Lei Cheng, Nav Nidhi Rajput, William Richards, Gopalakrishnan Sai Gautam, Larry A Curtiss, Kristin Persson, and Gerbrand Ceder. Elucidating the structure of the magnesium aluminum chloride complex electrolyte for magnesium-ion batteries. *Energy Environ. Sci.*, pages –, 10 2015.

[68] Doron Aurbach, Haim Gizbar, Alex Schechter, Orit Chusid, Hugo E. Gottlieb, Yossef Gofer, and Israel Goldberg. Electrolyte solutions for rechargeable magnesium batteries based on organomagnesium chloroaluminate complexes. *Journal of The Electrochemical Society*, 149:A115–A121, 02 2002.

[69] Robert E. Doe, Ruoban Han, Jaehee Hwang, Andrew J. Gmitter, Ivgeni Shterenberg, Hyun Deog Yoo, Nir Pour, and Doron Aurbach. Novel, electrolyte solutions comprising fully inorganic salts with high anodic stability for rechargeable magnesium batteries. *Chem. Commun.*, 50:243–245, 2014.

[70] John Muldoon, Claudiu B. Bucur, Allen G. Oliver, Tsuyoshi Sugimoto, Masaki Matsui, Hee Soo Kim, Gary D. Allred, Jaroslav Zajicek, and Yukinari Kotani. Electrolyte roadblocks to a magnesium rechargeable battery. *Energy Environ. Sci.*, 5:5941–5950, 2012.

[71] Pubchem. Tetrahydrofuran, 2018. Available at: https://pubchem.ncbi.nlm.nih.gov/compound/tetrahydrofuran#section=Odor, [Accessed July 6th, 2018].

[72] Nav Nidhi Rajput, Xiaohui Qu, Niya Sa, Anthony K. Burrell, and Kristin A. Persson. The coupling between stability and ion pair formation in magnesium electrolytes from first-principles quantum mechanics and classical molecular dynamics. *Journal of the American Chemical Society*, 137(9):3411–3420, 2015. PMID: 25668289.

[73] Se-Young Ha, Yong-Won Lee, Sang Won Woo, Bonjae Koo, Jeom-Soo Kim, Jaephil Cho, Kyu Tae Lee, and Nam-Soon Choi. Magnesium(ii) bis(trifluoromethane sulfonyl) imide-based electrolytes with wide electrochemical windows for rechargeable magnesium batteries. *ACS Applied Materials & Interfaces*, 6(6):4063–4073, 2014. PMID: 24559269.

[74] Zheng Ma, Mega Kar, Changlong Xiao, Maria Forsyth, and Douglas R. MacFarlane. Electrochemical cycling of Mg in $Mg[TFSI]_2$/tetraglyme electrolytes. *Electrochemistry Communications*, 78:29 – 32, 2017.

[75] Seydou Hebié, Hoang Phuong Khanh Ngo, Jean-Claude Leprêtre, Cristina Iojoiu, Laure Cointeaux, Romain Berthelot, and Fannie Alloin. Electrolyte based on easily synthesized, low cost triphenolate–borohydride salt for high performance $Mg(TFSI)_2$-glyme rechargeable magnesium batteries. *ACS Applied Materials & Interfaces*, 9(34):28377–28385, 2017. PMID: 28792210.

[76] Carter Tyler J., Mohtadi Rana, Arthur Timothy S., Mizuno Fuminori, Zhang Ruigang, Shirai Soichi, and Kampf Jeff W. Boron clusters as highly stable magnesium-battery electrolytes. *Angewandte Chemie International Edition*, 53(12):3173–3177.

[77] Oscar Tutusaus, Rana Mohtadi, Timothy Arthur, Fuminori Mizuno, Emily G. Nelson, and Yulia V. Sevryugina. An efficient halogen-free electrolyte for use in rechargeable magnesium batteries. *Angewandte Chemie*, 54, 05 2015.

[78] Mohtadi Rana, Matsui Masaki, Arthur Timothy S., and Hwang Son-Jong. Magnesium borohydride: From hydrogen storage to magnesium battery. *Angewandte Chemie International Edition*, 51(39):9780–9783.

[79] Albert L. Lipson, Sang-Don Han, Baofei Pan, Kimberly See, Andrew Gewirth, Chen Liao, J.T Vaughey, and Brian Ingram. Practical stability limits of magnesium electrolytes. *Journal of The Electrochemical Society*, 163:A2253–A2257, 08 2016.

[80] Pieremanuele Canepa, Shou-Hang Bo, Gopalakrishnan Sai Gautam, Baris Key, William Richards, Tan Shi, Yaosen Tian, Yan Wang, Juchuan Li, and Gerbrand Ceder. High magnesium mobility in ternary spinel chalcogenides, 11 2017.

[81] Muldoon John, Bucur Claudiu B., and Gregory Thomas. Fervent hype behind magnesium batteries: An open call to synthetic chemists—electrolytes and cathodes needed. *Angewandte Chemie International Edition*, 56(40):12064–12084.

[82] E. Levi, M. D. Levi, O. Chasid, and D. Aurbach. A review on the problems of the solid state ions diffusion in cathodes for rechargeable Mg batteries. *Journal of Electroceramics*, 22(1–3):13–19, Dec 2007.

[83] Xiaoqi Sun, Patrick Bonnick, and Linda F. Nazar. Layered TiS_2 positive electrode for Mg batteries. *ACS Energy Letters*, 1(1):297–301, 2016.

[84] Hyun Deog Yoo, Yanliang Liang, Hui Dong, Junhao Lin, Hua Wang, Yisheng Liu, Lu Ma, Tianpin Wu, Yifei Li, Qiang Ru, Yan Jing, Qinyou An, Wu Zhou, Jinghua Guo, Jun Lu, Sokrates T. Pantelides, Xiaofeng Qian, and Yan Yao. Fast kinetics of magnesium monochloride cations in interlayer-expanded titanium disulfide for magnesium rechargeable batteries. *Nature Communications*, 8(1):339, 2017.

[85] Chen Ling and Koji Suto. Thermodynamic origin of irreversible magnesium trapping in chevrel phase Mo_6S_8: Importance of magnesium and vacancy ordering. *Chemistry of Materials*, 29(8):3731–3739, 2017.

[86] Ariel Mitelman, Elena Levi, Eli Lancry, and Doron Aurbach. On the Mg trapping mechanism in electrodes comprising chevrel phases. In *ECS Transactions*. ECS, 2007.

[87] Chen Ling and Ruigang Zhang. Manganese dioxide as rechargeable magnesium battery cathode. *Frontiers in Energy Research*, 5:30, 2017.

[88] Ruigang Zhang, Timothy S. Arthur, Chen Ling, and Fuminori Mizuno. Manganese dioxides as rechargeable magnesium battery cathode; synthetic approach to understand magnesiation process. *Journal of Power Sources*, 282:630 – 638, 2015.

[89] Masashi Inamoto, Hideki Kurihara, and Tatsuhiko Yajima. Vanadium pentoxide-based composite synthesized using microwave water plasma for cathode material in rechargeable magnesium batteries. *Materials*, 6(10):4514–4522, Oct 2013.

[90] Gregory Gershinsky, Hyun Deog Yoo, Yosef Gofer, and Doron Aurbach. Electrochemical and spectroscopic analysis of Mg^{2+} intercalation into thin film electrodes of layered oxides: V_2O_5 and MoO_3. *Langmuir*, 29(34):10964–10972, 2013. PMID: 23924361.

[91] Petr Novak. Electrochemical insertion of magnesium in metal oxides and sulfides from aprotic electrolytes. *Journal of The Electrochemical Society*, 140(1):140, 1993.

[92] M. Shibata, D. Omori, and N. Furuya. Electrochemical behavior of magnesium anode in non-aqueous solutions. *Electrochemistry*, 66(4):411–416, 1998. cited By 1.

[93] M. W. Barsoum. *MAX phases : properties of machinable ternary carbides and nitrides*. Wiley-VCH, Weinheim, 2013. ISBN: 9783527654581.

[94] Michel W. Barsoum. The $M_{n+1}AX_n$ phases: A new class of solids: Thermodynamically stable nanolaminates. *Progress in Solid State Chemistry*, 28(1):201 – 281, 2000.

[95] Per Eklund, Johanna Rosen, and Per O Å Persson. Layered ternary $M_{n+1}AX_n$ phases and their 2d derivative MXene: an overview from a thin-film perspective. *Journal of Physics D: Applied Physics*, 50(11):113001, 2017.

[96] Tianyu Liu. The birth of MXene (interview script), May 2018. [Accessed July 6th, 2018].

[97] Naguib Michael, Mochalin Vadym N., Barsoum Michel W., and Gogotsi Yury. 25th anniversary article: MXenes: A new family of two-dimensional materials. *Advanced Materials*, 26(7):992–1005.

[98] Vincent Ming Hong Ng, Hui Huang, Kun Zhou, Pooi See Lee, Wenxiu Que, Jason Zhichuan Xu, and Ling Bing Kong. Recent progress in layered transition metal carbides and/or nitrides (MXenes) and their composites: synthesis and applications. *J. Mater. Chem. A*, 5:3039–3068, 2017.

[99] Martin Magnuson and Maurizio Mattesini. Chemical bonding and electronic-structure in MAX phases as viewed by X-ray spectroscopy and density functional theory. *Thin Solid Films*, 621:108 – 130, 2017.

[100] Alhabeb Mohamed, Maleski Kathleen, Mathis Tyler S., Sarycheva Asia, Hatter Christine B., Uzun Simge, Levitt Ariana, and Gogotsi Yury. Selective etching of silicon from Ti_3SiC_2 (MAX) to obtain 2d titanium carbide (MXene). *Angewandte Chemie International Edition*, 57(19):5444–5448.

[101] F. Liu, A. Zhou, J. Chen, J. Jia, W. Zhou, L. Wang, and Q. Hu. Preparation of Ti_3C_2 and Ti_2C MXenes by fluoride salts etching and methane adsorptive properties. *Applied Surface Science*, 416:781–789, September 2017.

[102] Yu Xie, Michael Naguib, Vadym N. Mochalin, Michel W. Barsoum, Yury Gogotsi, Xiqian Yu, Kyung-Wan Nam, Xiao-Qing Yang, Alexander I. Kolesnikov, and Paul R. C. Kent. Role of surface structure on Li-ion energy storage capacity of two-dimensional transition-metal carbides. *Journal of the American Chemical Society*, 136(17):6385–6394, 2014. PMID: 24678996.

[103] Mohammad Khazaei, Masao Arai, Taizo Sasaki, Ahmad Ranjbar, Yunye Liang, and Seiji Yunoki. Oh-terminated two-dimensional transition metal carbides and nitrides as ultralow work function materials. *Phys. Rev. B*, 92:075411, Aug 2015.

[104] Yuelei Bai, Kun Zhou, Narasimalu Srikanth, John H. L. Pang, Xiaodong He, and Rongguo Wang. Dependence of elastic and optical properties on surface terminated groups in two-dimensional MXene monolayers: a first-principles study. *RSC Adv.*, 6:35731–35739, 2016.

[105] Junping Hu, Bo Xu, Chuying Ouyang, Shengyuan A. Yang, and Yugui Yao. Investigations on V_2C and V_2CX_2 (X = F, OH) monolayer as a promising anode material for Li-ion batteries from first-principles calculations. *The Journal of Physical Chemistry C*, 118(42):24274–24281, 2014.

[106] Michael Naguib, Olha Mashtalir, Joshua Carle, Volker Presser, Jun Lu, Lars Hultman, Yury Gogotsi, and Michel W. Barsoum. Two-dimensional transition metal carbides. *ACS Nano*, 6(2):1322–1331, 2012. PMID: 22279971.

[107] Zhimei Sun, Sa Li, Rajeev Ahuja, and Jochen M. Schneider. Calculated elastic properties of M_2AlC (M=Ti, V, Cr, Nb and Ta). *Solid State Communications*, 129(9):589 – 592, 2004.

[108] Maria R. Lukatskaya, Olha Mashtalir, Chang E. Ren, Yohan Dall'Agnese, Patrick Rozier, Pierre-Louis Taberna, Michael Naguib, Patrice Simon, Michel W. Barsoum, and Yury Gogotsi. Cation Intercalation and High Volumetric Capacitance of Two-Dimensional Titanium Carbide. *Science*, vol. 341(n° 6153):pp. 1502–1505, September 2013.

[109] Olha Mashtalir, Michael Naguib, Vadym N Mochalin, Yohan Dall'Agnese, Min Heon, Michel Barsoum, and Yury Gogotsi. Intercalation and delamination of layered carbides and carbonitrides. *Nature communications*, 4:1716, 04 2013.

[110] Nitin K. Chaudhari, Hanuel Jin, Byeongyoon Kim, Du San Baek, Sang Hoon Joo, and Kwangyeol Lee. MXene: an emerging two-dimensional material for future energy conversion and storage applications. *J. Mater. Chem. A*, 5:24564–24579, 2017.

[111] Patrice Simon. Two-dimensional MXene with controlled interlayer spacing for electrochemical energy storage. *ACS Nano*, 11(3):2393–2396, 2017. PMID: 28281347.

[112] Eric S. Muckley, Michael Naguib, Hsiu-Wen Wang, Lukas Vlcek, Naresh C. Osti, Robert L. Sacci, Xiahan Sang, Raymond R. Unocic, Yu Xie, Madhusudan Tyagi, Eugene Mamontov, Katharine L. Page, Paul R. C. Kent, Jagjit Nanda, and Ilia N. Ivanov. Multimodality of structural, electrical, and gravimetric responses of intercalated MXenes to water. *ACS Nano*, 11(11):11118–11126, 2017. PMID: 29019645.

[113] Ming Lu, Haojie Li, Wenjuan Han, Junnan Chen, Wen Shi, Jiaheng Wang, Xiang-Min Meng, Jingang Qi, Haibo Li, Bingsen Zhang, Wei Zhang, and Weitao Zheng. 2d titanium carbide (MXene) electrodes with lower-F surface for high performance lithium-ion batteries. *Journal of Energy Chemistry*, 2018.

[114] Yohan Dall'Agnese, Maria R. Lukatskaya, Kevin M. Cook, Pierre-Louis Taberna, Yury Gogotsi, and Patrice Simon. High capacitance of surface-modified 2d titanium carbide in acidic electrolyte. *Electrochemistry Communications*, 48:118 – 122, 2014.

[115] Qing Tang, Zhen Zhou, and Panwen Shen. Are MXenes promising anode materials for Li-ion batteries? computational studies on electronic properties and Li storage capability of Ti_3C_2 and $Ti_3C_2X_2$ (X = F, OH) monolayer. *Journal of the American Chemical Society*, 134(40):16909–16916, 2012. PMID: 22989058.

[116] Johannes Etzkorn, Martin Ade, and Harald Hillebrecht. V_2AlC, V_4AlC_{3-x} ($x \approx 0.31$), and $V_{12}Al_3C_8$: Synthesis, crystal growth, structure, and superstructure. *Inorganic Chemistry*, 46(18):7646–7653, 2007. PMID: 17685605.

[117] W. L. Bragg. The diffraction of short electromagnetic waves by a crystal. *Scientia*, 23(45):153, 1929.

[118] Y.S. Cho and C.C. Koch. Mechanical milling of ordered intermetallic compounds: the role of defects in amorphization. *Journal of Alloys and Compounds*, 194(2):287 – 294, 1993.

[119] Chunfeng Hu, Lingfeng He, Mingyue Liu, Xiaohui Wang, Jingyang Wang, Meishuan Li, Y.-W Bao, and Yanchun Zhou. In situ reaction synthesis and mechanical properties of V_2AlC. *Journal of the American Ceramic Society*, 91:4029 – 4035, 11 2008.

[120] Chunfeng Hu, Jie Zhang, Y.-W Bao, Jingyang Wang, Meishuan Li, and Yanchun Zhou. In situ reaction synthesis and decomposition of Ta_2AlC. *International Journal of Materials Research - INT J MATER RES*, 99:8–13, 01 2008.

[121] Xiaohui Wang and Yanchun Zhou. Solid-liquid reaction synthesis of layered machinable Ti_3AlC_2 ceramic. *J. Mater. Chem.*, 12:455–460, 2002.

[122] Nilay G Akdogan, George C Hadjipanayis, and David J Sellmyer. Novel nd 2 fe 14 b nanoflakes and nanoparticles for the development of high energy nanocomposite magnets. *Nanotechnology*, 21(29):295705, 2010.

[123] James D. Robertson, Loris Rizzello, Milagros Avila-Olias, Jens Gaitzsch, Claudia Contini, Monika S. Magon, Stephen A. Renshaw, and Giuseppe Battaglia. Purification of nanoparticles by size and shape. *Scientific Reports*, 6:27494, Jun 2016. Article.

[124] C. Wadenpohl and F. Löffler. Electrostatic agglomeration and centrifugal separation of diesel soot particles. *Chemical Engineering and Processing: Process Intensification*, 33(5):371 – 377, 1994.

[125] Xinmin Min and Yi Ren. Electronic structures and bonding properties of Ti_2AlC and Ti_3AlC_2. *Journal of Wuhan University of Technology-Mater. Sci. Ed.*, 22(1):27–30, Feb 2007.

[126] Mohamed Alhabeb, Kathleen Maleski, Babak Anasori, Pavel Lelyukh, Leah Clark, Saleesha Sin, and Yury Gogotsi. Guidelines for synthesis and processing of two-dimensional titanium carbide ($Ti_3C_2T_x$ MXene). *Chemistry of Materials*, 29(18):7633–7644, 2017.

[127] Dandan Sun, Qianku Hu, Jinfeng Chen, Xinyu Zhang, Libo Wang, Qinghua Wu, and Aiguo Zhou. Structural transformation of MXene (V_2C, Cr_2C, and Ta_2C) with O-groups during lithiation: A first-principles investigation. *ACS Applied Materials & Interfaces*, 8(1):74–81, 2016. PMID: 26703113.

[128] G B Ying, Sankalp Kota, Andrew D. Dillon, Aaron T. Fafarman, and Michel Barsoum. Conductive transparent V_2CT_x (MXene) films. *FlatChem*, 8, 03 2018.

[129] Ivgeni Shterenberg, Michael Salama, Hyun Deog Yoo, Yosef Gofer, Jin-Bum Park, Yang-Kook Sun, and Doron Aurbach. Evaluation of $(CF_3SO_2)2N$-(TFSI) based electrolyte solutions for Mg batteries. *Journal of The Electrochemical Society*, 162(13):A7118–A7128, 2015.

[130] Carl Hamann. *Electrochemistry*. Wiley-VCH, Weinheim, 2007. ISBN: 978-3-527-31069-2.

[131] Jiajie Zhu and Udo Schwingenschlögl. P and Si functionalized MXenes for metal-ion battery applications. *2D Materials*, 4(2):025073, 2017.

[132] Maria R. Lukatskaya, Olha Mashtalir, Chang E. Ren, Yohan Dall'Agnese, Patrick Rozier, Pierre Louis Taberna, Michael Naguib, Patrice Simon, Michel W. Barsoum, and Yury Gogotsi. Cation intercalation and high volumetric capacitance of two-dimensional titanium carbide. *Science*, 341(6153):1502–1505, 2013.

[133] Michael Ghidiu, Joseph Halim, Sankalp Kota, David Bish, Yury Gogotsi, and Michel W. Barsoum. Ion-exchange and cation solvation reactions in Ti_3C_2 MXene. *Chemistry of Materials*, 28(10):3507–3514, 2016.

[134] Min Xu, Shulai Lei, Jing Qi, Qingyun Dou, Lingyang Liu, Yulan Lu, Qing Huang, Siqi Shi, and Xingbin Yan. Opening magnesium storage capability of two-dimensional MXene by intercalation of cationic surfactant. *ACS Nano*, 12(4):3733–3740, 2018. PMID: 29543438.

[135] Ayeong Byeon, Meng-Qiang Zhao, Chang E. Ren, Joseph Halim, Sankalp Kota, Patrick Urbankowski, Babak Anasori, Michel W. Barsoum, and Yury Gogotsi. Two-dimensional titanium carbide MXene as a cathode material for hybrid magnesium/lithium-ion batteries. *ACS Applied Materials & Interfaces*, 9(5):4296–4300, 2017. PMID: 27275950.

[136] Baofei Pan, Zhenxing Feng, Niya Sa, Sang-Don Han, Qing Ma, Paul Fenter, John T. Vaughey, Zhengcheng Zhang, and Chen Liao. Advanced hybrid battery with a magnesium metal anode and a spinel $LiMn_2O_4$ cathode. *Chem. Commun.*, 52:9961–9964, 2016.

[137] Yingwen Cheng, Hee Jung Chang, Hui Dong, Daiwon Choi, Vincent L. Sprenkle, Jun Liu, Yan Yao, and Guosheng Li. Rechargeable Mg-Li hybrid batteries: status and challenges. *Journal of Materials Research*, 31:1–17, 09 2016.

[138] Yingwen Cheng, Yuyan Shao, Ji-Guang Zhang, Vincent L. Sprenkle, Jun Liu, and Guosheng Li. High performance batteries based on hybrid magnesium and lithium chemistry. *Chem. Commun.*, 50:9644–9646, 2014.

[139] Kevin G. Gallagher, Steven Goebel, Thomas Greszler, Mark Mathias, Wolfgang Oelerich, Damla Eroglu, and Venkat Srinivasan. Quantifying the promise of lithium-air batteries for electric vehicles. *Energy Environ. Sci.*, 7:1555–1563, 2014.

Appendix A

Additional figures

EDX measurements

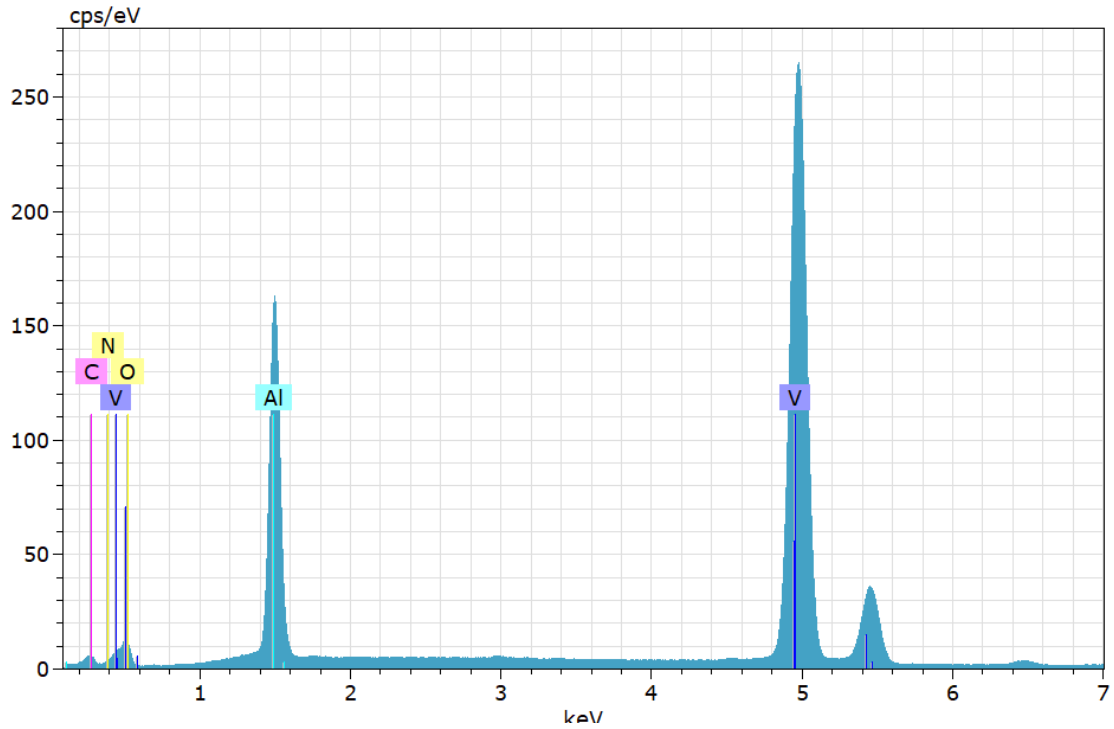

Figure A.1: The EDX spectra from one of the V_2AlC particles, showing significant peaks related to V and Al.

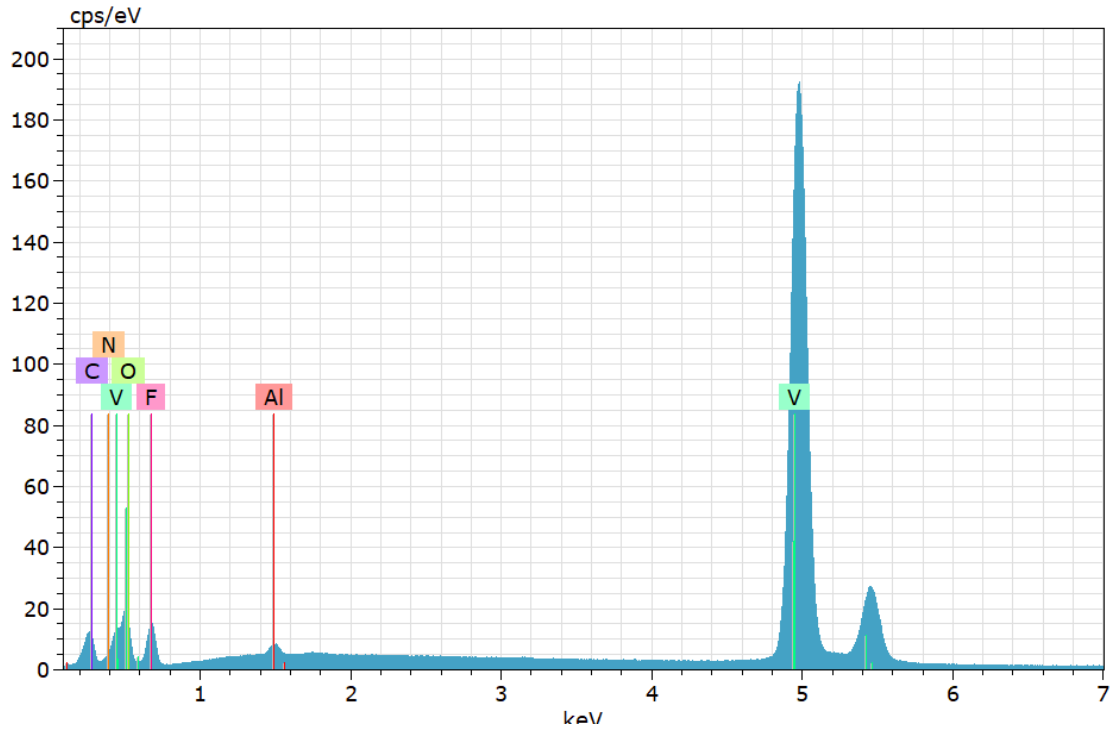

Figure A.2: The EDX spectra from one of the pristine V_2C particles, showing a significant reduction of the Al peak, from the V_2AlC particle in Figure A.1.

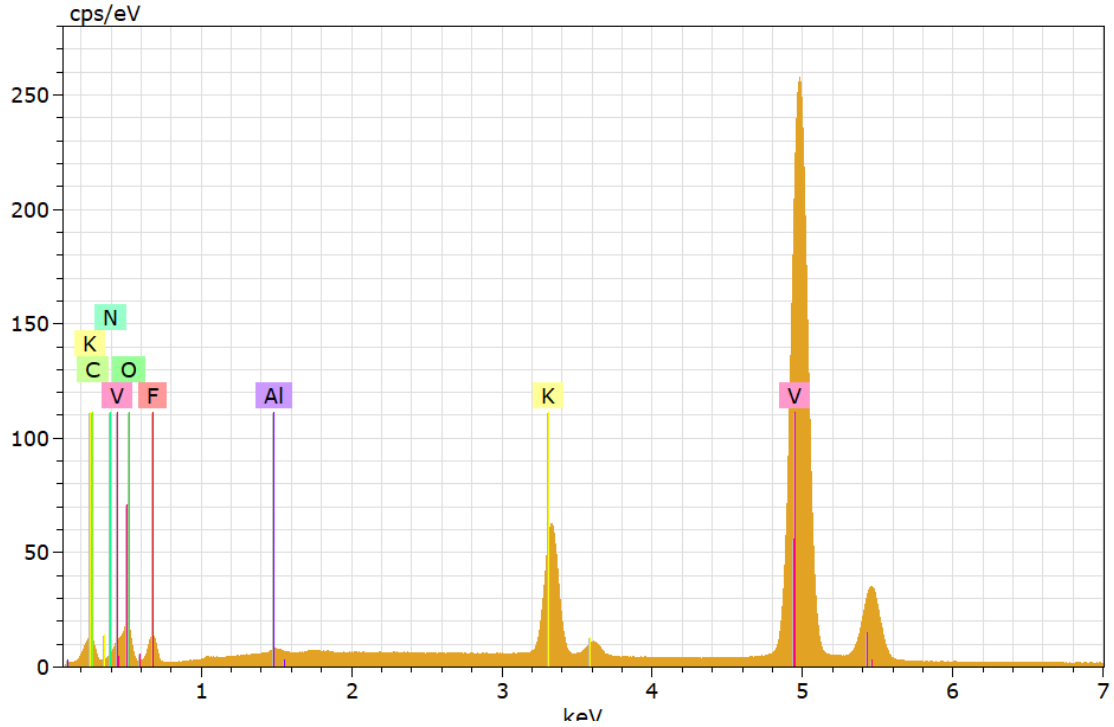

Figure A.3: The EDX spectra from one of the V_2C particles after the TBAOH treatment, showing the introduction of a significant K-peak from the pristine V_2C shown in Figure A.2.

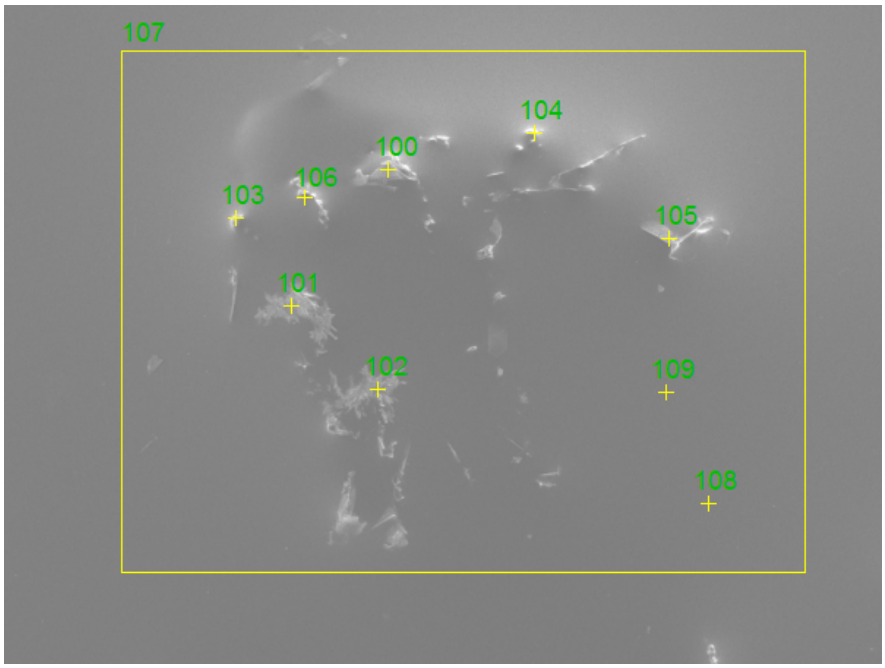

Figure A.4: Overview image of the points/areas that were measured by EDX of the dried TBAOH solution.

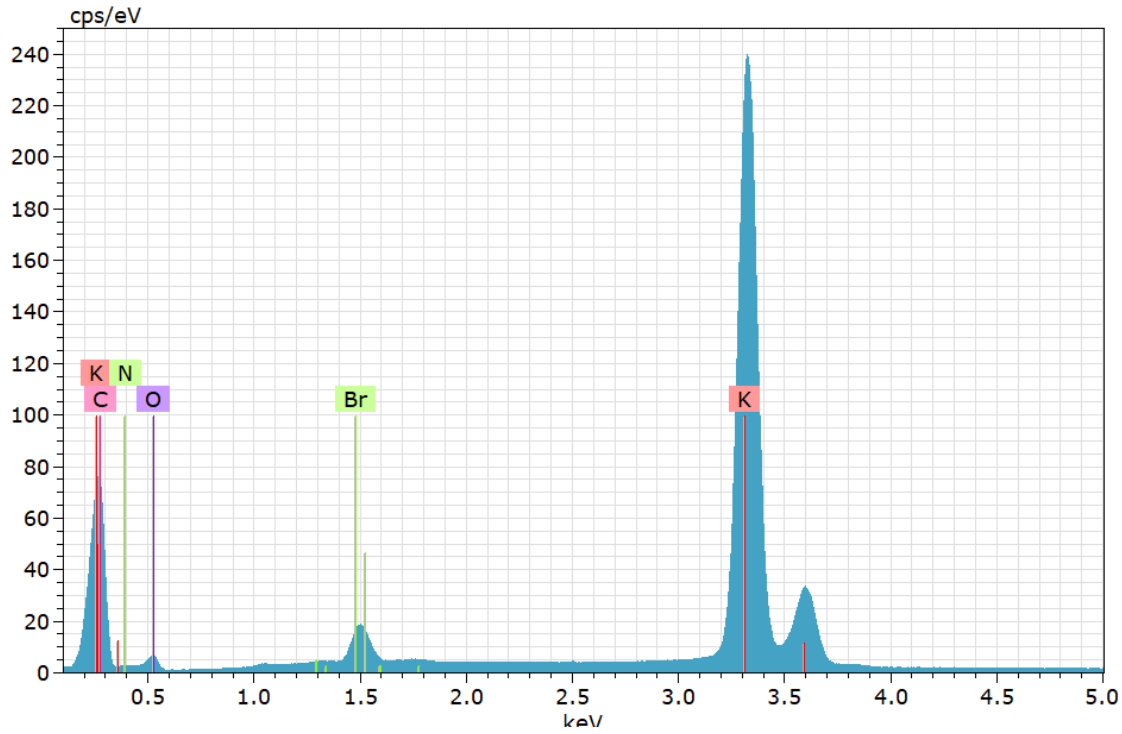

Figure A.5: The EDX spectra from one of the precipitated particles (point 102) in Figure A.4, showing a dominant K-peak, indicating that the precipitated particles consist of large amounts of potassium.

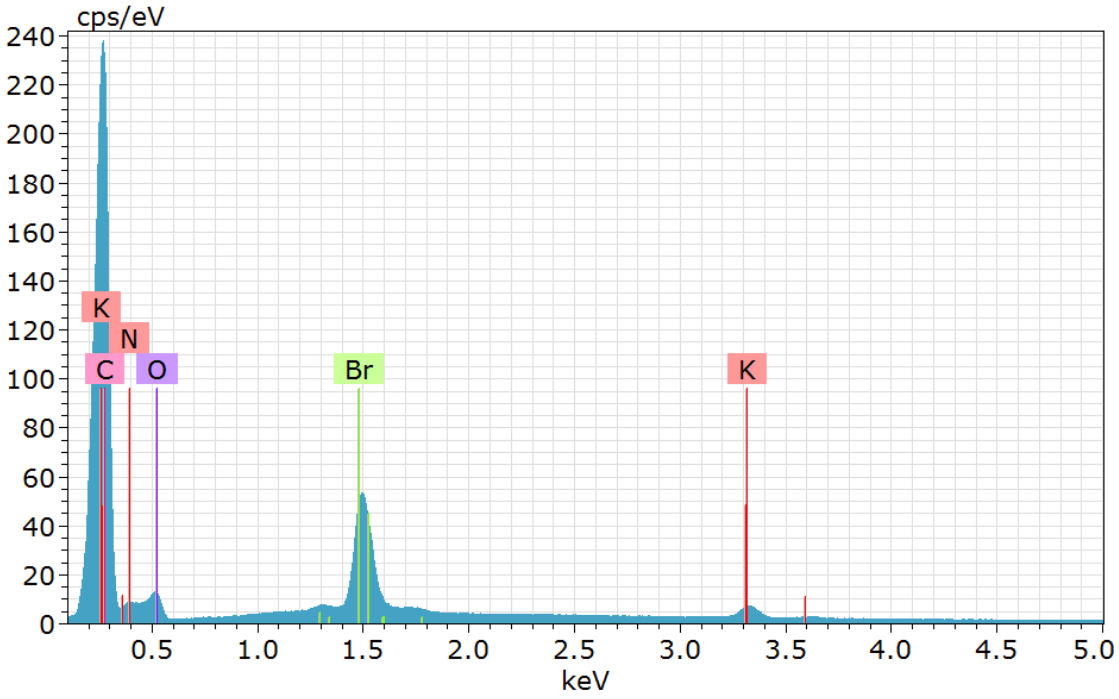

Figure A.6: The EDX spectra from the overview scan (area 107) from Figure A.4, showing a significant K-peak, in addition to a large peak related to Br impurities.

Synthesis images

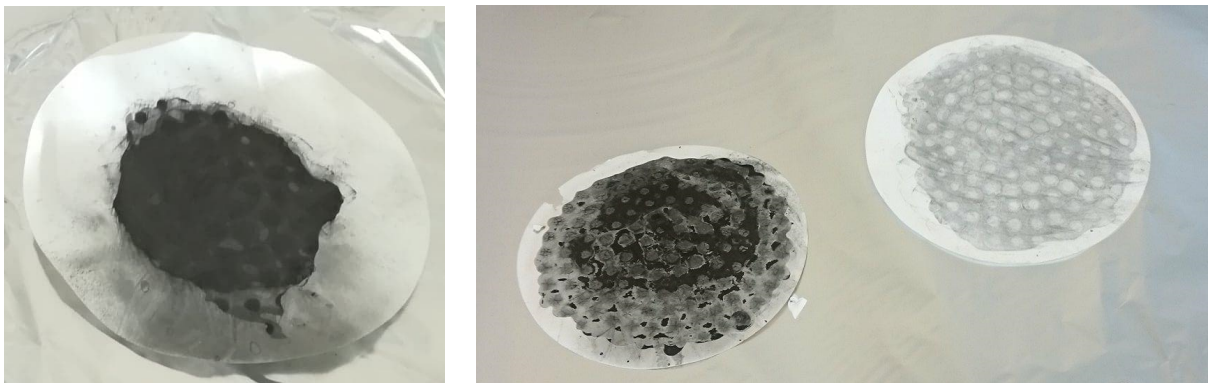

(a) (b)

Figure A.7: Pictures of the filter papers used for vacuum drying of the etched powders, after the easily accessible powder was scraped off. Image (a) shows the 0.45 µm pore sized filter paper used for the etching of MAX phase batch 1 with 48 % HF for 96 h, and (b) illustrates the 0.22 µm pore sized filter paper used for the etching of MAX phase batch 4 (left) and 5 (right), both with 48 % HF for 96 h.

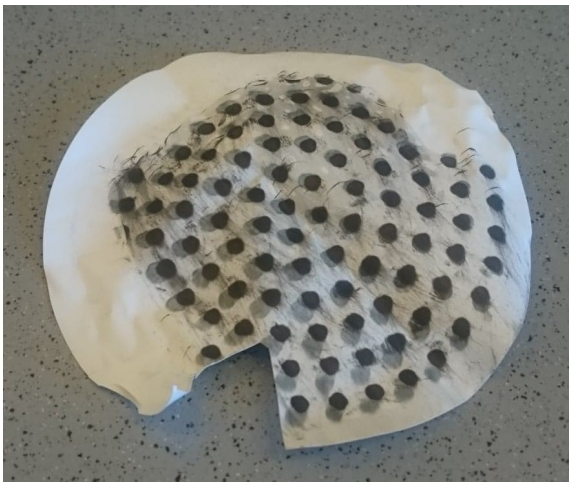

Figure A.8: Picture of the 0.22 µm pore sized filter paper used for vacuum drying of the first attempt to delaminate V_2C (by sonication), showing that all of the dried powder remained stuck on the filter paper.

(a) (b)

Figure A.9: Pictures of different parts of the synthesis process, where (a) show the green supernatant obtained after the first centrifugation after etching 2 (batch 1 - 96 h, 48%), and (b) illustrate the planetary milled powder of MAX phase batch 4 (4:ROTA-PEL-MIL) that got partly stuck to the planetary milling jar and balls.

Publication trend

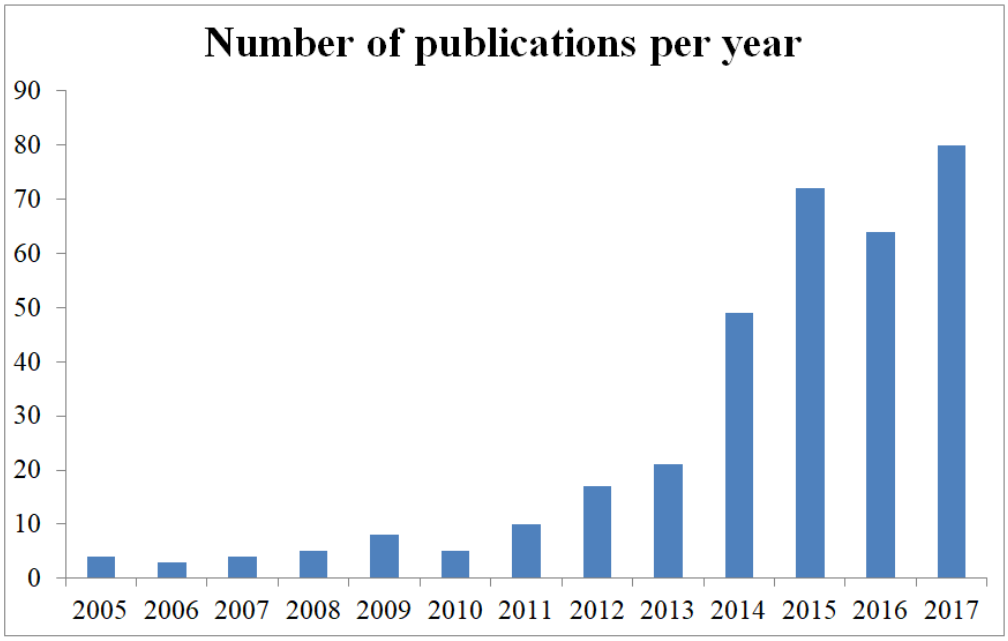

Figure A.10: Number of publications from 2005 until 2017 featuring magnesium battery. The plotted data is retrieved using Web of Science by Thomson Reuters.